Femtosecond Laser Interactions at Interfaces and Their Applications

by

Ryan D. Murphy

A dissertation submitted in partial fulfillment
of the requirements for the degree of
Doctor of Philosophy
(Applied Physics)
in The University of Michigan
2013

Doctoral Committee:

- Professor Steven M. Yalisove, Chair
- Professor Roy Clarke
- Research Professor Ben Torralva
- Professor Herbert G. Winful

© Ryan D. Murphy
2013

To my parents, Doug and Agnes Murphy

Acknowledgements

I would like to thank my family and friends for the support they have given me in my life and professional studies. I'm grateful for my previous and current colleagues helping me get where I am today, and I am particularly thankful for John Nees and Peter Diehr for helping me learn how to get around the lab. Thanks are especially due to my advisor Steven Yalisove and my colleague Ben Torralva for their continuing support and for showing me the importance of questioning everything.

Table of Contents

Dedication....................ii
Acknowledgements....................iii
List of Figures....................vii
List of Appendices....................xiv
Abstract....................xv
Chapter

1. **Introduction**....................1

2. **Background**....................6
    2.1 Femtosecond Laser Irradiation....................6
        2.1.2 Models and Mechanisms for Material Removal from Metals and Semiconductors....................7
    2.2 Nanoparticle Formation After Laser Irradiation....................9
    2.3 Laser Irradiation of Carbon Nanotubes....................10
    2.4 Laser Irradiation of Thin Films....................11
    2.5 Laser Induced Periodic Structures....................13
        2.5.1 Theories of Laser Induced Periodic Structures Formation with Periods Near λ....................14

3. **Experimental Details**....................26
    3.1 Sample Preparation....................26
    3.2 Ultrafast Irradiation in Air....................26
    3.3 Precise Single-Shot Ultrafast Irradiation in Air....................28
    3.4 Fluence Calculations....................29
    3.5 Nanoparticle Collection....................30

3.6 Ultrafast Pump-Probe Microscopy Shortly After Irradiation................31
3.7 Material Growth..34
3.7.1 Ni Thin Film Deposition..34
3.7.2 SiO_2 Thin Film Deposition..34
3.8 Microscopy Long After Irradiation...35
3.8.1 Optical Microscopy..35
3.8.2 Atomic Force Microscopy...35
3.8.3 Scanning Electron Microscopy..36
3.8.4 Transmission Electron Microscopy......................................36

4. Ultrafast Laser Interactions with Single Interfaces..................................38
4.1 Ultrafast Laser Interactions with a Ni-Silicon Interface........................39
4.2 Ultrafast Laser Interactions with a Ni-Glass Interface.........................45
4.3 Ultrafast Laser Printing of Nanoparticles..57

5. Ultrafast Laser Interactions with Multiple Interfaces................................66
5.1 Ultrafast Laser Formation of Microstructures at Substrate-Ni Film-SiO_2 Interfaces..67
5.2 Revisiting Femtosecond Laser Interactions with Single Interfaces.....78

6. Ultrafast Laser Formation of Laser Induced Periodic Structures............83
6.1 Ultrafast Laser Formation of LIPS on Bulk Si.....................................84
6.2 Ultrafast Laser Formation of Ripples at a Si-SiO_2 Interface................86
6.3 Ultrafast Laser Formation of LIPS Near Au Microstructures...............88
6.4 Pump-Probe Microscopy of LIPS Formation......................................98
6.5 Proposed LIPS Formation Mechanisms..101

7. Ultrafast Laser Interactions with Carbon..112
7.1 Ultrafast Laser Irradiation of Bulk Polymer.......................................113
7.2 Ultrafast Laser Irradiation of CNT Forests..116
7.3 Ultrafast Laser Irradiation of CNT-Polymer Composites....................118

8. Conclusions and Future Work..130

8.1 Single Interfaces..133

8.2 Multiple Interfaces..135

8.3 Laser Induced Periodic Structures...136

8.4 Composites...139

8.5 Improving Uniformity...140

Appendices...141

List of Figures

FIG 3.2.1. Ultrafast laser setup for irradiation of samples at normal incidence............27

FIG. 3.3.1. Microscope setup beside the laser irradiation line used to precisely place single laser shots..29

FIG 3.4.1. Typical image from the beam profiling camera for a 20 cm focal length lens..30

FIG. 3.5.1. Setup for printing nanoparticles onto a TEM grid substrate in air using irradiation of a thin film on a microscope cover slip...31

FIG. 3.6.1. Pump-probe microscopy with reflection imaging geometry.........................32

FIG 3.6.2. Pump-probe setup for imaging ripple formation at normal incidence...........33

FIG. 4.1.1. Damage threshold study of a bulk Ni target..39

FIG. 4.1.2. (a) SEM image of a crater in bulk Ni after irradiation with a single pulse at 0.71 J/cm^2...40

FIG. 4.1.3. (a) After irradiation, part of the Ni melts (dashed line) and homogeneous void nucleation occurs within the melt, perforating a plane in the film...........................41

FIG. 4.1.4. Irradiation of the 70 nm Ni film at 0.95 J/cm^2..42

FIG. 4.1.5. (a) Illustration of material removal from within the a 70 nm Ni film on a Si substrate at low fluence....43

FIG. 4.1.6. SEM images of single shot irradiation of a 10 nm Ni film on a Si substrate....44

FIG. 4.2.1. Irradiation of a 20 nm thick film of Ni on a glass microscope cover slip......46

FIG. 4.2.2. Representative AFM images of the surface roughness after laser irradiation of a 20 nm thick Ni film....47

FIG 4.2.3. Damage Radius vs. Fluence for varying thin film thicknesses of Ni deposited onto microscope cover slips....48

FIG. 4.2.4. Material removal threshold vs. Ni film thickness for thin Ni films on microscope cover slips....49

FIG. 4.2.5. (a) Part of the Ni film melts and homogeneous void nucleation occurs within the film, perforating a plane in the film....51

FIG. 4.2.6. Ni removal from a 20 nm Ni film....52

FIG. 4.2.7. Absorptance dependence of 780 nm light on Ni film thickness is plotted in green....53

FIG. 4.2.8. Predicted removal threshold based on percent changes in absorptance with film thickness....54

FIG. 4.2.9. Irradiation of a 10 nm thick film of Ni on a glass microscope cover slip......55

FIG. 4.2.10. Comparing film absorptance when laser light irradiates the Ni film first to irradiating the microscope cover slip first....56

FIG. 4.3.1. Printing of Ni NPs from a 20 nm Ni film at a fluence of 10 J/cm^2....58

FIG. 4.3.2. Printing of Ni NPs from a 20 nm Ni film at a fluence of 10 J/cm2....58

FIG. 4.3.3. EELS spectrum for a hexagonal NP....59

FIG. 4.3.4. NPs printed onto a TEM grid in a vacuum of 40 mTorr....60

FIG. 4.3.5. SWNTs grown using CVD from catalyst NPs which were printed from a 20 nm Ni film....61

FIG. 4.3.6. Au NP distributions from laser irradiation of 3 nm and 10 nm Au films....62

FIG. 4.3.7. Spherical Au NPs printed along with the formation of large Au slabs....63

FIG. 5.1.1. DIC images of blisters produced at normal incidence at the interface between a 70 nm Ni film and 1 µm of SiO_2....67

FIG. 5.1.2. AFM images and traces of blisters produced at normal incidence....68

FIG. 5.1.3. Blister dimensions vs. fluence after irradiation of a 70 nm Ni-SiO_2 interface....68

FIG. 5.1.4. Illustration of pit formation and subsequent collapse of blister structures after irradiation in the high fluence regime....70

FIG. 5.1.5. DIC image of microtube formation at a 70 nm Ni-SiO_2 interface....71

FIG. 5.1.6. Blister threshold as a function of Ni film thickness deposited on glass substrates....72

FIG. 5.1.7. Bright field OM image of microtubes formed at a glass substrate-1 nm Ni-SiO_2 interface using fluence of 0.20 J/cm^2....73

FIG. 5.1.8. (a) Bright field OM image of a microtube formed at 0.20 J/cm^2 before microfluidic flow....74

FIG. 5.1.9. Illustrated cross-sections of microtubes after laser irradiation and before thermal quenching....76

FIG. 5.1.10. AFM image and trace of the edge of a broken blister at the 1 nm film-SiO_2 interface....77

FIG. 5.2.1. (a) DIC image of blister formation at a glass substrate-SiO_2 interface at a fluence of 3.0 J/cm^2....78

FIG. 5.2.2. (a) AFM image of irradiation of 1 µm SiO_2 on a Si substrate with 1 laser pass....80

FIG. 6.1.1. (a) DIC image of a crater in Si after a single laser shot at 0.64 J/cm^2....85

FIG. 6.1.2. DIC image of a crater in Si with ripples after 2 shots at 0.64 J/cm^2....85

FIG. 6.2.1. (a) DIC image of LIPS formation at a Si-SiO_2 interface....86

FIG. 6.2.2. Illustration of crater formation after a single laser shot and LIPS formation after the second laser shot....87

FIG. 6.3.1. A pristine Au square mesa and illustrated $\frac{1}{e^2}$ diameter of the focused laser beam.....89

FIG. 6.3.2. Irradiation of square mesa at 0.30 J/cm^2.....90

FIG. 6.3.3. Distributions of Λ after irradiation of the mesa in Figure 6.3.3.....90

FIG. 6.3.4. Irradiation of square mesa at 0.64 J/cm^2.....91

FIG. 6.3.5. Irradiation of square mesa at 0.20 J/cm^2.....92

FIG. 6.3.6. Irradiation of square mesa at 0.20 J/cm^2 with the polarization vector perpendicular to the mesa edge.....92

FIG. 6.3.7. AFM image of LIPS on a Au surface after irradiation of a mesa edge at 0.20 J/cm^2 and perpendicular polarization.....93

FIG. 6.3.8. Irradiation of triangular mesas at 0.50 J/cm^2.....94

FIG. 6.3.9. (a) Irradiation of a triangle at 0.50 J/cm^2.....95

FIG. 6.3.10. DIC image of the irradiation of a square Au mesa at a peak fluence of 0.50 J/cm^2.....96

FIG. 6.3.11. Comparison of LIPS amplitudes in Si after irradiation of a Au mesa edge at 0.34 J/cm^2.....97

FIG. 6.3.12. Single pulse crater formation in Si at 0.75 J/cm^2 near a mesa edge.....97

FIG. 6.4.1. Pump-probe microscopy of Si removal after irradiation with a single pulse at 0.60 J/cm^2....98

FIG. 6.4.2. Image from white probe light using the white light pump-probe setup.......100

FIG. 6.4.3. Pump-probe microscopy of LIPS formation after irradiation of a crater in bulk Si with a single 0.34 J/cm^2 pulse....101

FIG. 6.5.1. The orientations of the first few fringes from diffraction of the fundamental beam from the microstructure edges are illustrated....103

FIG 7.1.1. Irradiation of Nafion with a single laser shot....114

FIG 7.1.2. Irradiation of Nafion with two slightly overlapping laser shots....115

FIG 7.1.3. Large area irradiation of Nafion with 50% overlapping laser shots....115

FIG 7.1.4. (a) Void formation in Nafion after a single laser shot....116

FIG 7.2.1. Top-down view of irradiation of a CNT forest with single laser pulses........117

FIG 7.2.2. Top-down view of crust removal from a CNT forest....118

FIG 7.3.1. SEM image of the direct-write large scale patterning of a 30 layer CNT-polymer composite film on a glass substrate irradiated with varying laser fluences above the damage threshold of the film....119

FIG 7.3.2. (a) SEM image of a single laser pulse damage area of a 30 layer CNT-polymer composite film on a glass substrate irradiated at a fluence of 0.12 J/cm^2......120

FIG 7.3.3. (a) Irradiation of a composite film at the damage threshold....121

FIG 7.3.4. UV-Vis transmittance measurements of a composite film before and after laser irradiation at a fluence of 0.12 J/cm^2..122

FIG 7.3.5. Single pulse irradiation of a 10 bi-layer sample at 0.11 J/cm^2....................123

FIG 7.3.6. (a) A CNT network organized within the 2-D XY plane is shown, with CNTs in green resting on the gray substrate..125

List of Appendices

Appendix 1..142
Appendix 2..147
Appendix 3..149
Appendix 4..151
Appendix 5..153
Appendix 6..157

Abstract

Femtosecond Laser Interactions at Interfaces and Their Applications

by

Ryan D. Murphy

Chair: Steven M. Yalisove

This dissertation explores the interaction of femtosecond (fs) laser irradiation with material interfaces. The role of the interface after irradiation near the damage and material removal thresholds of metal thin films, semiconductors, insulators, and carbon nanotubes is rarely addressed in the literature and is explored here. Resulting morphologies and dynamics after irradiation are investigated using optical microscopy, atomic force microscopy, scanning electron microscopy, transmission electron microscopy, and pump-probe microscopy in order to elucidate physical models for the observed phenomena.

The fundamental knowledge and mechanisms gained from studying the laser-material interactions in this thesis are used to explain phenomena observed by other researchers which were previously unexplained. For the first time, a link between homogeneous void nucleation within thin films to smooth surfaces and heterogeneous

void nucleation at interfaces to rougher surfaces is shown. Formation mechanisms of Laser Induced Periodic Structures (LIPS) were investigated using single laser shots to elucidate the roles various mechanisms play in LIPS formation. To study the dynamics of LIPS formation, a new pump-probe microscopy technique with resolution limits comparable to commercially available Nomarski contrast microscopes was developed to observe the formation of LIPS after femtosecond irradiation for the first time. This technique will allow for observation of the evolution of surface features in other systems after femtosecond irradiation which are not accessible with current pump-probe techniques.

The mechanisms covered in this thesis were used to improve current applications and for the creation of new devices. Thin Ni films were used to form blisters and microtubes at metal-SiO_2 interfaces. After femtosecond irradiation of very thin Ni films, the formation of flexible microfluidics was demonstrated. New alignment mechanisms and orientations of carbon nanotubes (CNTs) on substrates were discovered using the interaction of femtosecond laser pulses with CNT-polymer composites. Finally, a nanoparticle (NP) printing technique was developed to print NPs from thin films to control NP size. The technique was used to print catalyst Ni NPs onto substrates and chemical vapor deposition was used to grow CNTs from these NPs.

Chapter 1
Introduction

The interaction of femtosecond (fs) laser pulses with materials allows us to study the behavior of materials after laser irradiation under extreme conditions. Their characteristic sub-picosecond pulse lengths (150 fs in this thesis) provide high light intensities at the material surface which are not possible for longer pulsed lasers or continuous wave light [Maine 1988]. The available energy provided by commercial fs lasers for experiments is only ~ 1 mJ; however, the short pulse length pushes the light intensity to very high values, typically on the order of 10^{12} W/cm^2 in this thesis. The field strengths in these pulses are large enough to create a plasma of free electrons and ions in any material. This plasma is created before the material has time to respond to electron excitation, so the electrons reach high temperatures while the atomic lattice is still cold [Guo 2000]. Equilibration of the excited electrons with the cold lattice produces phase transitions of materials unique only to fs irradiation of materials [Saeta 1991, Tom 1988].

After equilibration, metals and semiconductors melt above a threshold fluence. The molten material then rapidly expands, and the coalescence of vacancies into voids within this expanding melt breaks the material along a plane, causing separation of a molten slab of material from the bulk. This mechanism of material removal from the bulk is rarely discussed in the literature and will be linked with the formation of smooth surfaces for the first time in this thesis. But how does the nature of material removal change after fs laser irradiation of interfaces?

The coalescence of vacancies into voids at the interface is never discussed in the literature and is a major focus of this thesis in order to advance the understanding of the interaction of ultrafast lasers with interfaces. The void nucleation process within bulk material is a homogeneous process, but void nucleation in the presence of a

heterogeneous interface is largely unexplored. When we hear the word “interface” our thinking usually turns immediately towards the solid-solid interface. These interfaces are of the utmost importance for applications in the electronics industry where controlling the properties of thin films, such as thickness, composition, and crystallinity, allows for the construction of microelectronic devices [Fortunato 2012]. The interaction of fs lasers with solid-solid interfaces is the main focus of this thesis, but in order to study this interaction, other types of interfaces must be considered. The liquid-solid interface discussed in Section 2.1.3 will be shown later to play a pivotal role in material removal from interfaces. While the air-solid interface determines the behavior of light at the material surface and consequently the response of material to irradiation.

The behavior of light changes in the presence of rough surfaces at the air-solid interface, which has been explored through the formation of Laser Induced Periodic Structures (LIPS) for many years [Guosheng 1982, Sipe 1983]. Classical light scattering from surfaces was originally proposed [Emmony 1973] but shortly after found to not be a sufficient description. The LIPS periodicities are smaller than predicted for classical diffraction theory; surface plasmon polariton (SPP) excitation must be taken into account. The behavior of light at material-dielectric interfaces is known to change if a surface defect is present but the source of LIPS is rarely addressed in the literature. This thesis seeks to explain the source of LIPS formation and the various factors which contribute to their morphology.

Finally, other solid-solid interfaces often not considered during fs laser irradiation involve carbon nanotubes. Carbon nanotube-solid interfaces are important when CNTs are used in devices. The bonding of CNTs to substrates and the mechanical and electrical properties of CNTs need to be considered in order to take advantage of their unique properties [Kumar 2011]. It will be shown in this thesis that the interaction of laser light with both CNT/substrate and CNT/polymer interfaces are important when using fs irradiation, and the fs laser/interface interaction may be used to change CNT-polymer composite properties.

The goals of this thesis include:

Identify the role of void formation in material removal within films and at interfaces after fs laser irradiation.

1. To determine the role of the interface in changing the material removal thresholds of thin films on substrates.

2. To determine the role of void formation within thin films and interfaces in surface roughness and material removal after fs laser irradiation.

To determine the role of the interaction of laser light with thin films in blister and microtube formation.

1. To demonstrate the ability of forming blisters at metal-SiO_2 interfaces.

2. To identify the role of decreasing film thickness on blister and microtube formation at metal-SiO_2 interfaces.

Explore the role of interfaces in the behavior of light at the interface and the formation of LIPS.

1. To demonstrate the possibility of forming LIPS after a single shot and controlling their orientation.

2. Characterize LIPS formation to further understand LIPS morphology and the behavior of light at different interfaces.

3. To establish the mechanisms of LIPS formation by changing the laser polarization orientation with surface features.

4. To establish a time scale for LIPS formation using pump-probe microscopy to understand the dynamics of LIPS formation.

Identify the response of CNT-polymer composites to fs laser irradiation.

1. To identify the role of interfaces in the irradiation of CNT-polymer composites.

2. To demonstrate the possibility of changing the morphology of CNT-polymer composites without damaging CNTs.

3. To use the interaction of ultrafast laser pulses with CNT-polymer composites to change the electrical properties of composite films.

Applications of discovered mechanisms.

1. To demonstrate NP formation from the fs irradiation of thin films.

2. To print catalyst Ni NPs particles onto a substrate and demonstrate CNT growth using the NPs.

3. To demonstrate the ability to form microfluidic tubes and flexible mircrofluidics at metal-SiO_2 interfaces.

The impact of this thesis is the interaction of ultrafast laser light with interfaces allows for the ability to change material properties in manners otherwise not possible. It demonstrates that where interfaces exist, the response of the interface to fs irradiation cannot be ignored. Being able to change the performance of materials using rapid methods will play pivotal roles in creating new devices with unique material properties.

References

D. C. Emmony, R. P. Howson, and L. J. Willis, *Laser mirror damage in germanium at 10.6 μm*, Applied Physics Letters **23**, 598 (1973).

E. Fortunato, P. Barquinha, and R. Martins, *Oxide semiconductor thin-film transistors: A review of recent advances*, Advanced Materials **24**, 2945 (2012).

C. Guo, G. Rodriguez, A. Lobad, and A. J. Taylor, *Structural phase transition of aluminum induced by electronic excitation*, Physical Review Letters **84**, 4493 (2000).

Z. Guosheng, P. M. Fauchet, and A. E. Siegman, *Growth of spontaneous periodic surface structures on solids during laser illumination*, Physical Review B **26**, 5366 (1982).

S. Kumar, B. A. Cola, R. Jackson, and S. Graham, *A review of carbon nanotube ensembles as flexible electronics and advanced packaging materials*, Journal of Electronic Packaging **133**, 020906 (2011).

M. Pessot, J. Squier, G. Mourou, and D. J. Harter, *Chirped-pulse amplification of 100-fsec pulses*, Optics Letters **14**, 797 (1989).

P. N. Saeta, J. K. Wang, Y. Siegal, N. Bloembergen, and E. Mazur, *Ultrafast electronic disordering during femtosecond laser melting of GaAs*, Physical Review Letters **67**, 1023 (1991).

J. E. Sipe, J. F. Young, H. M. van Driel, *Laser-induced periodic surface structure. I. Theory*, Physical Review B 27, 2 (1983).

H. W. K. Tom, G. D. Aumiller, and C. H. Brito-Cruz, *Time-resolved study of laser-induced disorder of Si surfaces*, Physical Review Letters **60**, 1438 (1988).

Chapter 2
Background

A review of previous research on the interaction of fs laser pulses with materials and the removal thresholds, resulting morphology, and dynamics is presented in this chapter. The first part of this chapter will focus on single pulse interactions and morphology, and the last part will focus on surface morphology after irradiation with multiple laser shots.

Section 2.1 Femtosecond Laser Irradiation

The majority of this thesis will be focused on fs laser irradiation of metals and semiconductors, so this section discusses material removal mechanisms after irradiation of these bulk materials.

Nanosecond laser thresholds of materials, particularly metals, are governed by excitation of electrons to high energy states in the conduction band and thermalization with the lattice through electron-phonon coupling [Fujimoto 1984]. The electron-phonon coupling times are much shorter than the pulse length of the laser, meaning that the laser is still on while material removal is still occurring. As a result, the damage thresholds of materials for ns laser irradiation are not well defined and rough surfaces are produced. It has been found that damage threshold fluence for metals and semiconductors decreases with pulse length, so fs laser damage thresholds are much smaller than those for ns laser irradiation [Momma 1996, Pronko 1995, Preuss 1994, Wellershoff 1998]. The dynamics of material removal after fs laser irradiation result in deterministic thresholds, which will be discussed in detail below. Damage thresholds after fs laser irradiation are measured with optical microscopy [McDonald 2005], scanning electron microscopy (SEM) [McDonald 2005, Weingärtner 1999], and atomic

force microscopy (AFM) [Bonse 2002]. The Gaussian shape of the laser pulse is used to correlate the damage size with the amount of energy in the pulse to determine peak and average laser fluences [Borowiec 2004]. In this thesis, the stated fluences are always given as peak fluences.

Section 2.1.2 Models and Mechanisms for Material Removal from Metals and Semiconductors

The dynamics of material removal after irradiation with fs laser pulses are simpler than irradiation with ns laser pulses since the laser light is "on" for much shorter time scales than the electron-phonon coupling times [Sun 1994]. For metals, the laser energy is absorbed by electrons in the conduction band which are then excited to higher energy states. Within 1 ps, excited electrons lose their energy via collisions with with other electrons and through electron-phonon coupling with the lattice and the surface melts [Rethfeld 2004, Sun 1994, Hohlfeld 2000].

For semiconductors, using pump-probe microscopy, the first evidence for ultrafast melting of Si was shown [Downer 1985]. Near the material removal threshold of Si, molten Si was observed within ~ 1 ps, after which a dome of molten material rising off the surface was visible a few picoseconds later. This dome is visible from the interference of reflected fs probe light off the surface of the expanding molten dome of Si and the underlying molten Si below the dome, and will be used to investigate material from Si in Chapter 6 of this thesis. The interference of the two reflections produces interference rings, allowing for velocity estimates of the expanding dome. For semiconductors such as Si, with bandgaps lower than the energy of single photons, ~ 10% of the valence electrons are excited into the conduction band and electron-hole pairs are formed. The reflectivity of the surface then increases and the absorption depth decreases, due to formation of the plasma [Stampfli 1994, Pronko 1998]. Within 1 ps, the electrons and holes are in thermal equilibrium and the first few nm's of the Si melts after the electron energy is transferred to the atomic lattice via electron-phonon coupling; these processes are addressed with a two-temperature model [Rethfeld 2002]. At low fluences for Si (~ 0.20 J/cm^2), thermalization leads to melting of the first

few nanometers of the Si surface. Amorphous Si forms when the molten Si thermally quenches with bulk Si [Bonse 2004]. Material removal doesn't occur until a fluence of ~ 0.30 J/cm^2 is reached, after which the following has been reported in the literature to occur.

After melting and before the expansion associated with the liquid transition is concluded, high temperature collisions within the hot liquid set up extreme pressure gradients at the free surface-liquid-bulk interfaces. The pressure gradients drive expansion of the liquid from the free surface away from the sample, launching a compressive wave into the sample. The local pressure within the liquid goes negative as a rarefaction wave forms in the liquid and vacancies within the liquid coalesce into voids along a plane within the melt [Rethfeld 2002, Reis 2006]. The ejection of a liquid layer results along this plane. The coalescence of voids along this plane is responsible for the deterministic nature of material removal from metals and semiconductors and allows us to directly correlate damage size, such as craters in the material surface after a single laser shot, to a specific fluence. Smooth surfaces after single laser shots have been reported [Bonse 2002] and are the direct result of the nature of void formation in the bulk. The void nucleation discussed above is homogeneous within bulk material but is not usually connected with smooth crater surfaces in the literature. Chapter 4 of this thesis will explain the removal of material from within bulk materials in more detail and will relate homogeneous void nucleation within bulk to material removal within thin films. It will be shown for the first time that the nature of void nucleation has direct effects on surface roughness.

Insulators have much larger bandgaps than semiconductors and therefore have fs laser damage thresholds which are an order of magnitude larger than the thresholds for metals and semiconductors discussed above [Stuart 1996]. The mechanisms for damage now involve multiphoton excitation of electrons from the valence band to the conduction band and once a critical density of electrons is produced, Coulomb explosion and material removal occurs [Gamaly 2002].

Section 2.2 Nanoparticle Formation After Laser Irradiation

The mechanisms of fs irradiation and material removal discussed in the previous section are used to machine materials with better control of material removal and smaller heat affected zones compared to ns irradiation [Krüger 1999]. In the process of repeatedly irradiating material surfaces above their damage thresholds, a significant amount of material ejection occurs. It has been found that this molten material has dimensions on the order of a few nanometers to several hundred nanometers with a range of compositions, depending on the irradiation conditions [Lowndes 1996]. The debris forms through melting, expansion of the melt, and ejection from the substrate; the cooling rate depends on the irradiation conditions but usually takes time periods of several nanoseconds to milliseconds [Marine 2000]. The particle sizes vary depending on the irradiation conditions, but nanoparticles (diameter $\lesssim$ 100 nm) can be produced in large quantities and are desired for various applications. The majority of experiments for nanoparticle (NP) production involve irradiation of bulk materials with many laser pulses in air [Barcikowski 2007], water [Kabashin 2003], vacuum [Amoruso 2005], and in the presence of ambient background gases introduced into the chamber during irradiation [Barcikowski 2007]. Pulsed laser deposition (PLD) of nanoparticles is the most widely used technique to produce NPs using laser irradiation because of the ability to form NPs with narrow size distributions. Investigation of the plume formation and subsequent cooling has been performed using spectroscopy in a number of studies [Lowndes 1996], and the plume dynamics may be correlated to NP morphology and sizes [Haverkamp 2003, Anisimov 1993]. In addition to using pulse duration to control plume dynamics, the presence of ambient gases during PLD can be used to control NP size [Sturm 2003], but the downside to this technique is that fine control of the gas pressure must be maintained in order to control the NP size distributions. However, more control over NP formation is gained when when PLD is performed in vacuum, which avoids the complications when ambient background gases are used [Amoruso 2005].

Nanoparticles for applications such as CNT growth using chemical vapor deposition [Ren 1998] are also commonly produced by dewetting thin films of transition

metals such as Fe, Ni, Co, and Mo through heating [Cantoro 2006]. The film is slowly heated until it melts and surface tension of the molten film will cause the film to dewet into islands which have nanoscale dimensions [Jiran 1990]. But this method does not allow for very precise control of NP size; while control of the catalyst size is important since many studies have linked the catalyst NP size to the diameter of CNTs after growth [Wei 2001, Ho 2001]. To gain more control over CNT growth using CVD, processes are currently available and being developed to control the location of CNT growth by precisely placing NPs on a substrate. These methods include patterning the catalyst nanoparticles with lithographic techniques [Huang 2002, Franklin 2001], stamping solutions of NPs onto the substrate [Kind 2000], and ink-jet printing of NPs [Ago 2003]. Printing of NPs both in vacuum and in the presence of background gases has been demonstrated by using the ns laser irradiation of thin films [Murray 2008], but this technique has not yet been extended to NP printing after the fs irradiation of thin films.

Section 2.3 Laser Irradiation of Carbon Nanotubes

Laser irradiation of CNTs has been pursued in order to attempt to machine and change CNT properties after growth of the CNTs. Initial studies using continuous wave laser irradiation have shown above a threshold, smaller diameter CNTs are removed from substrates first [Corio 2002] and with increasing laser fluence CNTs are broken up into smaller C_n clusters and amorphous carbon [Ma 1999]. Femtosecond irradiation of CNTs is a largely unexplored topic, but has been shown useful for the machining of groups of CNT pillars using shockwaves [Chang 2008]. More controlled studies have used the polarization dependent properties of light absorption by CNTs [Murakami 2005] to selectively remove CNTs from a substrate which are oriented parallel to the electric field of the laser [Kocabas 2004]. The remaining aligned CNTs on the substrate were used to build a field effect transistor. Femtosecond irradiation of CNTs on a glass substrate have even been used to ablate the glass neighboring CNTs using the electric field enhancements in the vicinity of the CNTs [Guo 2008].

These studies have explored the interaction of laser pulses with CNTs but have not shown controlled alignment of the CNTs using fs laser irradiation. Chapter 7 of this thesis will show that alignment of CNTs may be controlled without damaging the CNTs or ablating them from the substrate.

Section 2.4 Laser Irradiation of Thin Films

The irradiation of thin films by fs and nanosecond (ns) laser pulses [Kuznetsov 2009, Kaganovskii 2006, Trice 2007, Koch 2005, Nakata 2003] have been used for many years to change surface morphology. Depending on the film and irradiation conditions, melting and dewetting of the film or delamination of the film is induced by fs, ps, and ns laser pulses.

The morphology of thin films has been shown to change during ns irradiation using multibeam interference lithography [Kaganovski 2006, Xiao 2010] and also multiple pulse irradiation [Trice 2007]. After the film melts, it dewets, and as the surface cools a surface roughness on the nano-scale forms. On these same time scales, the removal threshold of Ni thin films using ns laser pulses was also investigated [Röder 2012] and found to depend on film thickness. Surface morphology can also be controlled by printing using the Laser Induced Forward Transfer (LIFT) process [Bohandy 1986, Bera 2007, Banks 2006, Yang 2006]. This process uses laser irradiation to melt the film, and forward momentum of the expanding molten material ejects the film from the donor substrate onto an acceptor substrate. Variations of the LIFT process were discussed in the previous section as they were applied to nanoparticle formation. It was found in [Bera 2007] that more control over the morphology of printed films using the LIFT technique may be achieved by using fs laser pulses. Multiple methods using fs irradiation can control thin film surface morphology, including delamination of Au films [Kuznetsov 2009, Koch 2005, McDonald 153121 (2006)] and the LIFT technique [Bera 2007, Banks 2006]. This is because femtosecond laser pulses interact with the material on time scales that are short relative to the material's atomistic response. For instance, after fs irradiation of thin films, ballistic electron confinement has been shown to decrease the melt threshold of Ni films below a

60 nm thickness [Güdde 1998, Wellershof 1999], but the mechanisms of material removal from the interface have not been studied. The dependence of material removal from thin films and the resulting surface roughness on film thickness and laser fluence after fs irradiation remains a largely unexplored topic. Homogeneous void nucleation with molten material initiates material removal near the threshold, but the presence of defects at interfaces are never discussed after the irradiation of thin films or their role as sites for heterogeneous void nucleation.

Without melting the film, the role of the interface has been explored in the delamination and buckling of SiO_2 thin films from Si substrates [McDonald 2007]. By studying dynamics of the thin film removal using pump-probe microscopy [McDonald 2007], these studies found that buckling (blistering) of the SiO_2 thin films is initiated after absorption of the laser pulse and melting of the underlying Si. Blister formation was only observed above the ablation threshold of Si; additionally the blister dimensions were larger than buckling mechanics of clamped circular plates predicted for the given stress of the films [McDonald 2010]. Since blistering was only observed above the Si ablation threshold, these results were attributed to a combination of both ablation and buckling of the film playing a role in blister formation. The ability to form microtubes at a Si-SiO_2 interface was also demonstrated [McDonald 2006] by overlapping successive laser pulses, but microtube formation was not explored at metal-SiO_2 interfaces. The role of the underlying Si substrate has also not been addressed in these studies. One study showed that the underlying substrate has an effect on buckling of the overlying SiO_2 film and was performed with ns laser pulses [Serrano 2002]. In that study the laser pulse was still on while the blister forms, and heat transfer from the underlying substrate to the SiO_2 induced collapse of the SiO_2. After fs irradiation, estimates of the temperatures of the molten Si underneath the SiO_2 thin film show that the Si temperatures far exceed the glass transition temperature of SiO_2 film; therefore, the role of the substrate cannot be ignored in the formation of blisters at interfaces and is further addressed in this thesis.

In summary, the interaction of fs laser pulses with thin films have been studied for a number of years, but the presence of the interface is not usually accounted for. Material removal and the dependence of the surface morphology will both be shown in

this thesis to be unique at the interface; therefore the role of the interface cannot be excluded from physical models seeking to explain the interaction of fs lasers with thin films.

Section 2.5 Laser Induced Periodic Structures

In this section, the polarization direction of the beam will be defined by the direction of the incident electric field "$\vec{E}$". The convention for polarization orientation will be used where electric fields perpendicular to the plane of incidence are transverse electric (TE), and magnetic fields perpendicular to the plane of incidence are transverse magnetic (TM).

LIPS are a corrugation of material surfaces after irradiation with laser pulses and appear to be a universal phenomenon. LIPS formation is usually studied in air, but complex micro- and nanostructures have also been observed to form on surfaces after irradiation in other environments such as water [Shen 2008]. LIPS have been observed with periodicities both approximately equal to the fundamental laser wavelength λ and much shorter than λ. LIPS with periods much shorter than λ are only observed after multiple shots and on metals and semiconductors they coexist with LIPS periods ~ λ [Dufft 2009, Crawford 2007, Honda 2010, Costache 2004]. Their orientations have been observed both perpendicular and parallel to $\vec{E}$. LIPS with periods much shorter than λ can also be formed inside insulators after laser irradiation *and* chemical etching [Hnatovsky 2006].

The focus of Chapter 6 of this thesis will be on LIPS formation with periods ~ λ so the following review of LIPS formation will be mostly focused on LIPS with periods near λ.

Section 2.5.1 Theories of Laser Induced Periodic Structures Formation with Periods Near λ

LIPS formation with periodicities ~ λ is generally attributed to the interaction of the laser light with defects on the material surface [Guosheng 1982, Sipe 1983]. If a pre-existing, surface defect is not initially present on a surface, only a crater is formed after irradiation by a single laser pulse. The scattering of light from isolated surface defects [Bonse 2009] and rough surfaces [Sipe 1983, Garrelie 2011], interaction of light with plasmonic nanostructures which are designed to only radiate light when surface plasmon polaritons (SPPs) are excited (Mie scattering) [Obara 2011], and the excitation of SPPs on surfaces [Guosheng 1982, Garrelie 2011, Bonse 2011] have been proposed to play major roles in LIPS formation after irradiation with multiple laser shots.

LIPS were first observed on the surface of Ge mirrors after irradiation of scratches with single 80 ns laser shots [Emmony 1973], and the LIPS orientation was parallel to the scratches. It was hypothesized that LIPS formed from a periodic variation of light intensity at the material surface, resulting from the interference of a scattered wave with the incident laser light. The Rayleigh diffraction condition $\frac{2\pi n}{\lambda}(\sin\theta + \sin\theta') = \pm m\frac{2\pi}{\Lambda}$ for gratings, where Λ is the grating period, was used to predict the condition for a wave of wavelength λ incident on a feature to be scattered at grazing incidence θ' = 90° along the diffracting surface. The index of refraction n of the air above the grating surface is ~ 1, so the condition $\Lambda = \frac{\lambda}{1 \pm \sin\theta}$, where Λ is the period of the LIPS, was derived to predict the change in Λ with a changing angle of incidence θ. More research followed soon after which showed LIPS can form after multiple shots without a pre-existing scratch in various materials, and LIPS were almost always formed with an orientation perpendicular to the direction of $\vec{E}$. However, more detailed investigations showed that this simple classical model doesn't hold and that Λ is rarely exactly equal to λ.

Both the polarization and Λ dependence of LIPS after irradiation with multiple laser shots was explained by Siegman [Guosheng 1982]. They showed that if the material surface is already corrugated at a period equal to the laser wavelength λ, light will be coupled into the surface at a period Λ which strongly depends on the polarization direction. If the laser polarization was perpendicular to the direction of the grating at normal incidence (TM) then the incident laser light is strongly coupled into the material surface at a period Λ which is slightly less than λ. This shift in period Λ from λ was attributed to the stimulation of "Wood's anomaly". Wood's anomaly was initially discovered by Robert Wood [Wood 1902] as he varied the angle of incidence of TE and TM light striking diffraction gratings and noticed a decrease in reflected light at specific angles, "This uneven distribution [of light] is carried to a degree almost incomprehensible."

The decrease in reflectivity was later attributed to scattering of TM laser light parallel to the surface [Rayleigh 1907], which can in turn excite SPPs at the near field of the surface of the diffraction grating [Hessel 1965]. SPPs are the result of light coupled to fields at a metallic surface; they travel along the surface and are non-radiative. It was also proposed by Siegman that the theory could allow for LIPS formation for TE light, but that TM light will govern LIPS formation. TM light dominates LIPS formation since the energy flux into the surface (the Poynting vector) for TE light is 2 orders of magnitude lower than that for TM light, since SPP excitation is prohibited for TE light with respect to (w.r.t.) surface features [Zayats 2005]. Van Driel [Sipe 1983] further showed that SPP excitation and LIPS growth may occur within a region of the material surface which is randomly rough, termed the "selvedge" region, and the coupling was strongest for TM light. The selvedge region is the region parallel to the sample which encompasses local variations in the surface profile of the sample and separates the homogenous bulk sample from vacuum. Their approach treated the selvedge region as the superposition of multiple diffraction gratings with different grating periods. The incident laser light interacts with all of the different grating periods but absorption in the material surface is strongest with the periods which are close to λ.

Since rough metal surfaces support SPP excitation, the Siegman and van Driel theories may be applied to LIPS formation in metals above the damage threshold of the

particular metal [Bonse 2012, Okamuro 2010]. For semiconductors, LIPS form above fluences at which the excited carrier density exceeds ~ 10^{21} cm^{-3}, where SPP coupling may occur with defects and gratings which are already present on the surface [Bonse 2009]. SPP excitation is directly related to the dielectric function of the material, which changes depending on the density of excited carriers in the semiconductor. Therefore the LIPS Λ for semiconductors is highly dependent on fluence. When laser intensities are high enough to trigger nonlinear interactions, irradiation with multiple laser shots can also generate higher harmonics. LIPS with Λ ~ 400 nm, the second harmonic of the incident 800 nm, are only observed when the carrier densities reach ~ 10^{22} cm^{-3}, at which the surface is absorbing to 400 nm light [Dufft 2009]. For semiconductors with increasing pulse number, LIPS with Λ slightly shorter than that predicted by Siegman and van Driel may coexist with longer Λ through coupling with the grating initially formed by LIPS [Bonse 2010]. With an increasing number of laser pulses, SPP coupling to the grating is enhanced and the grating deepens. As the grating deepens, the SPP coupling with the grating experiences a shift to slightly shorter Λ.

If the laser fluence is decreased below the single shot damage threshold of the material, thousands of laser shots can still form LIPS with Λ ~ λ [Tan 2006]. Irradiating the same area of a surface below the damage threshold can accumulate defects, and these defects eventually form above the material surface and scatter laser light along the surface and form LIPS with Λ ~ λ. LIPS after many shots on semiconductors form with both Λ ~ λ and Λ much shorter than λ [Costache 2004, Buividas 2011]. The reason for the coexistence of LIPS with Λ both ~ λ and much shorter than λ in metals is not currently understood [Honda 2010, Qi 2009], but the theory proposed for subsurface short Λ LIPS formation in dielectrics [Bhardwaj 2006] has been extended to the surface of semiconductors after irradiation with hundreds or thousands of laser shots [Buividas 2011].

The dynamics of LIPS formation, while rarely addressed in the literature, was originally proposed by Leamy [Leamy 1978] to be the result of the melt threshold being periodically exceeded by the interference pattern projected onto the material surface. While this may seem obvious, it has mostly only been surmised in the studies above through the observation of LIPS formation on different materials and at varying fluences

and polarization angles. The dynamics of LIPs formation have never been investigated by studying LIPS formation after irradiation with single laser pulses. The only study which at least directly confirms that LIPS formation occurs after melting was performed using a pump-probe reflection study with 20 ns laser pulses [Young 1983]. By measuring the intensity of probe light reflected from the irradiated sample, it was shown that LIPS formation occurs after the sample surface melts. However, the dynamics of LIPS formation after single laser shots using ns, ps, or fs irradiation has not been performed. Just as the LIPS period, amplitude, and orientations are highly variable depending on material type and irradiation conditions, the dynamics are likely to be equally complex. With the lack of pump-probe imaging experiments performed on LIPS formation after a *single* shot, the mechanisms of their formation are still largely unknown.

In summary, various LIPS morphologies and thresholds are presented in this section. There are many different kinds of LIPS which form on surfaces, depending on if the material irradiated is a metal, semiconductor, or insulator. LIPS almost always form only after multiple shots but are also seen after single shots. The LIPS period Λ and orientation w.r.t. the laser polarization are the most striking features of LIPS and the origin of both values depending on material type, laser λ, number of shots, and irradiation geometry are still being explored. The low number of single shot experiments means that many mechanisms of LIPS formation have likely not been decoupled, and the lack pump-probe experiments on LIPS means that the dynamics of formation have not yet been fully elucidated.

References

H. Ago, K. Murata, M. Yumura, J. Yotani, and S. Uemura, *Ink-jet printing of nanoparticle catalyst for site-selective carbon nanotube growth*, Applied Physics Letters **82**, 811 (2003).

S. Amoruso, G. Ausanio, R. Bruzzese, M. Vitiello, and X. Wan, *Femtosecond laser pulse irradiation of solid targets as a general route to nanoparticle formation in a vacuum*, Physical Review B **71**, 033406 (2005).

S. I. Anisimov, D. Bäuerle, B. S. Luk'yanchuk, *Gas dynamics and film profiles in pulsed-laser deposition of materials*, Physical Review B **48**, 12076 (1993).

D. P. Banks, C. Grivas, J. D. Mills, I. Zergioti, and R. W. Eason, *Nanodroplets deposited in microarrays by femtosecond Ti:sapphire laser-induced forward transfer*, Applied Physics Letters **89**, 193107 (2006).

S. Barcikowski, A. Hahn, A. V. Kabashin, and B. N. Chichkov, *Properties of nanoparticles generated during femtosecond laser machining in air and water*, Applied Physics A **87**, 47 (2007).

S. Bera, A. J. Sabbah, J. M. Yarbrough, C. G. Allen, and B. Winters, *Optimization study of the femtosecond laser-induced forward-transfer process with thin aluminum films*, Applied Optics **46**, 4650 (2007).

V. Bhardwaj, E. Simova, P. Rajeev, C. Hnatovsky, R. Taylor, D. Rayner, and P. Corkum, *Optically produced arrays of planar nanostructures inside fused silica*, Physical Review Letters **96**, 57404 (2006).

J. Bohandy, B. F. Kim, and F. J. Adrian, *Metal deposition from a supported metal film using an excimer laser*, Journal of Applied Physics **60**, 1538 (1986).

J. Bonse, S. Baudach, J. Kruger, W. Kautek, and M. Lenzner, *Femtosecond laser ablation of silicon–modification thresholds and morphology*, Applied Physics A **74**, 19 (2002).

J. Bonse, K. W. Brzezinka, and A. J. Meixner, *Modifying single-crystalline silicon by femtosecond laser pulses: an analysis by micro Raman spectroscopy, scanning laser microscopy and atomic force microscopy*, Applied Surface Science **221**, 215 (2004).

J. Bonse and J. Krüger, *Pulse number dependence of laser-induced periodic surface structures for femtosecond laser irradiation of silicon*, Journal of Applied Physics **108**, 034903 (2010).

J. Bonse, J. Krüger, S. Höhm, and A. Rosenfeld, *Femtosecond laser-induced periodic surface structures*, Journal of Laser Applications **24**, 042006 (2012).

J. Bonse, A. Rosenfeld, J. Krüger, *On the role of surface plasmon polaritons in the formation of laser-induced periodic surface structures upon irradiation of silicon by femtosecond laser pulses*, Journal of Applied Physics **106**, 104910 (2009).

J. Bonse, J. M. Wrobel, K. -W. Brzezinka, N. Esserd, and W. Kautek, *Femtosecond laser irradiation of indium phosphide in air: Raman spectroscopic and atomic force microscopic investigations*, Applied Surface Science **202**, 272 (2002).

A. Borowiec, and H. K. Haugen, *Femtosecond laser micromachining of grooves in indium phosphide*, Applied Physics A **79**, 521 (2004).

R. Buividas, L. Rosa, R. Šliupas, T. Kudrius, G. Šlekys, V. Datsyuk, and S. Juodkazis, *Mechanism of fine ripple formation on surfaces of (semi)transparent materials via a half-wavelength cavity feedback*, Nanotechnology **22**, 055304 (2011).

M. Cantoro, S. Hofmann, S. Pisana, V. Scardaci, A. Parvez, C. Ducati, A. C. Ferrari, A. M. Blackburn, K. Wang, and J. Robertson, *Catalytic chemical vapor deposition of single-wall carbon nanotubes at low temperatures*, Nano Letters **6**, 1107 (2006).

W. Chang, B. Yoo, and S. Cho, *Modification of Carbon Nanotube Templates Using Femtosecond Laser Pulses*, The Japanese Journal of Applied Physics **47**, 6998 (2008).

P. Corio, P. S. Santos, M. A. Pimenta, and M. S. Dresselhaus, *Evolution of the molecular structure of metallic and semiconducting carbon nanotubes under laser irradiation*, Chemical Physics Letters **360**, 557 (2002).

F. Costache, S. Kouteva-Arguirova, and J. Reif, *Sub-damage-threshold femtosecond laser ablation from crystalline Si: surface nanostructures and phase transformation*, Applied Physics A **79**, 1429 (2004).

T. H. R. Crawford and H. K. Haugen, *Sub-wavelength surface structures on silicon irradiated by femtosecond laser pulses at 1300 and 2100 nm wavelengths,* Applied Surface Science **253**, 4970 (2007).

M. C. Downer, R. L. Fork, and C. V. Shank, *Femtosecond imaging of melting and evaporation at a photoexcited silicon surface*, Journal of the Optical Society of America B **2**, 595 (1985).

D. Dufft, A. Rosenfeld, S. K. Das, R. Grunwald, and J. Bonse, *Femtosecond laser-induced periodic surface structures revisited: A comparative study on ZnO*, Journal of Applied Physics **105**, 034908 (2009).

T. Dumitrica, M.E. Garcia, H. O. Jeschke, and B. I. Yakobson, *Breathing coherent phonons and caps fragmentation in carbon nanotubes following ultrafast laser pulses*, Physical Review B **74**, 193406 (2006).

D. C. Emmony, R. P. Howson, and L. J. Willis, *Laser mirror damage in germanium at 10.6 μm*, Applied Physics Letters **23**, 598 (1973).

N. R. Franklin, Y. Li, R. J. Chen, A. Javey, and H. Dai, *Patterned growth of single-walled carbon nanotubes on full 4-inch wafers*, Applied Physics Letters **79**, 4571 (2001).

J. G. Fujimoto, J. M. Liu, E. P. Ippen, N. Bloembergen, *Femtosecond laser interaction with metallic tungsten and nonequilibrium electron and lattice temperatures*, Physical Review Letters **53**, 1837 (1984).

E. G. Gamaly, A. V. Rode, V. T. Tikhonchuk, and B. Luther-Davies, *Electrostatic mechanism of ablation by femtosecond lasers*, Applied Surface Science **197-198**, 699 (2002).

F. Garrelie, J. P. Colombier, F. Pigeon, S. Tonchev, N. Faure, M. Bounhalli, S. Reynaud, and O. Parriaux, *Evidence of surface plasmon resonance in ultrafast laser-induced ripples*, Optics Express **19**, 9035 (2011).

J. Güdde, J. Hohlfeld, J. G. Müller, and E. Matthias, *Damage threshold dependence on electron–phonon coupling in Au and Ni films*, Applied Surface Science **127**, 40 (1998).

S. X. Guo and A. Ben-Yakar, *Femtosecond laser nanoablation of glass in the near-field of single wall carbon nanotube bundles*, Journal of Physics D: Applied Physics **41**, 185306 (2008).

Z. Guosheng, P. M. Fauchet, and A. E. Siegman, *Growth of spontaneous periodic surface structures on solids during laser illumination*, Physical Review B **26**, 5366 (1982).

J. Haverkamp, R. M. Mayo, M. A. Bourham, J. Narayan, C. Jin, and G. Duscher, *Plasma plume characteristics and properties of pulsed laser deposited diamond-like carbon films*, Journal of Applied Physics **93**, 3627 (2003).

A. Hessel and A. A. Oliner, *A new theory of wood's anomalies on optical gratings*, Applied Optics **4**, 1275 (1965).

C. Hnatovsky, R. S. Taylor, E. Simova, P. P. Rajeev, D. M. Rayner, V. R. Bhardwaj, and P. B. Corkum, *Fabrication of microchannels in glass using focused femtosecond laser radiation and selective chemical etching*, Applied Physics A **84**, 47 (2006).

G. W. Ho, A. T. S. Wee, J. Lin, and W. C. Tjiu, *Synthesis of well-aligned multiwalled carbon nanotubes on Ni catalyst using radio frequency plasma-enhanced chemical vapor deposition*, Thin Solid Films **388**, 73 (2001).

J. Hohlfeld, S. S. Wellershoff, J. Gudde, U. Conrad, V. Jahnke, and E. Matthias, *Electron and lattice dynamics following optical excitation of metals*, Chemical Physics **251**, 237 (2000).

H. Honda, M. Tsukamoto, N. Abe, T. Shinonaga, & M. Fujita (2010). *Microstructres formed on stainless steel by femtosecond laser irradiation*. Online: Wiley Online Library.

S. Huang, L. Dai, and A. W. H. Mau, *Controlled fabrication of large-scale aligned carbon nanofiber/nanotube patterns by photolithography*, Advanced Materials **14**, 1140 (2002).

E. Jiran and C. V. Thompson, *Capillary instability in thin films*, Journal of Electronic Materials **19**, 1153 (1990).

A. V. Kabashin and M. Meunier, *Synthesis of colloidal nanoparticles during femtosecond laser ablation of gold in water*, Journal of Applied Physics **94**, 7941 (2003).

Y. Kaganovskii, H. Vladomirsky, and M. Rosenbluh, *Periodic lines and holes produced in thin Au films by pulsed laser irradiation*, Journal of Applied Physics **100**, 044317 (2006).

H. Kind, J. M. Bonard, L. Forró, K. Kern, K. Hernadi, L. O. Nilsson, and L. Schlapbach, *Printing gel-like catalysts for the directed growth of multiwall carbon nanotubes*, Langmuir **16**, 6877 (2000).

C. Kocabas, M. A. Meitl, A. Gaur, M. Shim, and J.A. Rogers, *Aligned arrays of single-walled carbon nanotubes generated from random networks by orientationally selective laser ablation*, Nano Letters **4**, 2421 (2004).

J. Koch, F. Korte, T. Bauer, C. Fallnich, A. Ostendorf, and B. N. Chichkov, *Nanotexturing of gold films by femtosecond laser-induced melt dynamics*, Applied Physics A **81**, 325 (2005).

J. Krüger and W. Kautek, *The femtosecond pulse laser: A new tool for micromachining*, Laser Physics **9**, 30 (1999).

A. I. Kuznetsov, J. Koch, and B. N. Chichkov, *Nanostructuring of thin gold films by femtosecond lasers*, Applied Physics A **94**, 221 (2009).

H. J. Leamy, G. A. Rozgonyi, T. T. Sheng, and G. K. Celler, *Periodic regrowth phenomena produced by laser annealing of ion-implanted silicon*, Applied Physics Letters **32** 535 (1978).

D. H. Lowndes, D. B. Geohegan, A. A. Puretzky, D. P. Norton, and C. M. Rouleau, *Synthesis of novel thin-film materials by pulsed laser deposition*, Science **273**, 898 (1996).

R. Z. Ma, B. Q. Wei, C. L. Xu, J. Liang, D. H. Wu, *The morphology changes of carbon nanotubes under laser irradiation*, Carbon **38**, 623 (200).

W. Marine, L. Patrone, B. Luk'yanchuk, and M. Sentis, *Strategy of nanocluster and nanostructure synthesis by conventional pulsed laser ablation*, Applied Surface Science **154-155**, 345 (2000).

J. P. McDonald, A. A. McClelland, Y. N. Picard, and S. M. Yalisove, *Role of a native oxide on femtosecond laser interaction with silicon (100) near the damage threshold*, Applied Physics Letters **86**, 264103 (2005).

J. P. McDonald, V. R. Mistry, K. E. Ray, and S. M. Yalisove, *Femtosecond pulsed laser direct write production of nano- and microfluidic channels*, Applied Physics Letters **88**, 183113 (2006).

J. P. McDonald, V. R. Mistry, K. E. Ray, S. M. Yalisove, J. A. Nees, and N. R. Moody, *Femtosecond-laser-induced delamination and blister formation in thermal oxide films on silicon (100)*, Applied Physics Letters **88**, 153121 (2006).

J. P. McDonald, J. A. Nees, and S. M. Yalisove, *Pump-probe imaging of femtosecond pulsed laser ablation of silicon with thermally grown oxide films*, Journal of Applied Physics **102**, 063109 (2007).

J. P. McDonald, M. D. Thouless, and S. M. Yalisove, *Mechanics analysis of femtosecond laser-induced blisters produced in thermally grown oxide on Si(100)*, Journal of Materials Research **25**, 1087 (2010).

C. Momma, B. Chichkov, S. Nolte, F. von Alvensleben, A. Tunnermann, H. Welling, and B. Wellegehausen, *Short-pulse ablation of solid targets*, Optics Communications **129**, 134 (1996).

Y. Murakami, E. Einarsson, T. Edamura, and S. Maruyama, *Polarization dependent optical absorption properties of single-walled carbon nanotubes and methodology for the evaluation of their morphology*, Carbon **43**, 2664 (2005).

P. T. Murray and E. Shin, *Formation of silver nanoparticles by through thin film ablation*, Materials Letters **62**, 4336 (2008).

Y. Nakata, T. Okada, and M. Maeda, *Nano-Sized Hollow Bump Array Generated by Single Femtosecond Laser Pulse*, Japanese Journal of Applied Phyics **42**, 1452 (2003).

G. Obara, N. Maeda, T. Miyanishi, M. Terakawa, N. N. Nedyalkov, and M. Obara, *Plasmonic and Mie scattering control of far-field interference for regular ripple formation on various material substrates*, Optics Express **19**, 20 (2011).

K. Okamuro, M. Hashida, Y. Miyasaka, Y. Ikuta, S. Tokita, and S. Sakabe, *Laser fluence dependence of periodic grating structures formed on metal surfaces under femtosecond laser pulse irradiation*, Physical Review B **82**, 165417 (2010).

S. Preuss, E. Matthias, and M. Stuke, *Sub-picosecond UV-laser ablation of Ni films: Strong fluence reduction and thickness-independent removal*, Applied Physics A **59**, 79 (1994).

P. P. Pronko, S. K. Dutta, J. Squier, J. V. Rudd, D. Du, and G. Mourou, *Machining of sub-micron holes using a femtosecond laser at 800 nm*, Optics Communications **114**, 106 (1995).

P. P. Pronko, P. A. V. Rompay, C. Horvath, F. Loesel, T. Juhasz, X. Liu, and G. Mourou, *Avalanche ionization and dielectric breakdown in silicon with ultrafast laser pulses*, Physical Review B **58**, 2387 (1998).

L. Qi, K. Nishii, and Y. Namba, *Regular subwavelength surface structures induced by femtosecond laser pulses on stainless steel*, Optics Letters **34**, 1846 (2009).

Lord Rayleigh, *On the dynamical theory of gratings*, Proceedings of the Royal Society of London **A79**, 399 (1907).

D. A. Reis, K. J. Gaffney, G. H. Gilmer, and B. Torralva, *Ultrafast dynamics of laser excited solids*, Materials Research Society Bulletin **31**, 601 (2006).

Z. F. Ren, Z. P. Huang, J. W. Xu, J. H. Wang, P. Bush, M. P. Siegal, and P. N. Provencio, *Synthesis of large arrays of well-aligned carbon nanotubes on glass*, Science **282**, 1105 (1998).

B. Rethfeld, K. Sokolowski-Tinten, D. von der Linde, and S. I. Anisimov, *Timescales in the response of materials to femtosecond laser excitation*, Applied Physics A **79**, 767 (2004).

B. Rethfeld, K. Sokolowski-Tinten, D. von der Linde, and S. I. Anisimov, *Ultrafast thermal melting of laser-exited solids by homogeneous nucleation*, Physical Review B **65**, 092103 (2002).

T. C. Röder and J. R. Köhler, *Physical model for the laser induced forward transfer process*, Applied Physics Letters **100**, 071603 (2012).

J. R. Serrano, and D. G. Cahill, *Micron-scale buckling of SiO_2 on Si*, Journal of Applied Physics **92**, 7606 (2002).

M. Shen, J. Carey, C. H. Crouch, M. Kandyla, H. A. Stone, and E. Mazur, *High-density regular arrays of nanometer-scale rods formed on silicon surfaces via femtosecond laser irradiation in water*, Nano Letters **8**, 2087 (2008).

J. E. Sipe, J. F. Young, H. M. van Driel, *Laser-induced periodic surface structure. I. Theory*, Physical Review B **27**, 2 (1983).

P. Stampfli and K. H. Bennemann, *Time dependence of the laser-induced femtosecond lattice instability of Si and GaAs: Role of longitudinal optical distortions*, Physical Review B **49**, 7299 (1994).

B. C. Stuart, M. D. Feit, S. Herman, A. M. Rubenchik, B. W. Shore, and M. D. Perry, *Nanosecond-to-femtosecond laser-induced breakdown in dielectrics*, Physical Review B **53**, 1749 (1996).

K. Sturm, S. Fahler, and H. U. Krebs, *Pulsed laser deposition of metals in low pressure inert gas*, Applied Surface Science **154**, 462 (2003).

C. K. Sun, F. Vallee, L. H. Acioli, E. P. Ippen, J. G. Fujimoto, *Femtosecond-tunable measurement of electron thermalization in gold*, Physical Review B **50**, 15337 (1994).

B. Tan and K. Venkatakrishnan, *A femtosecond laser-induced periodical surface structure on crystalline silicon*, Journal of Micromechanics and Microengineering **16**, 1080 (2006).

J. Trice, D. Thomas, C. Favazza, R. Sureshkumar, and R. Kalyanaraman, *Pulsed-laser-induced dewetting in nanoscopic metal films: Theory and experiments*, Physical Review B **75**, 235439 (2007).

Y. Y. Wei, G. Eres, V. I. Merkulov, and D. H. Lowndes, *Effect of catalyst film thickness on carbon nanotube growth by selective area chemical vapor deposition*, Applied Physics Letters **78**, 1394 (2001).

M. Weingärtner, R. Elschner, and O. Bostanjoglo, *Patterning of silicon-differences between nanosecond and femtosecond laser pulses*, Applied Surface Science **138-139**, 499 (1999).

S. S. Wellershof, J. Güdde, J. Hohlfeld, J. G. Müller, and E. Matthias, *The role of electron-phonon coupling in femtosecond laser damage of metals*, SPIE High Power Laser Ablation **3343**, 378 (1998).

S. S. Wellershof, J. Hohlfeld, J. Gudde, and E. Matthias, *The role of electron-phonon coupling in femtosecond laser damage of metals*, Applied Physics A **69**, S99 (1999).

R. W. Wood, *On the remarkable case of uneven distribution of light in a diffraction grating spectrum*, Proceedings of the Physical Society **18**, 269 (1902).

F. Xiao, T. Wu, and P. Y. Chiou, *Near field photothermal printing of gold microstructures and nanostructures*, Applied Physics Letters **97**, 031112 (2010).

L. Yang, C. Wang, X. Ni, Z. Wang, W. Jia, and L. Chai, *Microdroplet deposition of copper film by femtosecond laser-induced forward transfer*, Applied Physics Letters **89**, 161110 (2006).

J. F. Young, J. S. Preston, J. E. Sipe, and H. M. van Driel, *Time-resolved evolution of laser-induced periodic surface structure on germanium*, Physical Review B **27**, 1424 (1983).

A. V. Zayats, I. I. Smolyaninovb, A. A. Maradudinc, *Nano-optics of surface plasmon polaritons*, Physics Reports **408**, 131 (2005).

Chapter 3
Experimental Details

All experiments were performed with a Clark-MXR CPA-2001 Ti:sapphire pulsed laser with a 150 fs pulse length, centered at a wavelength of 780 nm, repetition rate of 1 kHz, maximum pulse energy of 1 mJ, and a Gaussian intensity profile. The resulting damage morphology was characterized using a variety of techniques using laser microscopy and commercial microscopes at the University of Michigan. The following sections detail the various sample preparation, laser irradiation, material growth, and material characterization techniques used to perform the experiments in this thesis.

Section 3.1 Sample Preparation

Prior to laser irradiation and material growth, bulk samples with metallic, semiconducting, and insulating composition were diced with a diamond scribe and cleaned with trichloroethylene, isopropanol, acetone, de-ionized (DI) water and followed by drying with dry nitrogen. Though it was found that simple cleaning with acetone to remove dust and debris from the sample often produced the same laser irradiation results (morphology and damage threshold values) as the full cleaning procedure. The full cleaning procedure was also used to clean substrates before thin film deposition. Samples which could not be cleaned when the cleaning process might affect sample morphology and/or performance prior to irradiation included polymer, graphene, and CNT samples and were irradiated as-received.

Section 3.2 Ultrafast Irradiation in Air

The setup for ultrafast s-polarized laser irradiation in air at normal incidence is shown in Figure 3.2.1. The laser beam was aligned down the optics table using 2 pinholes and focused onto the sample with a bi-convex positive focusing lens. The average laser power was measured with an Ophir Optics, LLC thermal power sensor, and the average energy per pulse was obtained by dividing the measured power by the 1 kHz repetition rate of the laser. Laser energy was varied using a half-wave plate to rotate the laser polarization, followed by a polarizing beamsplitter cube. If further attenuation was required, neutral density (ND) filters were placed after the cube to absorb laser light.

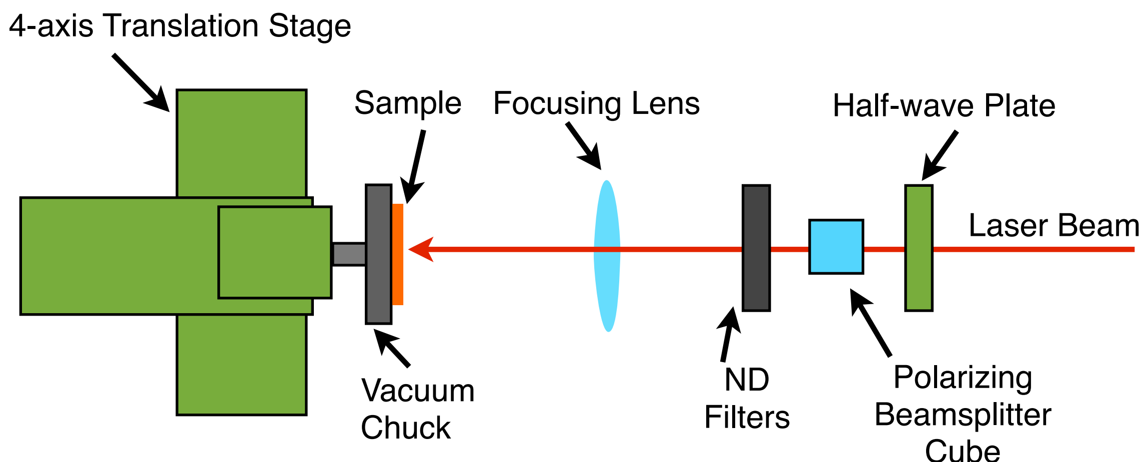

FIG 3.2.1. Ultrafast laser setup for irradiation of samples at normal incidence.

If frequency doubled light was required for the experiment, a barium borate (BBO) crystal was placed between focus and the lens with an ~ 40% conversion efficiency to 390 nm wavelength light.

Irradiation was always performed with the sample in the focus of the laser beam. The Rayleigh range bounds the edges of focus and lengthens with increasing focal length. For lenses with focal lengths ≧ 10 cm, the Rayleigh range is > 400 μm. Focus was found by placing a CCD camera in the focus of the attenuated laser beam, moving the CCD through focus to find the smallest spot, and fixing the camera to the table with a magnetic post holder. A micrometer was then placed against an ND filter in front of the CCD chip and fixed to the table in the same fashion. The CCD was removed and

the sample was placed against the micrometer. This method placed the sample within the focus of the laser beam with an accuracy of 10 μm.

For lenses with focal lengths < 10 cm, the method outlined above is either not accurate enough to reliably find focus or space limitations prevent the use of the micrometer. In these cases, focus was found by moving the sample into focus until a spark on the sample was visibly seen and then lowering the fluence. The lower fluence reduces the length of the focused beam capable of producing an air spark, so the sample is adjusted further to find the spark again. The process is repeated until step sizes of ~ 20 μm (depending on the focal length) bring the sample from a position where a spark is visible to one where the spark is not visible.

Sample placement and movement were performed using a Newport 4-axis control stage with a repeatable placement accuracy of 2.5 μm, maximum velocity of 100 mm/s, and a maximum travel length of 100 mm. The stage was programmed with LabVIEW code and controlled using a graphical user interface (Appendix 1) for velocity control and sample movement. Additional code in Appendix 1 was written to allow the user to run a for loop with included pauses to stop stage movement while the power was changed or samples exchanged.

Samples were fixed to the stage using a vacuum chuck, and the chuck was connected to house vacuum. The chuck allows samples to be held to the stage with vacuum, and an array of tapped holes interchangeably fit screws to stop air flow or accommodate pegs for sample alignment.

Section 3.3 Precise Single-Shot Ultrafast Irradiation in Air

When the experiment required precise placement of single shots, single laser pulses were isolated from the 1 kHz pulse train. A mechanical shutter placed after the focusing lens was used to block all but one laser shot but the shutter opening and closing speed, ~ 2 ms, was too slow to isolate single shots from the 1 kHz pulse train. An optical chopper wheel with a single slot was used to cut the 1 kHz repetition rate down to 100 Hz, however, instabilities in the chopper's timing box often led to instabilities in the wheel movement and random laser pulses were blocked by the

wheel. An external frequency division circuit was built and inserted between the laser's counting box and the chopper control box to circumvent the chopper's division circuits. The chopper and mechanical shutter were synced using a Princeton Scientific timing box and single laser shot operation was verified using a photodiode and oscilloscope.

Once single laser shots were isolated, a fiducial mark was created on the sample surface using multiple laser shots and was located with a microscope located on the optics table, shown in Figure 3.3.1. An "X" was then marked on the computer screen to indicate the location of laser shots on the sample. After the stage position was calibrated with the microscope position, single laser shots could be precisely placed on target, limited by the laser's pointing stability of ~ 5 µm. Several irradiation attempts on different parts of the sample were often required to place the laser spot where desired.

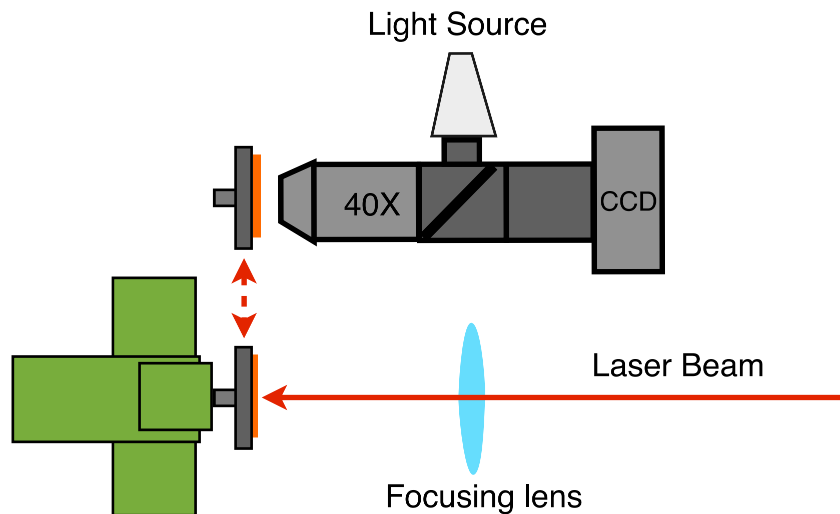

FIG. 3.3.1. Microscope setup beside the laser irradiation line used to precisely place single laser shots. Imaging of the sample was performed with a 40X objective, infinity correcting tube, and a CCD camera. Illumination was provided by an incandescent lamp.

Section 3.4 Fluence Calculations

The equation $F = \frac{2E_{Total}}{\pi ab}$ was used to calculate the peak fluence of the focused laser beam. Where F is the fluence, E_{Total} is the total energy per pulse, and a/b are the

major and minor radii at $\frac{1}{e^2}$ intensity of the focused beam, measured using a DataRay Inc. WinCamD 14-bit beam profiling CCD camera with a 20X objective attachment. A typical beam profile image of the focused beam is shown in Figure 3.4.1. Variations in the measured beam area and power corresponded to a ± 0.02 J/cm^2 variation in reported fluences. A proof that the above formula and parameters give the peak fluence is in Appendix 2.

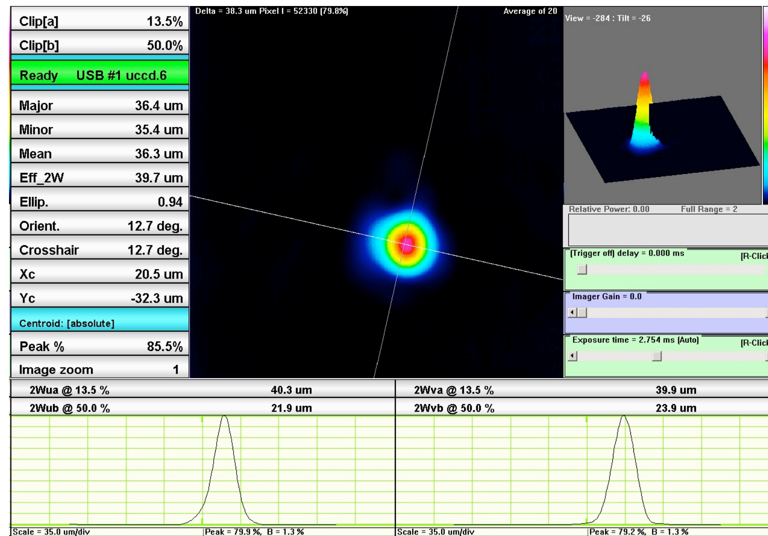

FIG 3.4.1. Typical image from the beam profiling camera for a 20 cm focal length lens.

It was often necessary to find the lowest fluence required for visible damage of the sample, the threshold fluence. The threshold fluence was calculated using the measured beam area from the beam profiling camera and the threshold energy, which was found by rastering the sample in front of the focused beam and increasing the laser power, creating increasing damage diameters. The average damage radius (average of at least 6 damage regions) was plotted against laser energy and a two parameter fit was used to interpolate the threshold energy [Borowiec 2004, Bonse 2002].

Section 3.5 Nanoparticle Collection

To study nanoparticles (NPs) created by laser irradiation in air, nanoparticles were printed onto substrates in air, using a variation of the Laser Induced Forward Transfer (LIFT) technique [Bera 2007, Banks 2006]. A scanning tunneling microscope TEM grid holder was attached to the translation stage for NP collection and a microscope cover slip holding a thin film of the material to be printed was placed in front of the TEM grid and then irradiated, shown in Figure 3.5.1. Forward momentum after irradiation propels material from the film and cover slip towards the TEM grid. Nanoparticles were also collected using a top-down irradiation approach where the film and TEM grid are in a vertical arrangement rather than the horizontal arrangement shown in Figure 3.5.1.

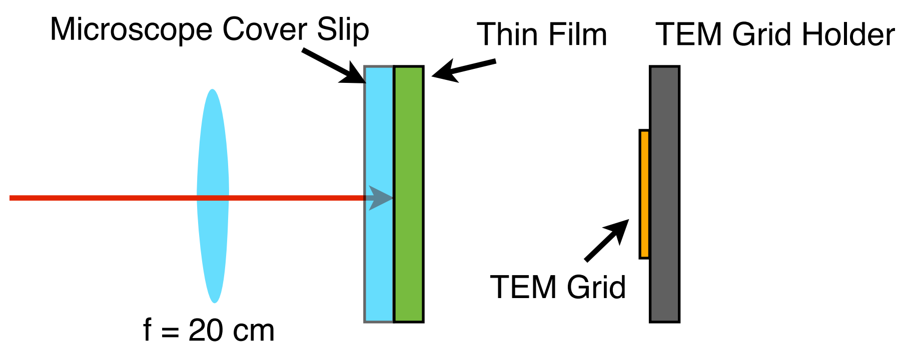

FIG. 3.5.1. Setup for printing nanoparticles onto a TEM grid substrate in air using irradiation of a thin film on a microscope cover slip.

When nanoparticle collection was performed in vacuum, the sample holder was placed in a vacuum chamber, shown in Appendix 3, and the chamber was pumped to a vacuum level of ~ 40 mTorr with an Alcatel rotary vane pump.

Section 3.6 Ultrafast Pump-Probe Microscopy Shortly After Irradiation

Dynamic changes of materials after laser irradiation were observed using pump-probe microscopy. In general, an s-polarized pump beam with a 780 nm wavelength initiates a material response to the ultrafast light and a time-delayed probe beam at a different wavelength images the resulting material response. Each time delay

represents a different irradiation event. An alternative arrangement is proposed in Appendix 4 which may allow for imaging the same irradiation event at different time steps using a 2-d optical streak camera. Pump-probe microscopy with an imaging resolution of ~ 2 μm with two different arrangements, side-view and reflection imaging, is shown in Figure 3.6.1; a similar setup has also been used to study thin film delamination [McDonald 2006].

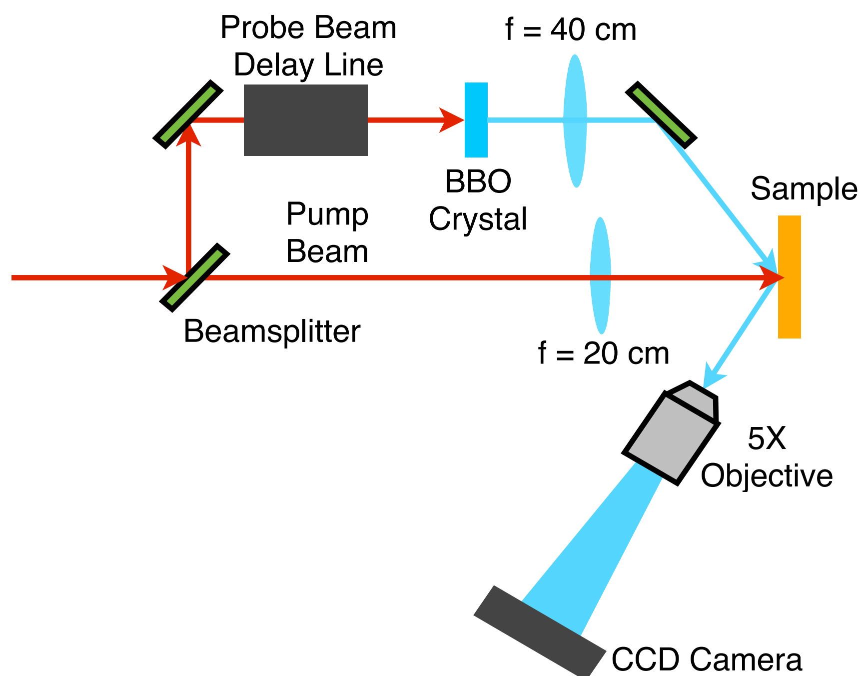

FIG. 3.6.1. Pump-probe microscopy with reflection imaging geometry.

Both the pump and probe beam required single shot operation, but the original beam diameter (~ 12 mm) was too large to fit through the mechanical shutter aperture (~ 6 mm). Therefore, a beam reducing telescope was employed to reduce the beam size to an ~ 4 mm diameter, detailed in Figure 3.6.1. The pump beam irradiates the sample at normal incidence and the probe beam is delayed by 4 passes with retro-reflecting mirrors mounted on a Velmex delay stage, programmed by Casey Wolf. This mechanical delay stage gives a maximum time delay of 12 ns, and a minimum step size of 2 μm which gives a minimum time step of 0.06 ps. After delay the probe beam was focused using an f = 40 cm lens and a BBO crystal placed after the lens was used to

convert the fundamental light into 390 nm light. Uniformly lit images were only obtained when a pin hole was tightly closed around the beam directly before the f = 40 cm lens. Filters were placed before and after the sample in the probe line to illuminate the event with 390 nm probe light; the fundamental light from the pump beam may be filtered out and not imaged by the CCD camera. After imaging the event, the probe beam passes through a 5X objective and enters a CCD camera ~ 60 cm behind the objective.

The time at which the pump and probe beam reach the sample at the same time could be determined to ~ 2 ps by noting the time step at which molten Si was observed, indicated by an increase in sample reflectivity [Downer 1985].

For observation of ripple formation, a normal incidence pump-probe setup was built. The setup is detailed in Figure 3.6.2 and employs white light imaging of the sample at normal incidence.

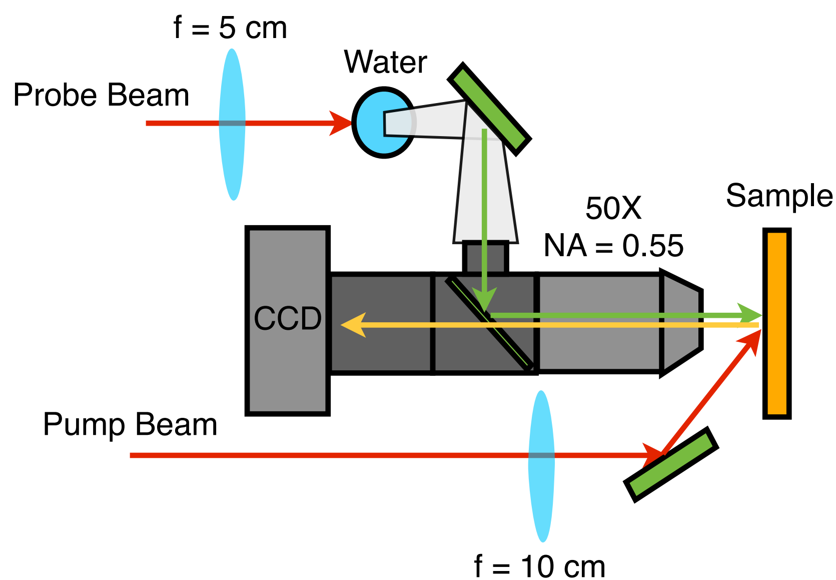

FIG 3.6.2. Pump-probe setup for imaging ripple formation at normal incidence. Illumination is provided by white light produced in water using the probe beam. The pump beam strikes the sample at a 45° angle with s-polarized light.

Fundamental probe light was converted into a semi-coherent white light spectrum by focusing the light into a beaker of DI water with an f = 5 cm lens; dispersion lengthened the probe pulse length to ~ 3 ps. The beam was then directed into an infinity correcting tube and sent backwards through a 50X objective (Working Distance =

13 mm). The objective projected white light onto the sample at normal incidence; the white light then reflected off the sample and travelled back through the objective into the CCD camera. Fresnel fringes were present at the rim of the projected white light circle and offered enhanced imaging resolution compared to regions where fringes were present. It is hypothesized that phase contrast was achieved in the Fresnel fringe regions. With this setup, the pump beam must strike the sample at an ~ 45° angle. The samples were irradiated with s-polarized pump light with this configuration by rotating the polarization 90° w.r.t the optics table.

Section 3.7 Material Growth

Many of the materials studied in this thesis were purchased or provided by other lab groups as noted. When thin film growth was required, sputter deposition and chemical vapor deposition (CVD) were employed, detailed in the following sections.

Section 3.7.1 Ni Thin Film Deposition

Ni thin films were grown using a DC Manetron sputtering system operated in continuous rotation mode using a 200 W sputter power, Ar gas pressure of 2.1 mTorr, and a typical base pressure of ~ 4 µTorr. The thickness of the Ni film was varied from 0.5 nm to 500 nm and controlled by varying the sputter time. The sputter rate (8 nm/minute) was calibrated with Rutherford Backscattering (RBS) using a 2 MeV helium ion beam line located at the University of Michigan, Michigan Ion Beam Laboratory (MIBL), operated by Ovidiu Toader and Fabian Naab. Silicon and glass samples with dimensions of 2 x 2 cm were clamped to the rotation stage with a non-galvanized bolt and washer. Semi-automation of the sputter tool was implemented by Payton Spaller using LabVIEW programming of the pressure valves which control the shutters for future deposition of multi-layer thin films using continuous rotation and two sputter targets.

Section 3.7.2 SiO_2 Thin Film Deposition

Deposition of SiO_2 thin films onto diced Si, Al, Ni, and microscope glass slide samples from the gas phase was performed using a GSI Plasma-Enhanced Chemical Vapor Deposition (PECVD) chamber at the University of Michigan Lurie Nanofabrication Facility (LNF) at a temperature of 200 °C. Deposition typically resulted in ~ 1 µm of SiO_2 and ~ 40 MPa compressive stress.

Si-SiO_2 samples were prepared by Kristen Tebo at the LNF facility using a Low-Pressure Chemical Vapor Deposition (LPCVD) furnace growth chamber. An SiO_2 thickness of ~ 1.2 µm with a ~ 100 MPa compressive stress was typically grown.

Section 3.8 Microscopy Long After Irradiation

After laser irradiation, sample characterization was performed in order to view and measure laser-induced morphology. The type of characterization utilized was dependent on both the type of information desired and the sample type. Characterization techniques utilizing light, electrons, and scanning probe microscopy (SPM) techniques are detailed in the following sections.

Section 3.8.1 Optical Microscopy

Optical images were acquired for measurement of damage morphology dimensions for all samples, with the exception of nanoparticle samples. Optical images were collected in the University of Michigan L. H. Van Vlack Undergraduate Laboratory using Nikon Optiphot microscopes and an Olympus BX-51 Fluorescence microscope in the LNF. Both microscopes had Differential Interference Contrast (DIC) capabilities when Nomarski prisms were inserted.

Section 3.8.2 Atomic Force Microscopy

The SPM technique, Atomic Force Microscopy (AFM) was performed on crater, blister and microtube, and ripple samples to determine the height of the damage

features after laser irradiation. All AFM images were collected using a Veeco Dimension Icon AFM at the University of Michigan Electron Microbeam Analysis Laboratory (EMAL) operated in tapping mode. The maximum height travel of the scanner was ~ 6 µm so it was not possible to measure samples with heights > 6 µm. A scan rate of 0.7 Hz was typically used to minimize streaking of the images and the time required for image collection.

Section 3.8.3 Scanning Electron Microscopy

Scanning Electron Microscopy (SEM) was performed on crater, ripple, polymer, and CNT samples to determine the sample surface morphology. Images were collected using an SEM located in the L. H. Van Vlack undergraduate laboratory (Phillips model XL30) and a Hitachi SU8000 SEM located in the LNF. Various techniques were used on the SEM including backscattered electron (BSEM) analysis and X-ray Energy Dispersive Spectroscopy (XEDS).

Section 3.8.4 Transmission Electron Microscopy

Transmission Electron Microscopy (TEM) was performed on NP and CNT samples to determine composition and crystalline structure and when other techniques were not able to measure sample morphology. All samples were prepared by depositing NPs or CNTs onto copper grids with a holey carbon coated film covering the grid. Bright field electron images and XEDS spectra were collected using a JEOL 3011 High Resolution Electron Microscope (HREM) located in EMAL. Scanning TEM (STEM) was performed using a JEOL 2100F Cs-Corrected Analytical Electron Microscope to obtain atomic resolution images of NPs and to perform Electron Energy Loss Spectroscopy (EELS) to determine chemical composition of the NPs.

References

D. P. Banks, C. Grivas, J. D. Mills, I. Zergioti, and R. W. Eason, *Nanodroplets deposited in microarrays by femtosecond Ti:sapphire laser-induced forward transfer*, Applied Physics Letters **89**, 193107 (2006).

S. Bera, A. J. Sabbah, J. M. Yarbrough, C. G. Allen, and B. Winters, *Optimization study of the femtosecond laser-induced forward-transfer process with thin aluminum films*, Applied Optics **46**, 4650 (2007).

J. Bonse, S. Baudach, J. Kruger, W. Kautek, and M. Lenzner, *Femtosecond laser ablation of silicon–modification thresholds and morphology*, Applied Physics A **74**, 19 (2002).

A. Borowiec, and H. K. Haugen, *Femtosecond laser micromachining of grooves in indium phosphide*, Applied Physics A **79**, 521 (2004).

M. C. Downer, R. L. Fork, and C. V. Shank, *Femtosecond imaging of melting and evaporation at a photoexcited silicon surface*, Journal of the Optical Society of America B **2**, 595 (1985).

J. P. McDonald, V. R. Mistry, K. E. Ray, S. M. Yalisove, J. A. Nees, and N. R. Moody, *Femtosecond-laser-induced delamination and blister formation in thermal oxide films on silicon (100)*, Applied Physics Letters **88**, 153121 (2006).

Chapter 4
Ultrafast Laser Interactions with Single Interfaces

To explore the role of a single interface on material removal after ultrafast irradiation, Ni thin films were deposited onto various substrates and Ni morphologies were studied after ultrafast irradiation. The morphology present within the following sections doesn't occur after ns laser irradiation and is unique to fs laser irradiation. A ns laser pulse is on much longer and the material removal mechanisms are very different than those after fs laser irradiation.

The fs laser interaction mechanisms presented in this chapter explain digital material removal after the irradiation of multi-layer reactive foils seen by other researchers [Picard 2005, Picard 2006]. The thin film removal mechanisms are also applied to NP production without the use of solvents. Several applications for NPs include light harvesting [Derkacs 2006], paint [Vorbau 2009], and catalysts (especially for CNT growth) [Kobayashi 2004]. Carbon nanotube growth using CVD involves depositing thin films of catalysts, such as Fe or Ni, onto an alumina layer on a Si substrate and heating the film until it dewets. Dewetting of the catalyst film breaks the film up into catalyst NPs. In addition to exploring the interaction of fs lasers with thin films and interfaces, it will be shown in this chapter that Ni NPs can be printed from thin films for CNT growth, opening the possibility of more control over CNT growth by controlling NP properties.

The basic ideas presented in this chapter will be continually revisited in the following chapters to explain morphology after the irradiation of metals, semiconductors, insulators, multilayers, and finally carbon based materials.

Section 4.1 Ultrafast Laser Interactions with a Ni-Silicon Interface

Bulk Ni samples were mechanically polished and irradiated with single laser pulses, and the damage radius of the Ni film is plotted against fluence in Figure 4.1.1.

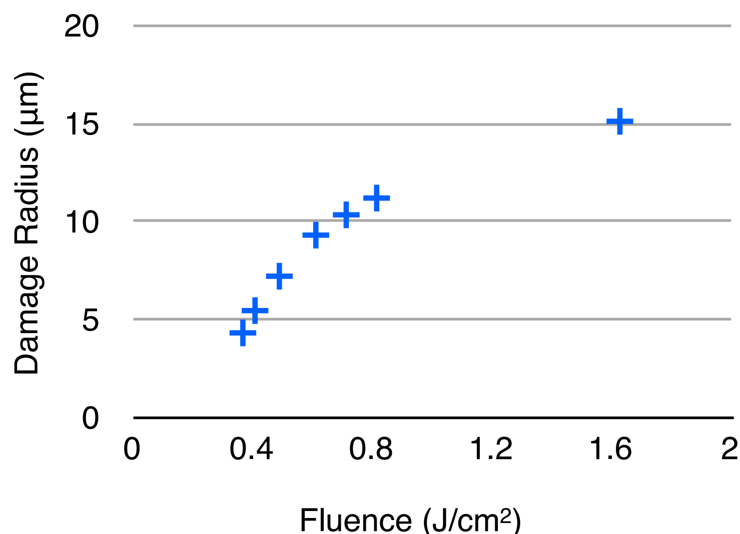

FIG. 4.1.1. Damage threshold study of a bulk Ni target. The damage threshold was found to be 0.32 J/cm^2. The standard deviation of each data point is ≤ 200 nm.

The damage threshold was found to be 0.32 J/cm^2. An SEM and AFM image of the crater in bulk Ni are shown in Figure 4.1.2 at a fluence of 0.71 J/cm^2. The AFM image and trace show a characteristic ~ 20 nm deep crater for metals and semiconductors in the bulk Ni surface.

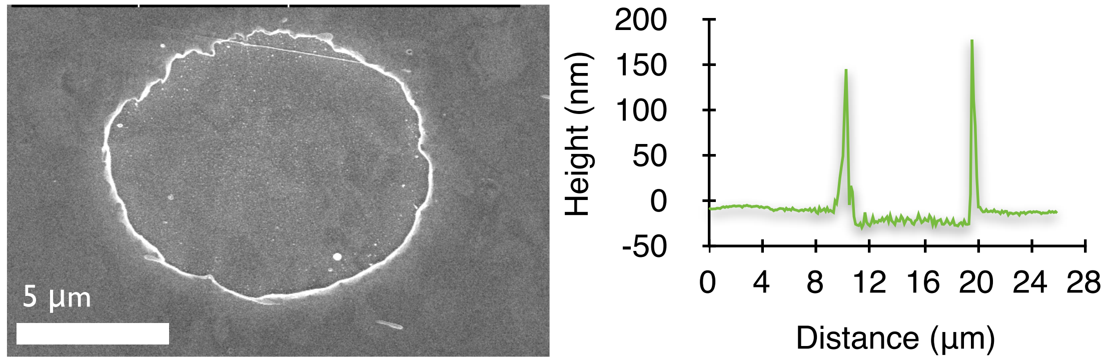

FIG. 4.1.2. (a) SEM image of a crater in bulk Ni after irradiation with a single pulse at 0.71 J/cm^2. (b) An AFM line trace from the crater in (a).

After irradiation of bulk Ni, MD simulations have shown that material removal is dominated by the homogeneous nucleation of voids from vacancies present in the melt at the trough of the tensile wave within the expanding molten Ni [Leveugle 2004]. After absorption of the laser energy by conduction electrons, the electrons are excited to high electronic states and equilibrate with the cold lattice a few picoseconds after absorption of the laser pulse, resulting in a solid to liquid phase transition and subsequent expansion. Before the expansion associated with the liquid transition is concluded, high temperature collisions within the hot liquid Ni set up extreme pressure gradients at the free surface-liquid-bulk interfaces. The pressure gradients drive expansion of the liquid from the free surface away from the sample, launching a shock wave and accompanying rarefaction wave into the liquid Ni. The local pressure within the liquid goes negative as the rarefaction wave forms and vacancies homogeneously coalesce into voids along a plane within the melt. A thinning of the cross-sectional area perforates this plane of voids and cohesion within the liquid allows for a transfer of stress from the expanding melt to the perforated plane. The majority of the bonds broken within the melt are in this plane, therefore the result is the ejection of a thin slab of melted material from the surface. In bulk, the minimum amount of material that is removed corresponds to the depth at which these voids can nucleate and grow. Near the removal threshold of bulk Ni this minimum depth is ~ 20 nm. This process is illustrated in Figure 4.1.3.

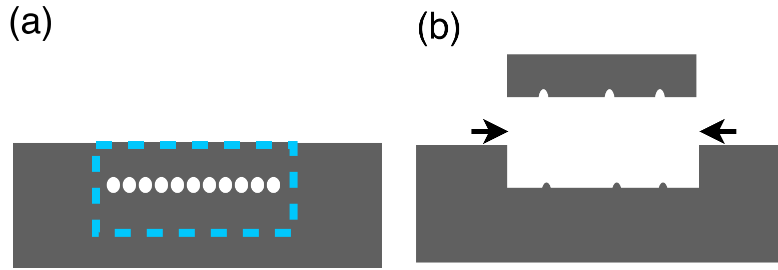

FIG. 4.1.3. (a) After irradiation, part of the Ni melts (dashed line) and homogeneous void nucleation occurs within the melt, perforating a plane in the film. (b) Cross-section illustration of material separation at the damage threshold. The material separates along the perforated plane in (a). Black arrows indicate the edge of the crater and the damage threshold of the film.

To investigate the role of an interface on material removal, a 70 nm Ni film was sputtered onto a Si substrate and irradiated with single laser pulses. The fluence required for damage of the 70 nm film was observed to decrease to 0.26 J/cm^2, below the threshold for bulk Ni. Fluences near the damage threshold of the 70 nm film produced craters in the film. When the laser fluence was increased to 0.95 J/cm^2, both a crater and pits were formed in the surface of the Ni film, shown in the SEM and AFM images Figure 4.1.4.

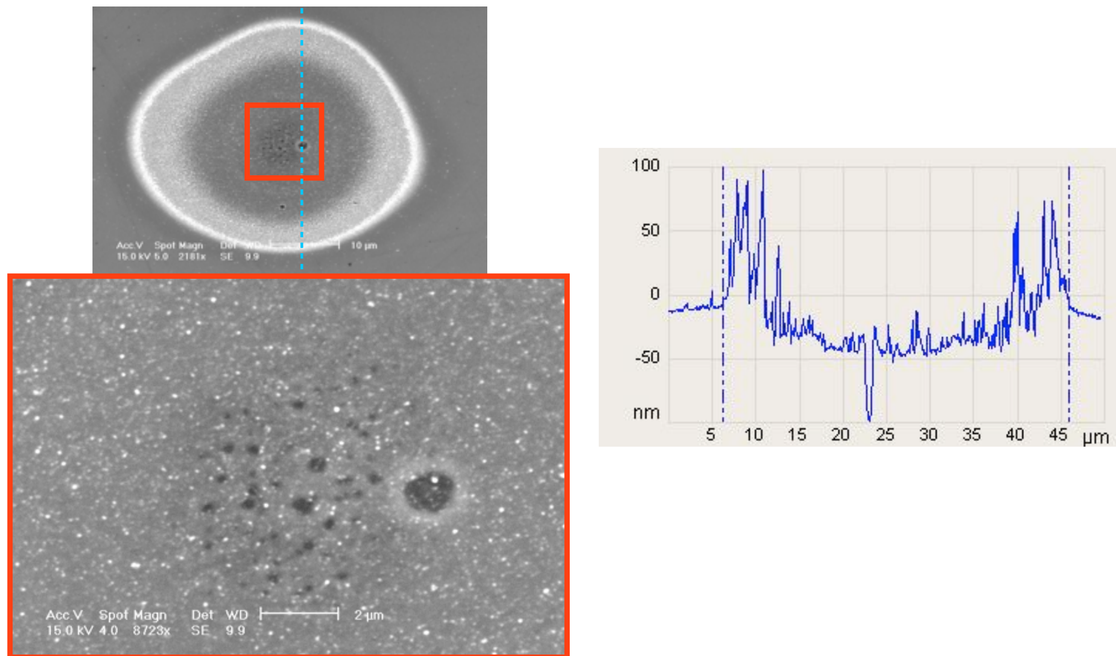

FIG. 4.1.4. Irradiation of the 70 nm Ni film at 0.95 J/cm^2. The blue dashed line in the SEM image indicates where the AFM line trace was taken. The pits in the SEM image are seen to extend down to the Ni-Si interface in the AFM image.

The AFM and SEM images show the pits are located in the center of the crater in the Ni film and the pits were typically < 2 µm in diameter. Height profiles from the AFM image indicate that the pits extend down to the Ni-Si interface. Pit formation at this interface after laser irradiation is evidence of material removal from the Ni-Si interface initiated by material breaking at this interface. It is shown that the simple presence of the interface changes the amount of material removed from the thin Ni film.

As discussed above, material removal near the removal threshold is dominated by void nucleation and growth within molten material. In bulk material this has been shown to be a homogeneous process within the melt. But pit formation provides evidence that defects at the Ni-Si can also provide nucleation sites for void formation and growth. The random nature of defects at the interface means that voids can heterogeneously nucleate at the interface, and this process ultimately leads to material removal from the interface. The material is still expanding when the melt front reaches the interface so the cross-sectional area between growing voids decreases and bonds at the interface are broken causing a release of the Ni film. Cohesion within the liquid transfers stress to planes containing voids within the film and at the interface. This

allows for interface separation in the center of the crater and intra-film separation in the outer crater of the film.

At low laser fluences, the melt front doesn't reach the interface and homogeneous void formation within the film results in crater formation only within the film, illustrated in Figure 4.1.5. At high fluences, the melt front reaches the interface and material is removed both from within the film and from the interface.

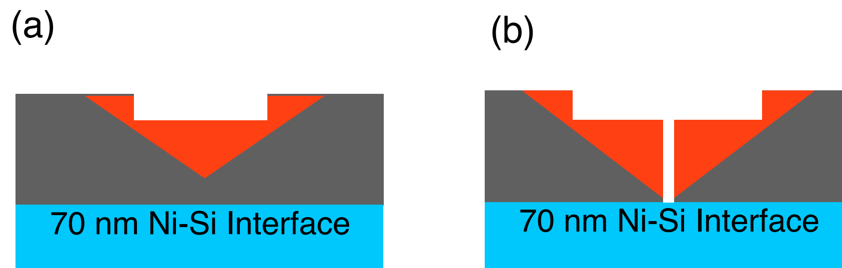

FIG. 4.1.5. (a) Illustration of material removal from within the a 70 nm Ni film on a Si substrate at low fluence. The melt front doesn't reach the Ni-Si interface and material is only removed from within the film. (b) At higher fluences, the melt front reaches the interface and material removal occurs both within the film and at the interface.

This phenomenon shows that the location of material removal can be controlled by the presence of an interface and explains what previous researchers have seen when removal of multi-layer reactive foil layers appeared to occur in a digital fashion, below the threshold fluence for ignition of the foil [Picard 2005]. Each interface provides a site for void nucleation and consequently material removal. Future studies will compare fluences used for irradiation to modeling heat transfer through the Ni film and correlating the fluences where pit formation is observed to the melt depth.

To explore the lower temperature requirements for void formation at interfaces, thinner Ni films were sputtered onto Si substrates. It was hypothesized that thinner films should further lower the temperature requirement and fluence requirement for removal of material from the film. Irradiation of a 10 nm Ni film sputtered onto a Si substrate is shown in the SEM images Figure 4.1.6.

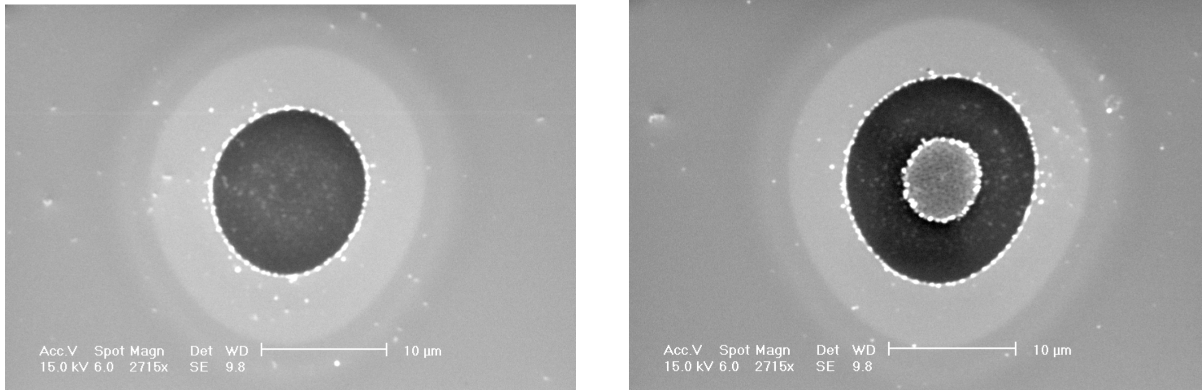

FIG. 4.1.6. SEM images of single shot irradiation of a 10 nm Ni film on a Si substrate. (a) Irradiation at 0.20 J/cm^2 removes a 10 nm disc of Ni from the substrate. (b) Irradiation at 0.30 J/cm2 removes a washer shape of Ni from the substrate and leaves a pedestal of Ni in the center of the irradiated region.

At low fluences in Figure 4.1.6(a), the 10 nm Ni film was completely removed from the substrate in the center of the irradiated region, less than the minimum 20 nm value for bulk Ni. The threshold fluence for material removal was calculated to be 0.18 J/cm^2, lower than the damage threshold of the 70 nm film.

If the the fluence is increased to 0.30 J/cm^2, it is seen in Figure 4.1.6(b) that the diameter of material removal has increased, but a “washer” shape of Ni is removed and a pedestal close to the same height as the original Ni surface has appeared in the center of the damage region. If the fluence is increased further, the pedestal is removed from the center and a ring at the same height as the original Ni surface appears. As the fluence is increased, the ring gets larger, and the local laser fluence at the edges of the ring remains the same. This indicates a deterministic threshold fluence for ring formation.

It is hypothesized here that Ni silicide formation with a bandgap greater than the fs laser’s single photon energy (1.59 eV) occurred during sputtering by Ni diffusion into the Si substrate at the elevated sputtering temperatures. Single photon absorption in Ni wouldn’t occur at low intensities for a bandgap greater than the single photon energy but two photon absorption above a threshold intensity may promote electrons into the conduction band, removing energy from the Gaussian pulse in regions of the highest intensity.

For low fluence, the intensity isn’t high enough to promote electrons across the Ni silicide bandgap, and is absorbed by the Si underneath. Bonds are broken at the

interface and a disc of material is ejected from the substrate. When the fluence increases above the threshold intensity, energy from the laser pulse is lost to promoting electrons across the Ni silicide bandgap and enough energy isn't left over to remove the film. Significantly above this threshold the Ni silicide layer may begin melting and removes the pedestal from the middle of the irradiated region. The origin of the annular ring contrast in the SEM image which surround the material removal region is unknown and may be due to laser induced changes to the underlying Si substrate.

Future studies should focus on using cross-sectional TEM analysis to study possible Ni silicide formation, its thickness, and the damage morphology dependence on silicide structure and thickness after irradiation.

Section 4.2 Ultrafast Laser Interactions with a Ni-Glass Interface

To minimize possible Ni silicide formation, varying thicknesses of Ni layers were sputtered onto microscope cover slips. By studying Ni film removal from glass substrates, direct effects of the transition from homogeneous nucleation of voids within bulk material to heterogenous nucleation of voids at the interface were observed. These effects make it possible to tailor the surface morphology of the irradiated surface by inducing void nucleation either within the film or at the interface.

The Ni films were irradiated at normal incidence and, as with previous Ni studies, irradiation of the Ni thin films also produced increasing crater diameters with increasing fluence. Irradiation of $\geq$ 20 nm thick Ni films on glass substrates with single shots slightly above the material removal threshold resulted in removal of material *within* the film (intra-film separation), shown in the AFM image and trace in Figure 4.2.1(a) after irradiation of a 20 nm film at 0.20 J/cm^2. For 20 nm Ni films, an increase in fluence to 0.40 J/cm^2 forms an outer ring of intra-film separation, Figure 4.2.1(b), and a deeper crater is also seen within the center of the irradiated region. Material removal occurred at the interface (interface separation) in the central crater. The rim of each crater is seen as spikes in the AFM traces extending ~ 30 nm above the Ni surface. The ~ 2 µm diameter pits surrounding the central crater extend down to the Ni-cover slip interface. Pedestal formation is no longer seen, as was seen at the Ni-Si interface.

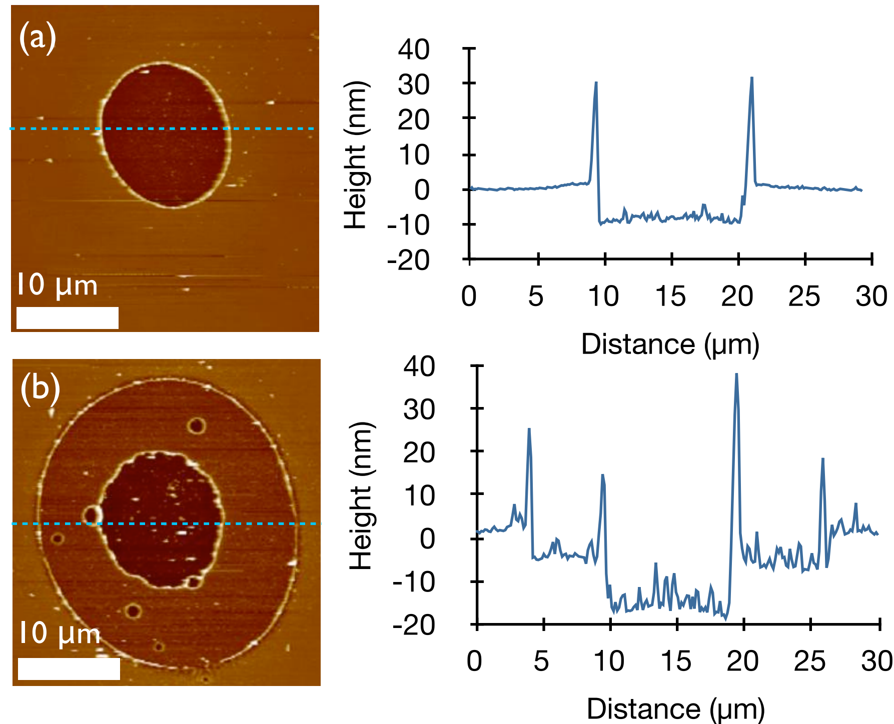

FIG. 4.2.1. Irradiation of a 20 nm thick film of Ni on a glass microscope cover slip. a) Irradiation at a peak fluence of 0.20 J/cm^2 results in intra-film separation. b) Irradiation at a peak fluence of 0.40 J/cm^2 results in both intra-film separation and interface separation, producing a much larger outer crater and a smaller inner crater. Models for the two different material removal mechanisms are in the text.

Variations in the surface roughness seen in the AFM traces in Figure. 4.2.1 were quantified by measuring the root mean square (RMS) value of the surface roughness with AFM. The RMS roughness from 5 separate craters for both intra-film (0.20 J/cm2) and interface separation (0.40 J/cm2) was measured with AFM and averaged. The RMS roughness after intra-film separation was 1.58 nm (standard deviation = 0.24 nm) and the RMS roughness after interface separation was 3.01 nm (standard deviation = 0.25 nm). AFM images in Figure 4.2.2 show representative comparisons of the surface roughness after intra-film separation, Figure 4.2.2(a), and after interface separation, Figure 4.2.2(b). Interface separation, Figures 4.2.1(b) and 4.2.2(b), resulted in an average > 90% increase in surface roughness compared to intra-film separation, Figures 4.2.1(a) and 4.2.2(a). The original Ni and glass RMS surface roughnesses were less than 0.60 nm.

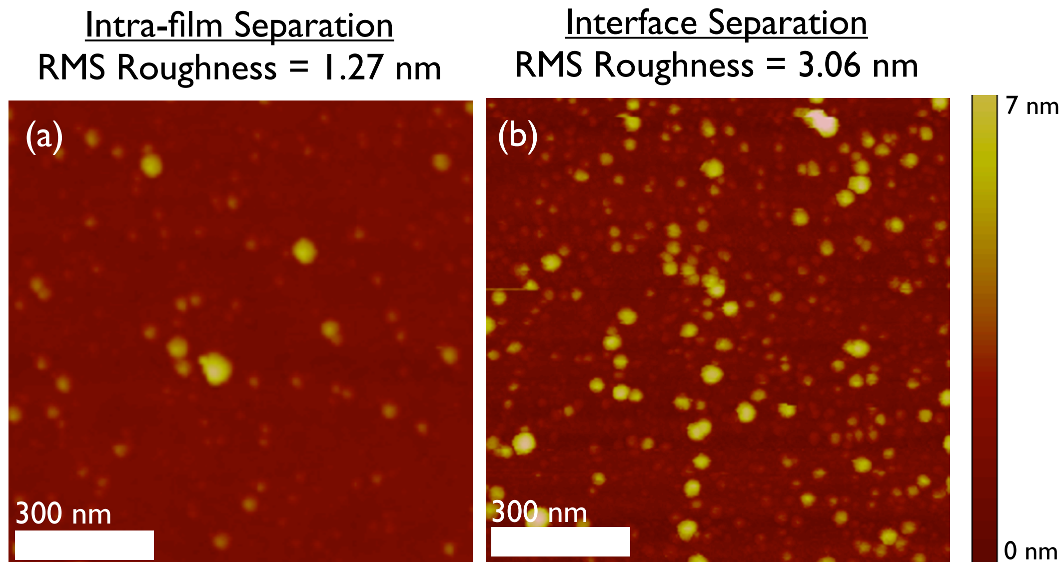

FIG. 4.2.2. Representative AFM images of the surface roughness after laser irradiation of a 20 nm thick Ni film. a) AFM image of the surface after intra-film separation. Irradiation at 0.20 J/cm^2. The RMS roughness is 1.27 nm. (b) AFM image of the surface of the central crater after interface separation. Irradiation at 0.40 J/cm^2. The RMS roughness is 3.06 nm. The surface is much rougher after interface separation compared to intra-film separation.

To investigate the dependence of the material removal threshold from the thin film on film thickness, threshold studies were performed for each film thickness. The damage radius for intra-film separation for different film thickness is shown in Figure 4.2.3.

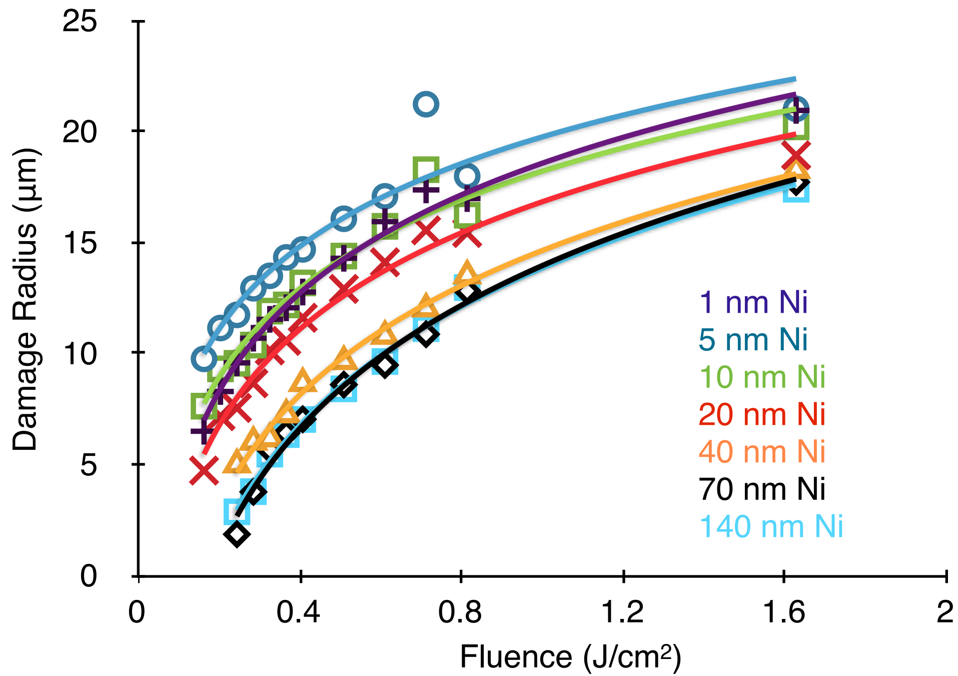

FIG 4.2.3. Damage Radius vs. Fluence for varying thin film thicknesses of Ni deposited onto microscope cover slips. All damage measurements had a standard deviation ≤ 2 µm.

The damage radius increases with increasing fluence for thin films and the material removal threshold for each film was calculated using a two-parameter fit and plotted in Figure 4.2.4.

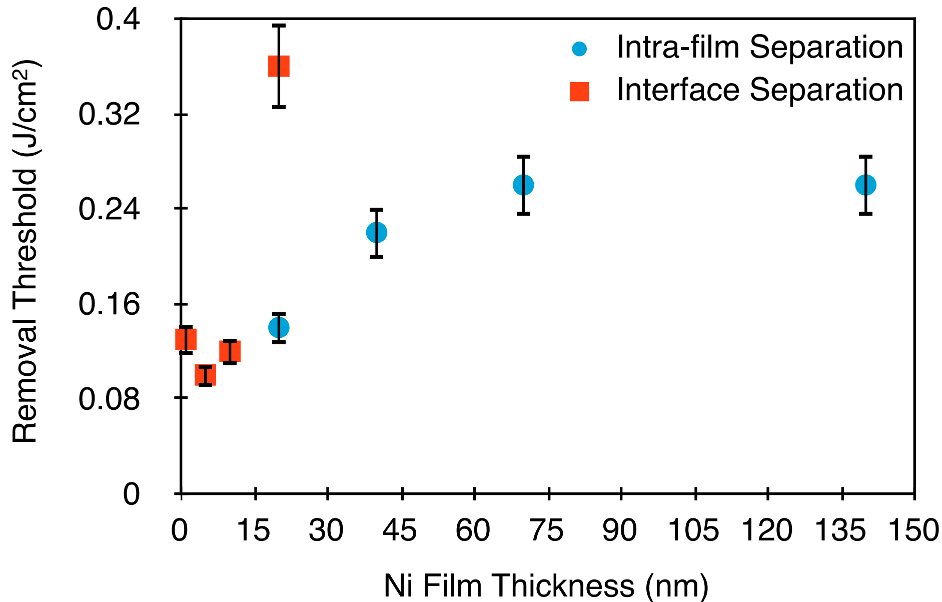

FIG. 4.2.4. Material removal threshold vs. Ni film thickness for thin Ni films on microscope cover slips. The removal threshold increases with film thickness for films 5 nm thick and greater. Two removal thresholds for 20 nm thick films corresponding to intra-film separation and interface separation are plotted. Calculated removal threshold values from different samples with the same Ni thickness agreed to within 10%. Intra-film separation is not possible for films ≤ 10 nm thick and interface separation for films 40 nm thick occurs at 1.2 J/cm^2 (not shown on the plot).

Material removal transitioned from intra-film separation to interface separation for decreasing film thickness. Two different damage thresholds are shown for 20 nm thick Ni films indicating different thresholds for intra-film separation and interface separation. The blue circles indicate removal of material from within the Ni film and the red squares indicate removal at the interface. The threshold for interface separation for 40 nm thick films occurs at 1.2 J/cm^2, not shown on the plot. Interface separation was only investigated for Ni film thicknesses of 1, 5, 10, 20 and 40 nm. In order for removal to occur at the interface for the 20 nm and thicker films, heat transfer must travel all the way down to the interface, leading to higher removal thresholds and larger variations in the data. This relation will be studied in more detail in future studies by studying pit formation with pump-probe and by modeling heat transfer in thin films.

By quantifying the surface roughness after intra-film and interface separation, we can correlate surface roughness to two separate material removal mechanisms, homogeneous and heterogeneous void nucleation. From Figure 4.2.2, surfaces after interface separation are 90% rougher than surfaces after intra-film separation. Since

the original Ni and glass surfaces were much smoother than the resulting roughness, the larger surface roughness in Figure 4.2.2(b) is the result of heterogeneous void nucleation at the Ni-cover slip interface. Defects at the interface provide nucleation sites for heterogeneous void formation and growth. The material is still expanding when the melt front reaches the interface so the cross-sectional area between growing voids decreases and bonds at the interface are broken causing a release of the Ni film. Cohesion within the liquid can transfer stress to planes containing voids within the film and at the interface. This allows for interface separation in the central crater and intra-film separation in the outer crater in the 20 nm film. Since interface separation is a heterogeneous process, areas where voids don't form will still contain Ni that wasn't removed from the Ni-cover slip interface, forming rougher surfaces, seen in Figure 4.2.2(b).

Slightly above the damage threshold of Ni films, part of the film melts, and homogeneous void nucleation and growth occurs within the film, Figure 4.2.1(a). Thin slab ejection results in intra-film separation for film thicknesses ≥ 20 nm, illustrated in Figure 4.2.5(b), producing the crater in Figure 4.2.5(c). The smooth surfaces quantified in Figure 4.2.2(a) are illustrated in Figure 4.2.5(b). As the fluence is increased, a larger area of the Gaussian beam is raised above damage threshold of the Ni, marked with arrows in Figure 4.2.5, and larger slabs of material are removed. The elevated rims around the crater from the AFM trace in Figure 4.2.1(a) are not illustrated and form from Ni which was softened due to laser irradiation and pulled out of the plane by cohesion with the expanding dome of molten material during material removal. A decrease in surface tension of the molten Ni with increasing temperature causes the dome to break due to forward momentum transfer. After the material breaks, the Ni surface thermally quenches before the softened Ni pulled out of the plane can relax to the original surface height, forming elevated rims around the crater edge.

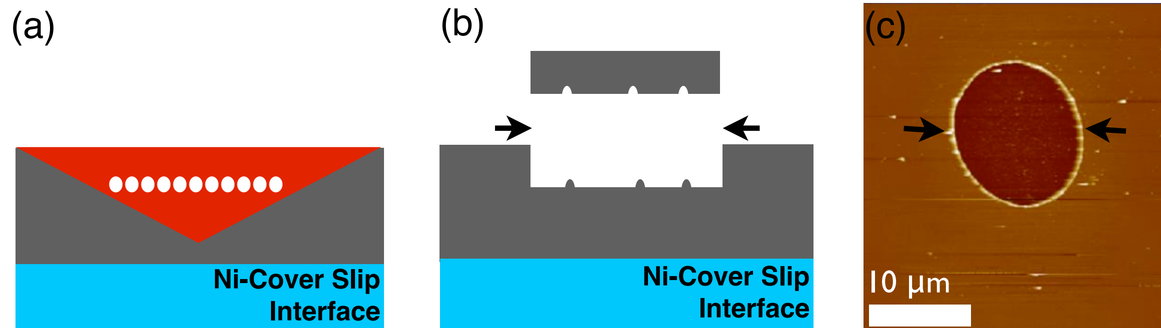

FIG. 4.2.5. (a) Part of the Ni film melts and homogeneous void nucleation occurs *within* the film, perforating a plane in the film. (b) Cross-section illustration of intra-film separation from ≥ 20 nm thick Ni films at the damage threshold. The material separates along the perforated plane in (a). Black arrows indicate the edge of the crater and the damage threshold of the film. Homogeneous nucleation within Ni films leads to intra-film separation and low surface roughness. (c) AFM image of intra-film separation from a 20 nm Ni film slightly above the film's damage threshold.

Figure 4.2.6(b) illustrates molten Ni removal from various regions of the 20 nm film in Figure 4.2.1(a) and the representative surface roughness on each surface. It is shown that the location of Ni removal controls both the amount of Ni removed and the resulting surface roughness after removal. The outer crater bounds regions where intra-film separation dominates and is marked with arrows. Homogeneous void nucleation within the molten Ni film ejects Ni slabs from within the film; the uniform process produces the smoother crater surfaces in Figure 4.2.1(a). The dashed lines bound areas where heterogeneous nucleation dominates the Ni removal process. Heterogeneous void nucleation and growth at the interface occurred in all areas bounded by the dashed lines and led to the ejection of Ni from the interface. Inhomogeneities in the fluence in Figure 4.2.6(a) produce local hot spots around the central crater. The melt front reached the interface in these regions and material removal formed pits which decorate the outer crater. Surface tension of the molten Ni will play a major role in the final morphology of the surface.

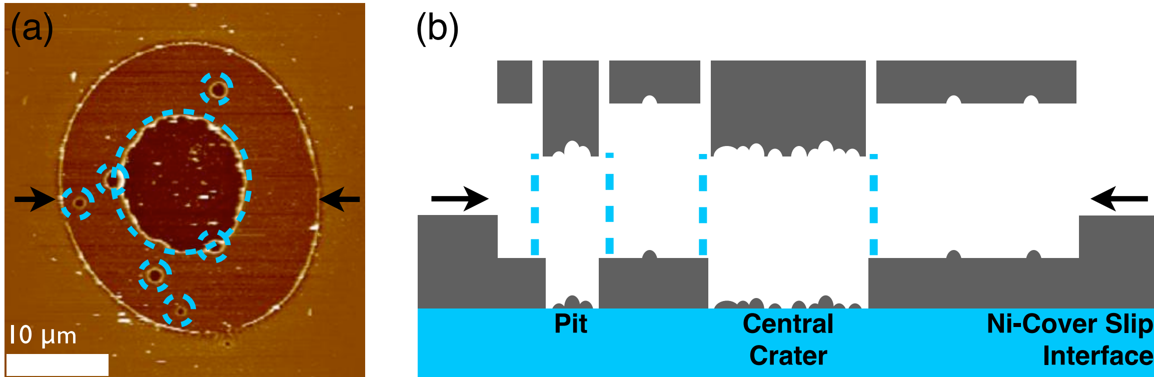

FIG. 4.2.6. Ni removal from a 20 nm Ni film. a) Arrows indicate the edge of the outer crater bounding intra-film separation areas. Areas where interface separation has occurred are bounded with dashed lines. b) Cross-section illustration of Ni removed from (a) and the resulting craters (not to scale). Heterogeneous void nucleation at the Ni-cover slip interface occurs in the central crater and pits, leading to interface separation and rougher surfaces. Homogeneous nucleation occurs *within* the Ni film and leads to intra-film separation and a lower surface roughness in all other areas bounded by the edge of the outer crater.

When the melt front doesn't reach the interface for films ≥ 20 nm thick, the material removal threshold decreases with decreasing film thickness. As the film thickness decreases, the material removal threshold begins to significantly drop around a film thickness of 60 nm. From around 60 nm down to a 20 nm thickness the confinement of ballistic electrons decreases the *melt* threshold of the Ni film by ~ 50% [Güdde 1998, Wellershof 1999]. In our study, the damage threshold was observed to continue to decreasing for film thicknesses < 20 nm. The absorptance of thin films is also dependent on film thickness and will contribute to the decreasing damage threshold. The reflectance (R) and transmittance (T) formulas for thin metallic films on transparent backings from [Harris 1951] were used to calculate the absorptance (A = 1-R-T) of 780 nm light by Ni deposited onto 115 µm of glass. The absorptance for film thickness is shown in Figure 4.2.7 and plotted against the damage threshold for thin Ni films.

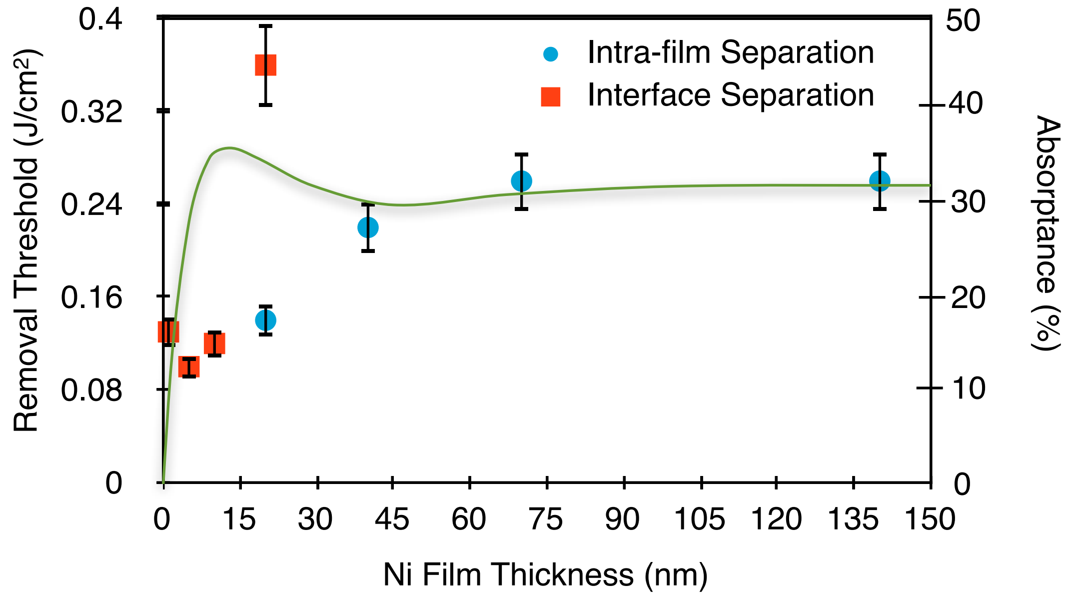

FIG. 4.2.7. Absorptance dependence of 780 nm light on Ni film thickness is plotted in green. The absorptance is plotted with the removal threshold dependence on film thickness.

The absorptance for thicker films approaches a value of 0.32 as expected for the absorptance of bulk Ni [Dennis 1972]. The absorptance begins increasing around 40 nm and peaks at 13 nm. For thicknesses < 13 nm the absorptance rapidly decreases. This increase in absorptance should correspond to a decrease in the melt threshold and consequently a decrease in the removal threshold of the film. To better understand the role the absorptance plays in changing the damage threshold with thickness, the predicted threshold based on absorptance change is plotted in Figure 4.2.8 by changing the Ni threshold by a percentage of the absorptance increase or decrease from the bulk absorptance.

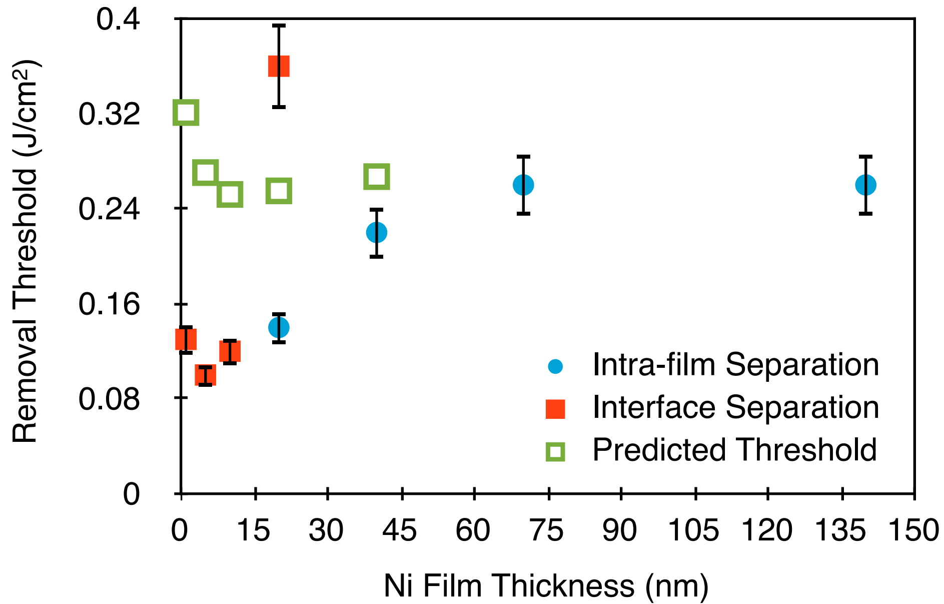

FIG. 4.2.8. Predicted removal threshold based on percent changes in absorptance with film thickness.

It can be seen that using only the Fresnel coefficients for R and T, the removal threshold change does not agree well with changes in the absorptance. A preliminary self-consistent calculation of the absorption coefficient performed by Ben Torralva has shown better agreement with the curve in Figure 4.2.7 by shifting the absorption peak to ~ 7 nm and doubling the absorption coefficient.

However, the rapid decrease in absorptance for Ni films < 5 nm thick doesn't correspond to a rapid increase in the removal threshold fluence of these films. There are several reasons for this. One reason is that the entire film is now melting after a single laser pulse, so the melt front doesn't need to propagate to an interface for void nucleation and growth. For films ≤ 10 nm thick, only interface separation was observed, shown in Figure 4.2.9.

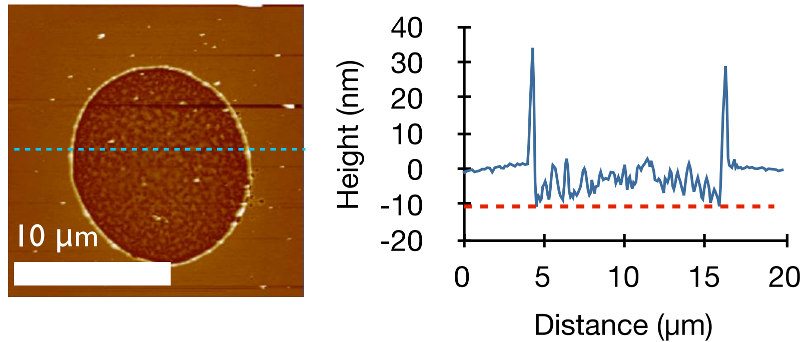

FIG. 4.2.9. Irradiation of a 10 nm thick film of Ni on a glass microscope cover slip. The red line indicates the location of the Ni-cover slip interface. The peak fluence was 0.16 J/cm^2. For film thicknesses ≤ 10 nm, material removal only occurred at the Ni-cover slip interface and the roughness within the crater is on the order of the film thickness.

It is hypothesized for films ≤ 10 nm thick, heterogeneous void dominates the material removal process and voids may not form within the film. The entire film is now melting and heterogeneous nucleation sites at the interface then allow for void nucleation and growth at temperatures lower than those required for growth within the film. The lower temperatures correspond to a lower rarefaction wave amplitude and a lower removal threshold. Films ≤ 5 nm thick may not provide enough melt in which the complete rarefaction wave may propagate and form its full “shape” as in bulk irradiation. Retarding the development of the rarefaction wave to an incipient state through confinement of the melt may increase the required laser energy for void formation and film removal, hence slightly increasing the removal threshold. Future studies should focus on experiments and simulations which elucidate the role the development of the tensile wave plays in material removal from thin films and their interfaces.

Material is not cleanly removed from the interface because the efficiency of material removal is now lower, producing rougher surfaces. Additionally, the surface in Figure 4.2.9 is slightly elevated in the center of the crater. This is counterintuitive since the center of the crater is the region of highest fluence, where one would expect the most material to be removed from, not the least. It was found in [Kaganovskii 2006, Trice 2007] that the morphology of thin films may be changed during ns irradiation as the film melts, dewets, and rapidly quenches with a surface roughness on the nano-scale. Therefore, the surface roughness after irradiation is likely a combination of two different factors. First the heterogenous nucleation of voids at the interface is a more

random process than homogeneous nucleation, increasing the surface roughness. Second, molten Ni may dewet towards the hottest part of the beam, the center of the irradiated region, and thermally quench with a larger amount of Ni in the center of the crater compared to the edges.

The thresholds for material removal of Ni thin films were also compared to irradiating the glass side of the Ni-glass interface first. It was found that when the glass side was irradiated first, the threshold for material removal was lower than if the Ni film was irradiated first, shown in Table 4.2.1. The absorptance of light was calculated for irradiating the Ni or glass side first and it was found that the absorptance was significantly higher if the glass side was irradiated first, Figure 4.2.10.

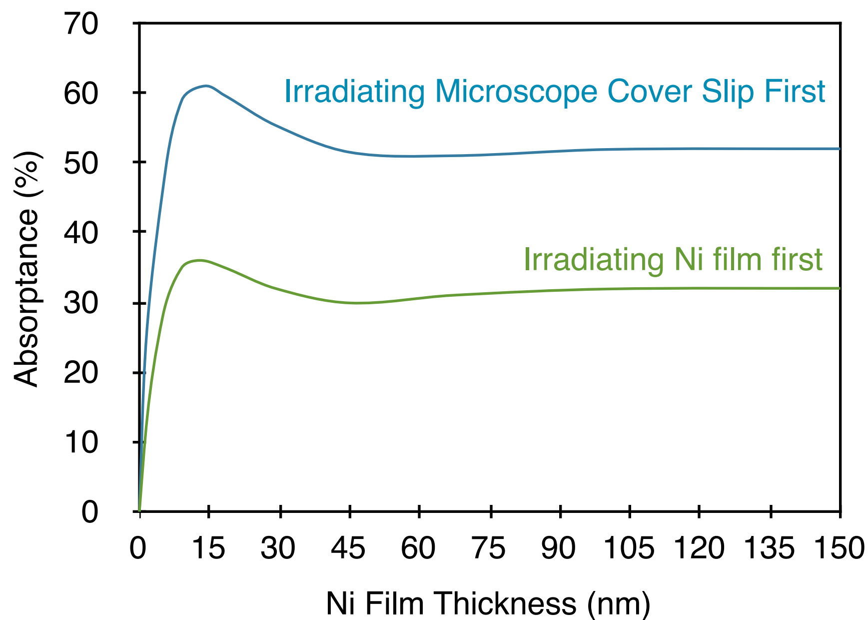

FIG. 4.2.10. Comparing film absorptance when laser light irradiates the Ni film first to irradiating the microscope cover slip first.

Changes in the absorptance when irradiating the glass or Ni film side first agreed well with changes in the interface separation thresholds for 5 and 10 nm thick Ni films and the intra-film separation thresholds for the 20 nm thick Ni films, showing direct affects of changes in absorptance to changes in the material removal threshold. The percent changes are shown in Table 4.2.1.

Film Thickness	**5 nm Ni**	**10 nm Ni**	**20 nm Ni**
Measured % change in removal threshold	33%	46%	33%
Calculated % change in removal threshold from absorptance changes	39%	41%	43%

Table 4.2.1. Comparing front and back removal thresholds for different Ni film thicknesses.

Section 4.3 Ultrafast Laser Printing of Nanoparticles

From the results in Section 4.2, it was hypothesized that intra-film and interface separation from thin films may allow for the study of NP formation. Initially, Ni films were irradiated in water to create a suspension of NPs for collection and drying onto TEM grids (as is common [Tripp 2002]), but it was difficult to reliably find focus of the sample underwater. In order to produce NPs more efficiently, a variation of the Laser Induced Forward Transfer (LIFT) technique was developed to print NPs in both air and vacuum. In this method, the film is irradiated from the glass side first, the film melts, and forward momentum from thermal expansion of the film in the plasma or molten state propels the film towards a substrate. A TEM grid was used for collection of the NPs for further investigation of NP size, structure, and morphology; although in principal the NPs may be printed onto any substrate.

A bright field TEM image of NPs printed from a 20 nm Ni film onto a holey carbon TEM grid positioned ~ 8 mm away from the Ni film using a fluence of 10 J/cm^2 and horizontal irradiation is shown in Figure 4.3.1. The film and TEM grid were rastered in front of the focused laser beam so that each laser shot irradiated a virgin area of the Ni film and the entire TEM grid was printed with NPs. Decreasing the distance between the Ni film and TEM grid had no effect on NP printing, and lowering the fluence resulted in no NP formation.

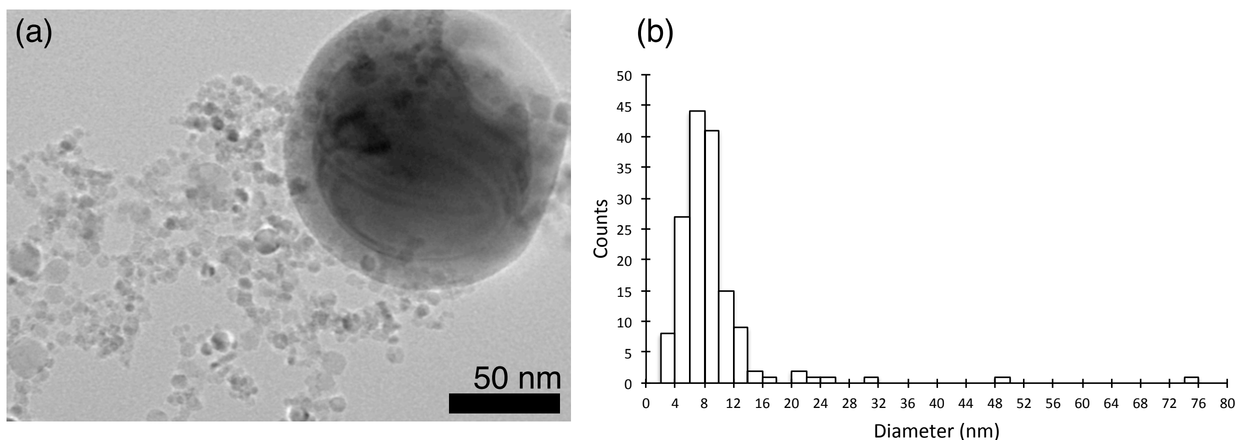

FIG. 4.3.1. Printing of Ni NPs from a 20 nm Ni film at a fluence of 10 J/cm^2.

The larger NPs (> 10 nm) are spherical and contrast in the TEM image suggests that an oxide shell is surrounding a Ni core. The oxide shell likely formed from partial oxidation of the condensed the Ni which forms the NP core. The smaller Ni NPs (< 10 nm) were usually faceted and two different shapes (squares and hexagons) were seen. Atomic resolution images of the smaller, faceted NPs are shown in Figure 4.3.2.

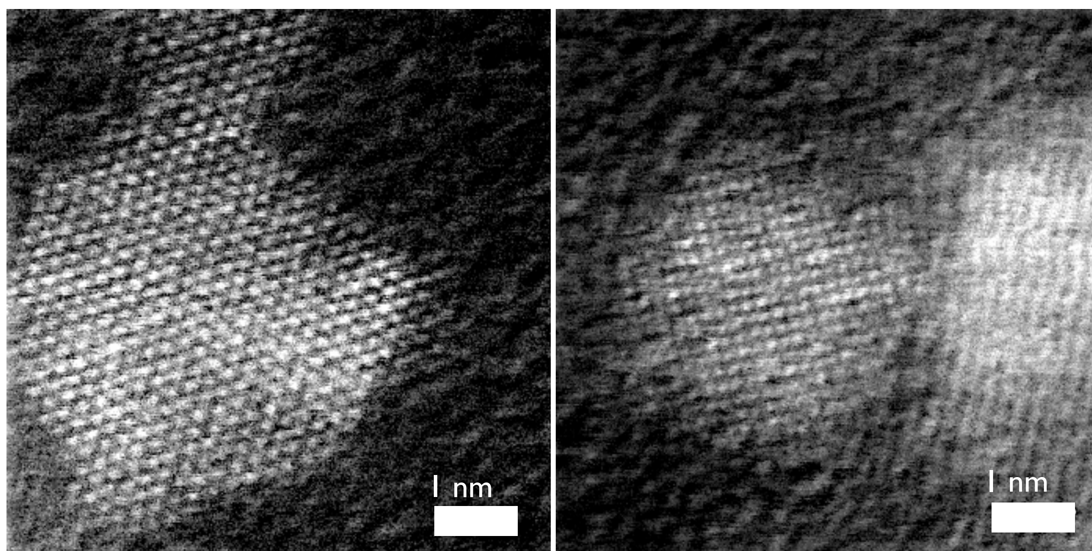

FIG. 4.3.2. Printing of Ni NPs from a 20 nm Ni film at a fluence of 10 J/cm^2.

Nickel oxide hexagonal plates have been produced in the literature using solution processing methods [Fiévet 1979], but their diameters are on the order of microns.

Nano-beam diffraction of the small faceted NPs created with this technique has shown that the cubes and hexagons may both be indexed to cubic NiO. Cubic shapes in the STEM images are the result of looking down the [100] zone axis of cubic NiO and hexagonal shapes are the result of looking down the [110] zone axis. Nano-beam EELS analysis of a hexagonal NP in Figure 4.3.2 has shown that the NPs contain equal amounts of Ni and O, confirming their composition is NiO. The EELS spectrum for a NiO NP is shown in Figure 4.3.3. A NiO NP EELS standard was used to calibrate the background subtraction. The leading edge of the O peak is located at 532 eV and the leading edge of the Ni peak is located at 855 eV.

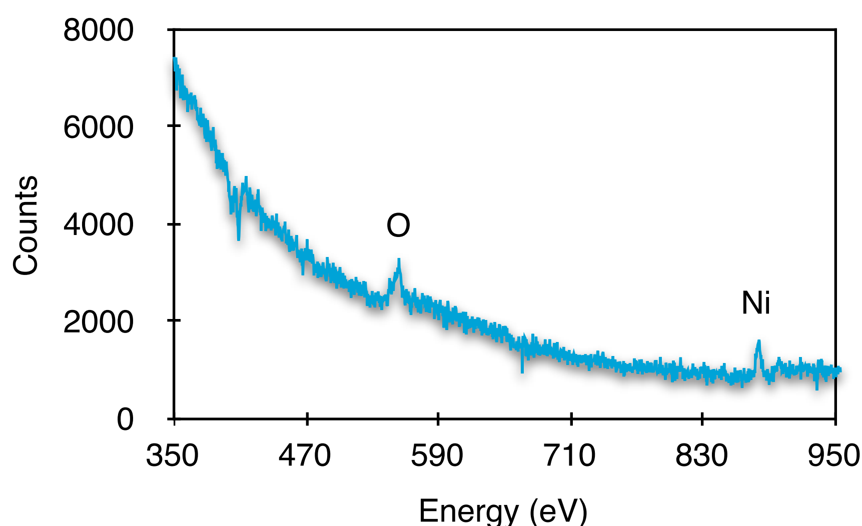

FIG. 4.3.3. EELS spectrum for a hexagonal NP. After background subtraction, the area under the Ni-L and O-K peaks are equal, indicating the NPs are NiO.

At 10 J/cm^2, interface separation occurs and a plasma is formed [Amoruso 2007]. Expansion of the plasma away from the Ni film occurs and NPs condense in flight as the plasma cools. Larger NPs are likely a result of molten Ni which has undergone more collisions before hitting the TEM grid than the smaller NPs. This suggests that NP size or shape may be controlled by using different atmospheres, such as air, gas atmosphere, or vacuum by controlling the collision rate.

To explore this possibility, NPs were also printed in a vacuum of 40 mTorr. The bright field TEM image in Figure 4.3.4 shows that the NPs exhibit many more facets than the simple cubes and hexagons seen in Figure 4.3.2.

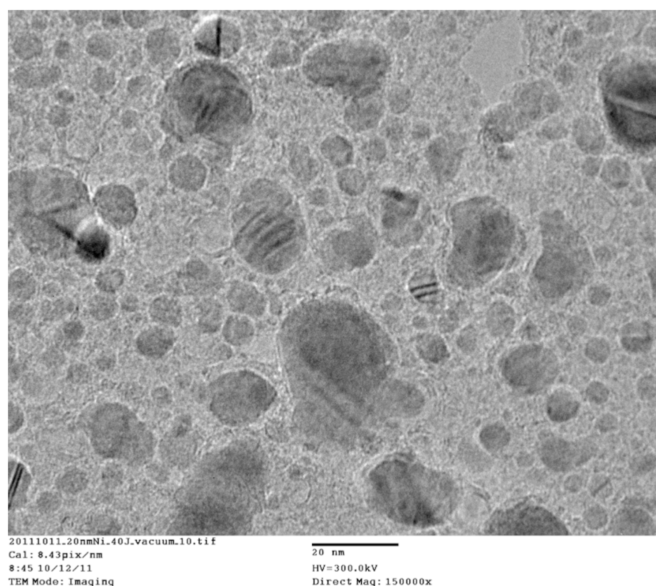

FIG. 4.3.4. NPs printed onto a TEM grid in a vacuum of 40 mTorr.

The NPs printed in vacuum have more facets than those printed in air likely because heat transfer is faster in vacuum. If the NPs created in vacuum are not completely cooled when they reach the substrate, they will thermally quench after striking the TEM grid. Nanoparticles created in air likely cool in transit to the TEM grid via heat conduction in the air. This slower cooling rate allows the NPs created in air to form equilibrium shapes, rather than quenching in the randomly shaped facets seen in the NPs created in vacuum. Future studies will focus on further control of the atmosphere the NPs are created in with different background gases and pressures for control of NP size and faceting.

Using the techniques discussed above, it was shown that faceted Ni NPs could be printed from a 20 nm Ni film onto an alumina substrate and used as catalysts during CNT growth with CVD. The resulting CNTs after CVD growth from the printed NPs are shown in Figure 4.3.5.

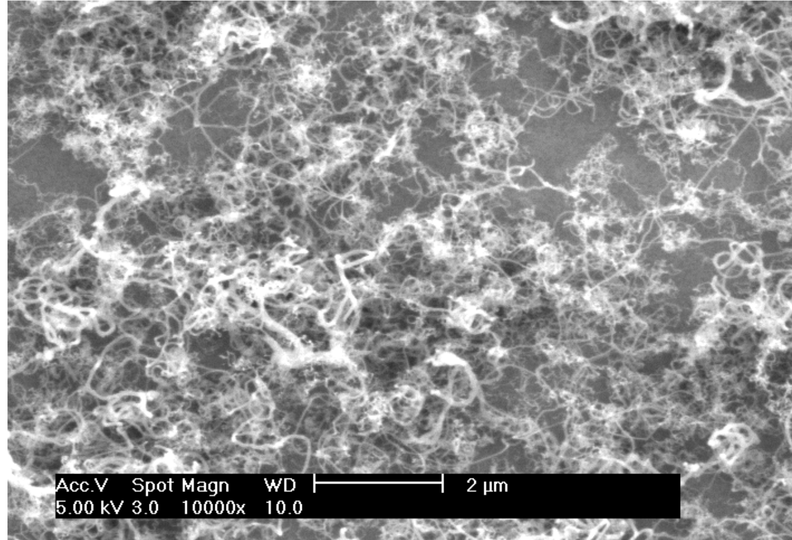

FIG. 4.3.5. SWNTs grown using CVD from catalyst NPs which were printed from a 20 nm Ni film.

The presence of the radial breathing mode peak in the Raman spectrum of these structures reveals they are single-wall CNTs. Future studies will focus on controlling the NP size and faceting, which may control CNT diameter, wall number, and CNT chirality.

Size control of NPs may also be possible by printing NPs from films which are thinner than the characteristic removal depth from bulk Ni, forming narrower NP distributions than those seen after bulk Ni irradiation. The collection efficiency for collecting NPs with the horizontal printing configuration was too low to print NPs from thin Ni films with thicknesses < 20 nm. A top-down irradiation approach using irradiation of 10 nm Ni film has shown promise of a better NP collection efficiency and will be used in future studies to attempt to control NP size by irradiating thinner Ni films.

Gold films with different film thicknesses had higher collection efficiencies with the horizontal printing setup using a 500 µm distance between the film and TEM grid and irradiation at a fluence of 0.08 J/cm^2. The results of Au NP printing after irradiation of a 3 nm Au film and a 10 nm Au film are shown in Figure 4.3.6.

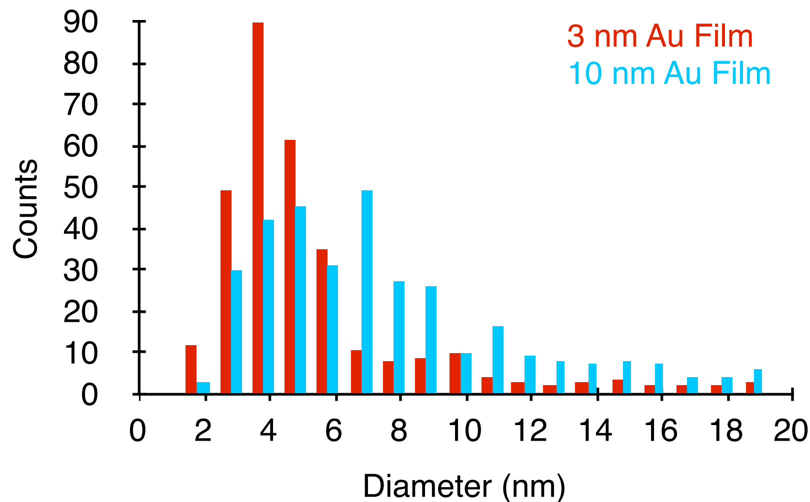

FIG. 4.3.6. Au NP distributions from laser irradiation of 3 nm and 10 nm Au films.

Gold does not form a continuous network after sputter deposition onto glass but NP formation is strong evidence that the film still became molten after irradiation, which then breaks up and forms NPs. Only spherical NPs were seen after irradiation of the Au films. The narrowing of the NP size distribution with the 3 nm film and shift towards smaller NP size suggests that the size of the NPs is most likely set by the thickness of the original film. The thickness of the 3 nm Au film confined the size of the Au NP distribution, compared to the 10 nm Au film.

Irradiation of the 10 nm Au films also produced large slabs of Au, shown in the bright field TEM image in Figure 4.3.7.

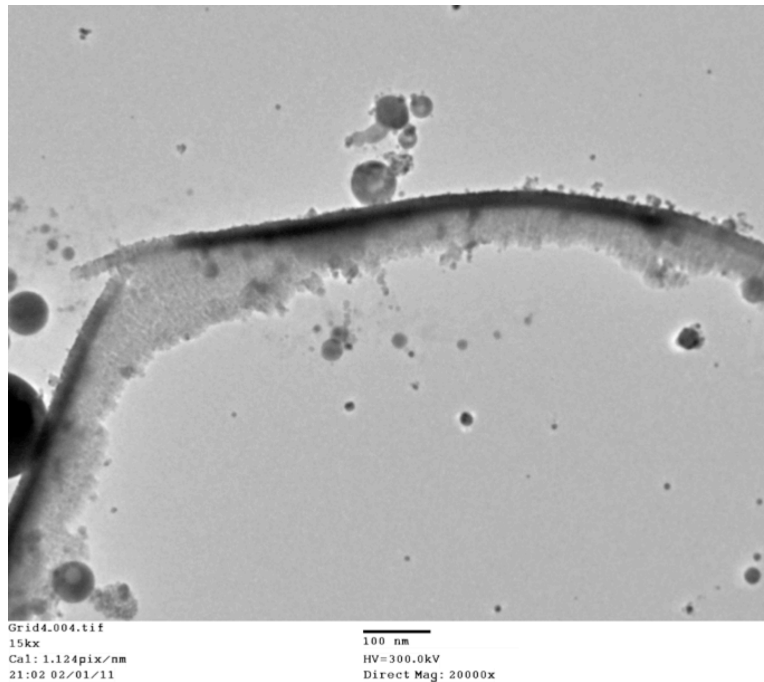

FIG. 4.3.7. Spherical Au NPs printed along with the formation of large Au slabs.

The origin of the slabs is unclear but is hypothesized to be the outer rings of the craters where the Au is softened but not completely melted. Forward momentum from the molten Au in the center of the crater expanding away from the substrate may pull and rip the softened slabs away from the remaining film on the substrate.

In summary, the material removal threshold dependence on film thickness was determined for Ni thin films. It was found that the absorption of laser light was dependent on film thickness, which changed the material removal thresholds from the film. The transition from homogeneous to heterogeneous nucleation of voids at the interface also played a major role in decreasing the removal threshold. Heterogeneous void nucleation at the interface induces a digital removal of material from the interface and also results in rough surfaces. Material removal from interfaces was used to print NPs onto substrates; the NPs were characterized with TEM and also used to grow CNTs. NP formation with narrow size distributions after irradiation of thin films with ns laser pulses has been demonstrated [Murray 2008], but the mechanisms of material removal after ns irradiation are different compared to fs irradiation. After fs irradiation, heterogeneous void nucleation induced by rapid material expansion allows for material

removal at the interface, while material removal only occurs within the film after ns irradiation. By breaking the thin film at the interface after fs irradiation, it may be possible to control the amount of material removed after each laser shot by changing the film thickness, controlling the size of the printed NPs. This process will be a subject of future study.

References

S. Amoruso, R. Bruzzese, C. Pagano, and X. Wang, *Features of plasma evolution and material removal efficiency during femtosecond laser ablation of nickel in high vacuum*, Applied Physics A **89**, 1017 (2007).

Dennis, J. K. and Such, T. E. (1972). *Nickel and chromium plating*. Cambridge: Woodhead Publishing Ltd.

D. Derkacs, S. H. Lim, P. Matheu, W. Mar, and E. T. Yu, *Improved performance of amorphous silicon solar cells via scattering from surface plasmon polaritons in nearby metallic nanoparticles*, Applied Physics Letters **89**, 093103 (2006).

F. Fiévet, P. Germi, F. de Bergevin, and M. Figlarz, *Lattice parameter, microstrains and non-stoichiometry in NiO. Comparison between mosaic microcrystals and quasi-perfect single microcrystals*, Journal of Applied Crystallography **12**, 387 (1979).

J. Güdde, J. Hohlfeld, J. G. Müller, and E. Matthias, *Damage threshold dependence on electron–phonon coupling in Au and Ni films*, Applied Surface Science **127**, 40 (1998).

L. Harris, J. K. Beasley, and A. L. Loeb, *Reflection and transmission of radiation by metal films and the influence of nonabsorbing backings*, Journal of the Optical Society of America **41**, 604 (1951).

Y. Kaganovskii, H. Vladomirsky, and M. Rosenbluh, *Periodic lines and holes produced in thin Au films by pulsed laser irradiation*, Journal of Applied Physics **100**, 044317 (2006).

Y. Kobayashia, H. Nakashimaa, D. Takagib, and Y. Homma, *CVD growth of single-walled carbon nanotubes using size-controlled nanoparticle catalyst*, Thin Solid Films **464-465**, 286 (2004).

E. Leveugle, D. S. Ivanov, and L. V. Zhigilei, *Photomechanical spallation of molecular and metal targets: molecular dynamics study*, Applied Physics A **79**, 1643 (2004).

P. T. Murray and E. Shin, *Formation of silver nanoparticles by through thin film ablation*, Materials Letters **62**, 4336 (2008).

Y. N. Picard, D. P. Adams, J. A. Palmer, and S. M. Yalisove, *Pulsed laser ignition of reactive multilayer foils*, Applied Physics Letters **88**, 144102 (2006).

Y. N. Picard, D. P. Adams, and S. M. Yalisove, *Femtosecond laser interactions with Co/Al multilayer films*, Materials Research Society Symposium Proceedings **850**, MM1.9.1 (2005).

J. Trice, D. Thomas, C. Favazza, R. Sureshkumar, and R. Kalyanaraman, *Pulsed-laser-induced dewetting in nanoscopic metal films: Theory and experiments*, Physical Review B **75**, 235439 (2007).

S. L. Tripp, S. V. Pusztay, A. E. Ribbe, and A. Wei, *Self-assembly of cobalt nanoparticle rings*, Journal of the American Chemical Society **124**, 7914 (2002).

M. Vorbau, L. Hillemann, and M. Stintz, *Method for the characterization of the abrasion induced nanoparticle release into air from surface coatings*, Aerosol Science **40**, 209 (2009).

S. S. Wellershof, J. Hohlfeld, J. Gudde, and E. Matthias, *The role of electron-phonon coupling in femtosecond laser damage of* metals, Applied Physics A **69**, S99 (1999).

Chapter 5
Ultrafast Laser Interactions with Multiple Interfaces

It has been shown in previous studies that the irradiation of transparent films, such as SiO_2 on a Si substrate, with fs and ns laser pulses forms blister structures at the interface [McDonald 153121 2006, Serrano 2002]. Delamination of the SiO_2 from the Si substrate is initiated when the laser melts the Si, bonds are broken at the interface, and a combination of material removal and stress relaxation lifts the SiO_2 up and away from the substrate forming a domed surface (blister). The blisters are hollow and can be connected to form microfluidic tubes [McDonald 183113 2006].

This chapter extends this work and will show that blisters may be formed at a Ni-SiO_2 interface. The morphology of the blisters is not only dependent on pulse length but also on interaction of the laser pulses with the underlying Ni film. It will be shown that the properties of buckling at the Ni-SiO_2 interface have similarities to the Si-SiO_2 interface, but the presence of a Ni film at the Ni-Si interface and its thickness introduce new blistering behaviors.

The 3-D stacking of microstructures for solar and battery applications is required to obtain high energy densities [Notten 2007]. Microtubes formed at metal-SiO_2 interfaces have the potential to form devices which do not exist for microtubes made at Si-SiO_2 interfaces. Forming microfluidic tubes at thin Ni-SiO_2 interfaces opens the possibility of stacking microfluidics, and forming stacked microfluidic tubes has the potential to create 3-D liquid anode, metal solid cathode, glass conduction membrane energy storage devices for any application which requires conductive layers. It will also be shown that using thin Ni films, flexible microfluidics are produced, which have the potential for forming in-plane microfluidic pumps and valves.

The phenomena observed at the Ni-SiO_2 interface will finally be extended to glass-glass interfaces and phenomena which were observed at the Si-SiO_2 interface.

Section 5.1 Ultrafast Laser Formation of Microstructures at Substrate-Ni Film-SiO_2 Interfaces

In order to study microstructure formation at metal-SiO_2 interfaces, buckling of SiO_2 at Ni-SiO_2 interfaces is explored in this section. A 1 µm layer of SiO_2 was deposited onto the 70 nm Ni films on Si substrates discussed in Chapter 4. After irradiation, blister features with diameters on the order of the laser spot size are formed, shown in Figure 5.1.1.

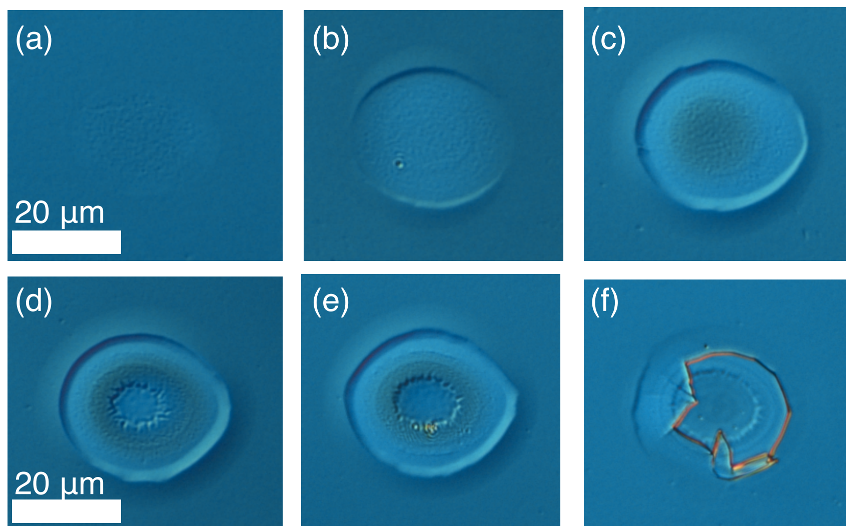

FIG. 5.1.1. DIC images of blisters produced at normal incidence at the interface between a 70 nm Ni film and 1 µm of SiO_2. (a) Fluence = 0.54 J/cm^2. (b) 0.64 J/cm^2. (c) 0.73 J/cm^2. (d) 0.81 J/cm^2. (e) 0.91 J/cm^2. (f) A broken blister. Fluence = 1.1 J/cm^2.

Damage to the Ni beneath the SiO_2 is seen in Figure 5.1.1(a) at fluences of 0.54 J/cm^2. Increasing the fluence to 1.1 J/cm^2, Figure 5.1.1(f), completely removes the SiO_2 layer and breaks the blister. Figures 5.1.2(a) and (b) show height profiles of typical blisters.

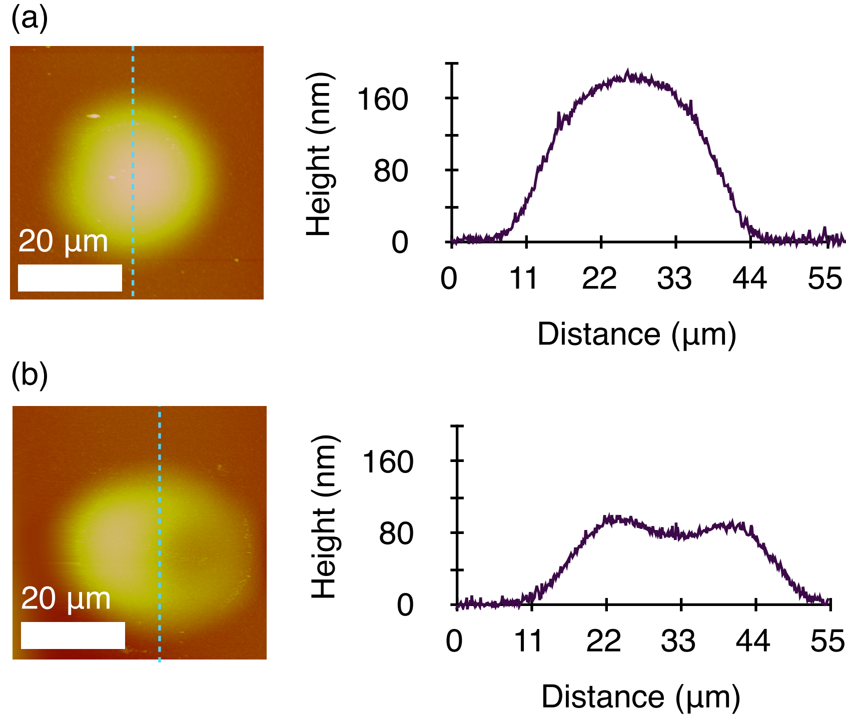

FIG. 5.1.2. AFM images and traces of blisters produced at normal incidence. (a) Laser fluence = 0.73 J/cm^2 (b) Laser fluence = 1.00 J/cm^2. The image and trace indicates the blister has collapsed.

Blisters form at fluences ≧ 0.64 J/cm^2, and blister radii increase linearly with fluence, shown in Figure 5.1.3(a). Blister height also increases linearly with fluence, as has been seen in other works [McDonald 2010] until fluences above 0.82 J/cm^2, where the blister height plateaus and then decreases with increasing fluence, Figure 5.1.3(b).

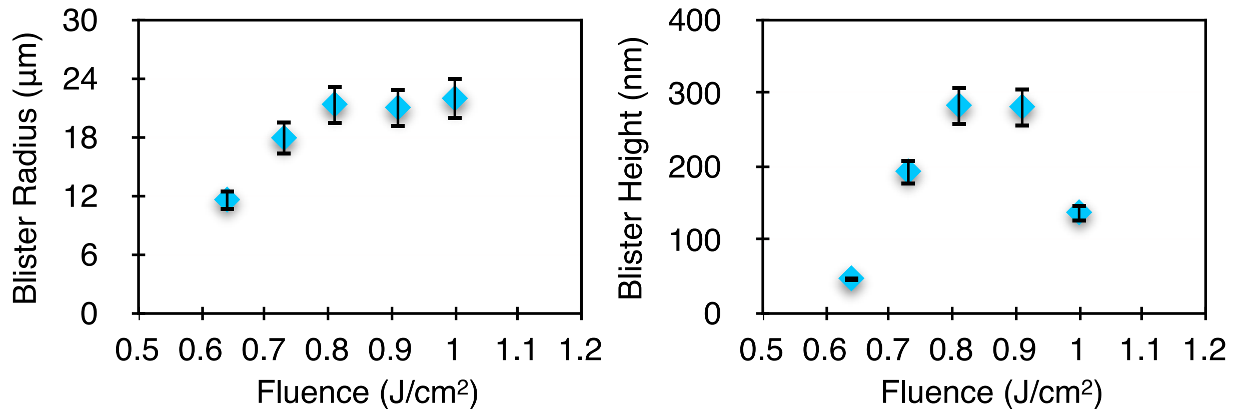

FIG. 5.1.3. Blister dimensions vs. fluence after irradiation of a 70 nm Ni-SiO_2 interface.

At a Si-SiO_2 interface, blister formation is consistent with a physical model where the incident laser pulse passes through the SiO_2, is absorbed by the Si underneath, and bonds at the interface are broken. The SiO_2 layer then buckles to release the stress at the interface [McDonald 2010, Serrano 2002]. Since the Ni-SiO_2 interface is under compressive stress, release of stress at the Ni-SiO_2 interface is expected to be partially responsible for the blister formation in Figure 5.1.1. However, the peak and decrease of the blister height is a strong indication that the blisters are collapsing after the pulse has turned off. Therefore, heat transfer from the Ni film to the SiO_2 layer cannot be excluded from a model seeking to fully explain the blistering phenomenon.

Heat transfer to the SiO_2 layer is usually associated with blister formation using *nanosecond* pulses, where the pulse length is comparable to the time scale of blister formation [Serrano 2002]. At these time scales, heat transfer from the hot Si to the SiO_2 raises the SiO_2 above its glass transition temperature (T_g) of ~1200 °C causing deformation and subsequent collapse of the blister. In our study, heat transfer while the laser pulse is on is non-existent, the laser pulse turns off long before the electrons equilibrate with the lattice a few picoseconds (ps) later. Also, little modification of the SiO_2 due to the laser is expected as the fluence of the laser pulse is much less than the modification threshold of SiO_2 (2 J/cm^2) [Ashkenasi 1999]. Given this evidence, the most likely mechanism for blister collapse is heat transfer from the molten Ni to the SiO_2, *after* bonds at the Ni-SiO_2 interface are broken.

Collapse of the blisters at the 70 nm Ni-SiO_2 interface occurred at similar fluences as pit formation in the 70 nm Ni film, discussed in Section 4.1. Blister formation at both the Si-SiO_2 interface and the 70 nm Ni-SiO_2 interface only occurred at fluences above the Si and Ni material removal thresholds. It has been hypothesized that material removal plays a role in blister formation [McDonald 2010], therefore, pit formation may play a role in blister collapse.

The number of pits increases with fluence, more Ni is removed, and the amount of Ni striking the underside of the blister increases. Once the Ni film partially melts after irradiation, bonds are broken at the Ni-SiO_2 interface, releasing stress in the SiO_2 layer. As the SiO_2 layer expands away from the Ni, the melt front proceeds through the thin Ni film towards the Ni-Si interface. When the melt front reaches the Ni-Si interface, bonds

are broken and hot, molten Ni is released from the Si substrate striking the SiO_2 above, illustrated in Figure 5.1.4(a). The increased mass striking the SiO_2 adds additional thermal mass at the center of the blister, which raises the temperature of the SiO_2 above its glass transition temperature, inducing flow and subsequent collapse of the blister. The result of this process is seen in Figure 5.1.2(b) and illustrated in Figure 5.1.4(b).

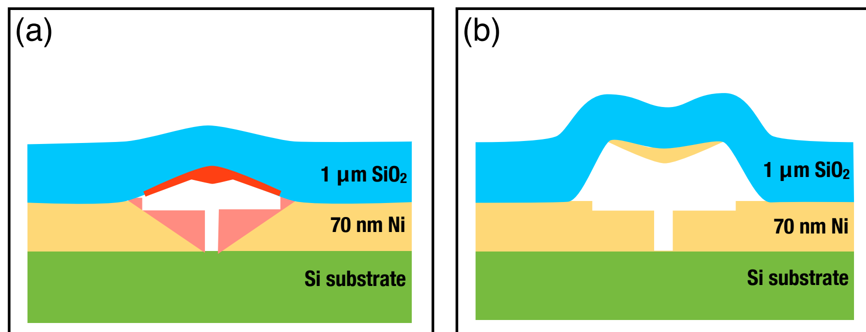

FIG. 5.1.4. Illustration of pit formation and subsequent collapse of blister structures after irradiation in the high fluence regime. (a) Heat transfer shown in pink extends to the Ni-Si interface, propelling hot Ni (red) away from the interface and striking the SiO_2 above. (b) Flow is induced in the SiO_2 causing deformation of the SiO_2 and collapse of the blister.

At lower laser fluences, the increased mass of Ni is not released from the interface and the SiO_2 temperature doesn't increase and the blister doesn't collapse.

Microtubes were formed at the 70 nm Ni-SiO_2 interface by overlapping successive laser pulses at a fluence of 0.54 J/cm^2, Figure 5.1.5. Microfluidic flow was demonstrated by drawing the microtubes to the edge of the sample, opening the microtubes to air and placing a water drop at the edge of the sample.

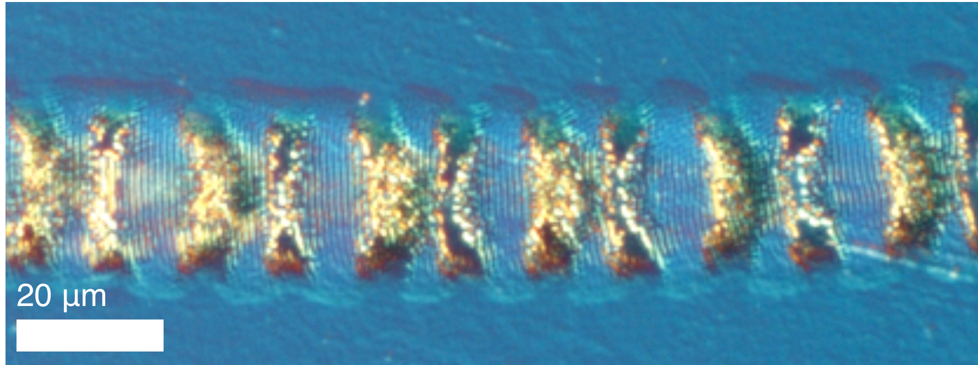

FIG. 5.1.5. DIC image of microtube formation at a 70 nm Ni-SiO_2 interface.

Performing AFM on the microtube in Figure 5.1.5 has shown the microtube collapses periodically in the regions with gold color, where the laser pulses overlapped. Dark contrast from the DIC image in these regions strongly indicates complete removal of the Ni film where the laser pulses overlapped. This data shows that flow can be induced in the SiO_2 and collapse of the microtube at lower laser fluences if multiple laser shots are used. Laser induced periodic structures are seen in the Ni underneath the glass and will be discussed in Chapter 6. Future studies of this system will involve cutting blisters open with a focused ion beam and investigating the underside of the raised SiO_2 with SEM to determine how much Ni was deposited onto the SiO_2 at varying fluences.

Varying thicknesses of Ni films were also sputtered onto microscope slides, and SiO_2 with a thickness of 650 nm was deposited onto the Ni films to determine what effect decreasing the Ni film thickness has on the blister behavior. It was found that the blister threshold varies with Ni film thickness, shown in Figure 5.1.6.

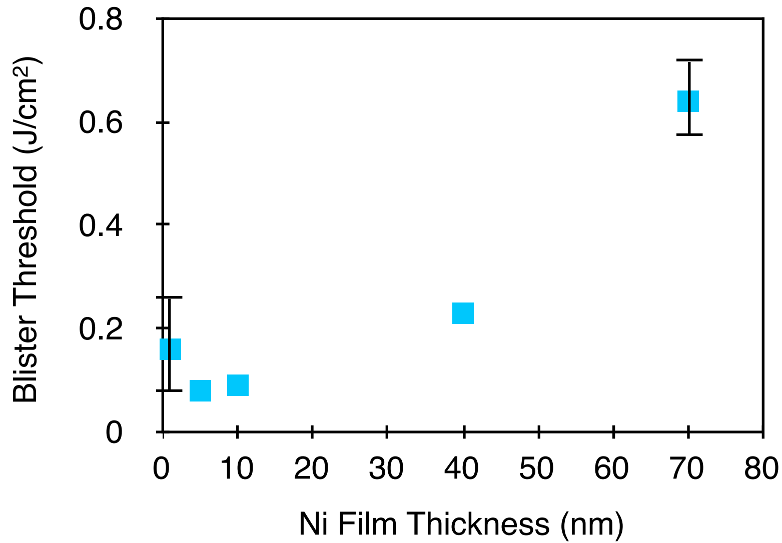

FIG. 5.1.6. Blister threshold as a function of Ni film thickness deposited on glass substrates. As the Ni thickness is decreased the threshold decreases until 5 nm Ni when it starts to increase again.

Seen in Figure 5.1.6, for Ni film thicknesses 1, 5, 10, and 40 nm, blistering occurred at fluences much lower than those required to form blisters at both the 70 nm Ni film-SiO_2 interface and the Si-SiO_2 interface. This is a direct result of the decrease of Ni film damage thresholds with decreasing Ni film thickness on glass substrates. The damage threshold for a 1 nm of Ni film on glass without the deposited SiO_2 film is 0.13 J/cm^2, compared to the threshold of 0.32 J/cm^2 for bulk Ni. The Ni film melts at lower fluences as the Ni film thickness decreases, leading to a lower blister threshold for thinner Ni films. Future studies will focus on directly measuring the absorptance of these films to determine the absorbed fluence rather than only the incident fluence on the Ni film-SiO_2 structure.

When microtubes were formed at the glass substrate-1 nm Ni-SiO_2 interface and water flow was initiated, the contrast of the microtubes drastically changed, shown in Figure 5.1.7.

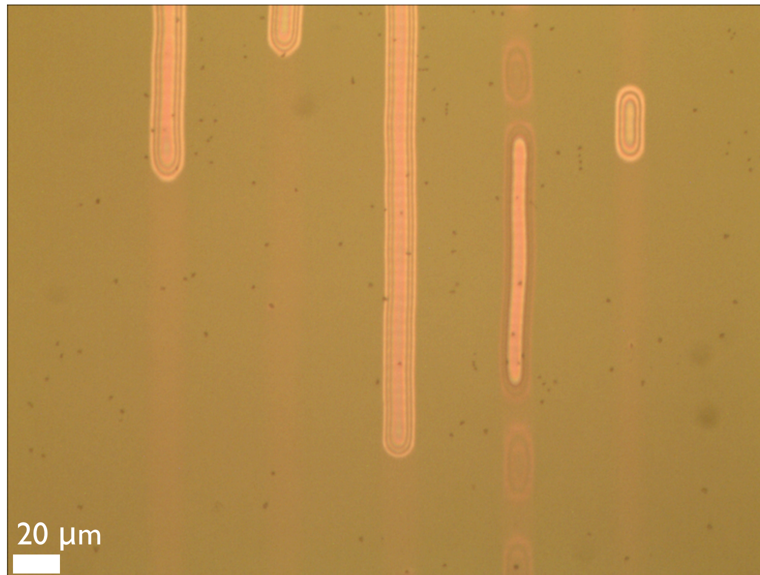

FIG. 5.1.7. Bright field OM image of microtubes formed at a glass substrate-1 nm Ni-SiO_2 interface using fluence of 0.20 J/cm^2. After initiation of water flow, Newton's rings were seen to vanish in parts of the microtubes.

Newton's fringes visible as lines of color running parallel to the microtube edges are indicators that the SiO_2 is raised above the Ni film surface. Portions of the microtubes in Figure 5.1.7 lost their Newton's fringe contrast and exhibited a pink contrast. Figure 5.1.8(a) shows an OM image of a microtube before microfluidic flow is initiated. After microfluidic flow, portions of the microtubes darken along the edges of the microtube, Figure 5.1.8(b). An AFM image of the region of the microtube which straddles the upper half of the image in Figure 5.1.8(c) with Newton's fringes and the lower half with little optical contrast shows the microtube collapsed from a > 1 μm height to an ~ 25 nm height in the regions with little optical contrast, Figure 5.1.8(d).

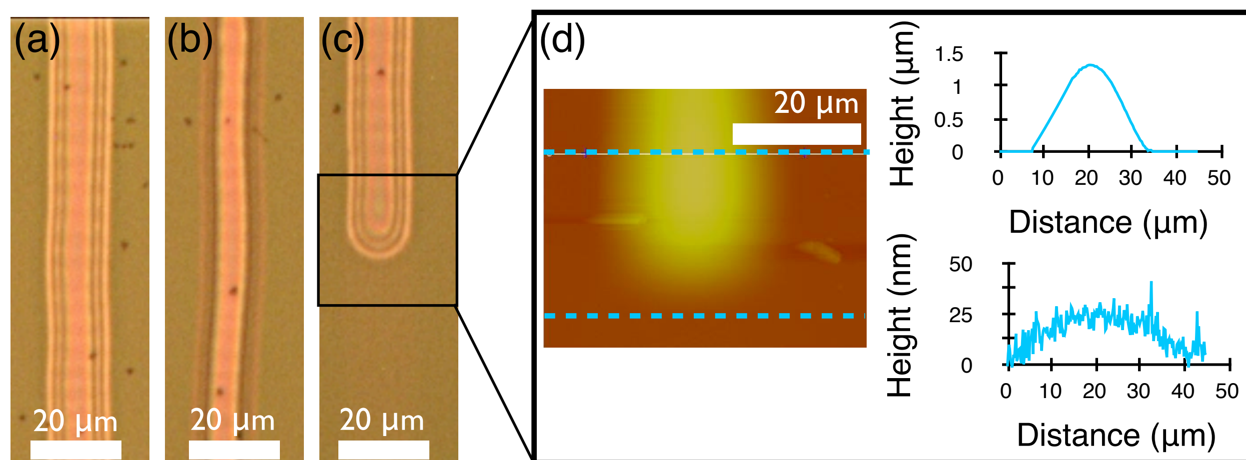

FIG. 5.1.8. (a) Bright field OM image of a microtube formed at 0.20 J/cm² before microfluidic flow. (b) Bright field OM image of a microtube after water flow via open ends of the tube at the edge of the sample. The dark contrast of the fringes near the edge of the microtube indicate water has partially filled the microtube. (c) Bright field OM image of a microtube after water flow. The loss of Newton's fringes in the bottom half of the image and appearance of a lighter pink contrast indicate the microtube collapsed. d) AFM image and traces of a portion of the tube in Fig 3(c). The image straddles the area where optical fringes are present in the upper part of the image and disappear in the lower part. The microtube collapsed to an ~ 25 nm height in the lower half of the image, compared to the 1.35 µm height in the upper half of the image.

The loss of Newton's fringes and collapse of microtubes after the initiation of water flow was never observed at the Si-SiO_2 interface or for the Ni-SiO_2 interface for Ni film thicknesses ≥ 5 nm. The collapse of the 1 nm Ni-SiO_2 microtubes suggests they are *flexible* while microtubes formed using Si and thicker Ni films as absorbing layers are more rigid. Rigid microtubes support microfluidic flow without collapsing.

Their rigidity suggests the loss of internal stresses within the buckled SiO_2 as a result of plastic deformation has occurred. Significant plastic deformation of the buckled SiO_2 is expected to occur only if the SiO_2 reaches temperatures close to or greater than the glass transition temperature (T_g) of SiO_2 thin films, ~ 1200 °C [Mitra 1980]. However, the laser fluence used to form microtubes is an order of magnitude lower than the modification threshold of SiO_2 (~ 2 J/cm²) [Ashkenasi 1999], therefore, heating of the SiO_2 due to absorption of the laser light is minimal.

The SiO_2 most likely heats due to heat transfer from the bulk substrate to the SiO_2 before cooling. After irradiation of the Si-SiO_2 interface by the 150 fs light, the light passes through the overlying SiO_2 and is absorbed by the crystalline Si substrate [McDonald 153121 (2006)]. At least a 20 nm thick layer of Si melts within a few

picoseconds after absorption and is in a molten state for several nanoseconds before thermal quenching [Downer 1985]. Before thermal quenching of the molten Si, heat transfer from hot Si to SiO_2 in the near vicinity of the SiO_2 could raise the temperature of the SiO_2 above its T_g after the SiO_2 layer buckles [McDonald 153121 (2006)].

When the loss of laser light due to the reflectivity of the bulk Si and Ni substrates and the 1 nm thin film is approximated using the Fresnel equations, the effective blister threshold fluence of the 1 nm film-SiO_2 interface (~ 8 mJ/cm^2) is two orders of magnitude lower than the effective blister thresholds for the bulk Si-SiO_2 interface (0.12 - 0.15 J/cm^2) [McDonald (2010)] and bulk Ni-SiO_2 interface (~ 0.14 J/cm^2). Since bond breaking is the driving mechanism for the initiation of buckling and blister formation, a lower threshold fluence corresponds to a lower energy requirement to break bonds at the 1 nm film-SiO_2 interface, which will correspond to a lower temperature.

Irradiation of the bulk Ni and Si substrates is illustrated in Figure 5.1.9(a). The Gaussian energy distribution of the laser pulse means regions (i) are at low temperatures, and buckling of the SiO_2 away from the hot bulk material in region (iii) reduces radiative heat flow into region (iii). Therefore, after buckling of the SiO_2, plastic deformation of the SiO_2 should only occur in regions (ii) after the SiO_2 temperature increases above its T_g and flow is induced in the SiO_2. After the SiO_2 cools, these regions are termed the “roots” of the microtube and they prevent collapse of the bulk substrate-SiO_2 microtubes. Further evidence for the presence of a root is seen when edges of the microtube crack in the regions of large stress concentrations [McDonald 2010]. Region (iii) of the SiO_2 pops up and away from a Si substrate and flattens, while the root of the microtube, region (ii), acts as a local plastic hinge. This is strong evidence that after microtube formation, region (iii) is elastically deformed while regions (ii) are plastically deformed.

After laser irradiation of the 1 nm film-SiO_2 interface, shown in Figure 5.1.9(b), the laser light passes through the SiO_2 and irradiates the interface. Laser energy is coupled to the interface via light absorption by Ni which hasn’t oxidized, dangling bonds, or adsorbed atoms and molecules at the interface and the film heats. Absorption of laser light within Ni films with thicknesses ≤ 5 nm will be a subject of future study since

very thin amounts of Ni aren't expected to have low damage thresholds due to the presence of an oxidized Ni layer of at least 2 nm [Song 2008].

After heating, bonds at the 1 nm film-SiO_2 interface are broken, and the breaking of bonds at the interface releases compressive stress causing the SiO_2 to buckle and form a blister. The lower temperatures and smaller thermal mass of the 1 nm film compared to the > 20 nm of molten bulk material result in little heat transfer from the film to the SiO_2 and the SiO_2 is not raised above its T_g. The microtube edges are elastically deformed and flexible, Figure 5.1.9(b); however, some plastic deformation may still occur due to large compressive stresses at the microtube edges [Coupeau 2004].

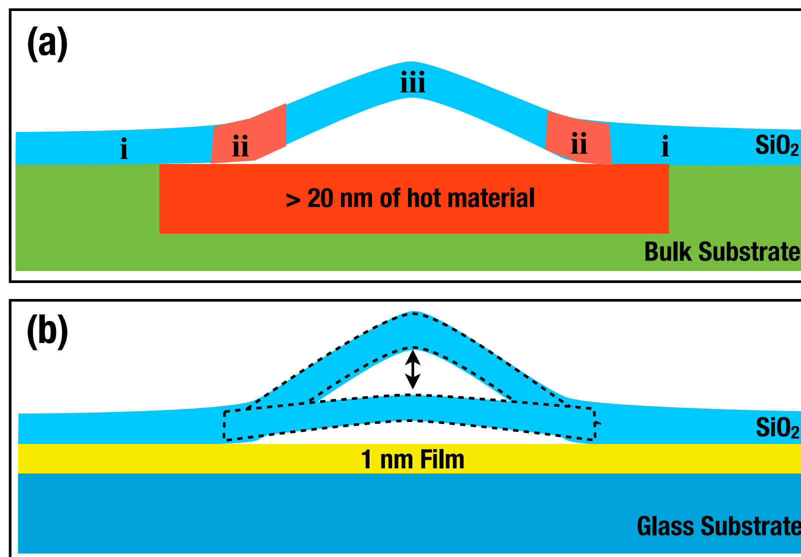

FIG. 5.1.9. Illustrated cross-sections of microtubes after laser irradiation and before thermal quenching. (a) Sections (i), little heat conduction from the bulk substrate to the SiO_2 due to low laser fluence. Section (iii), little radiative heat transfer. Sections (ii) represent the roots of the tubes. Conduction and radiation of heat from hot material to the SiO_2 raises the SiO_2 above its T_g and forms the root. (b) Low heat transfer from the laser irradiated film to the SiO_2 occurs, no flow is induced in the SiO_2, and the microtube is flexible. Two microtube states are shown, the taller original microtube height and the collapsed height.

The microtubes collapsed in several different regions along the length of the microtube after the initiation of water flow and water rarely filled the entire cross-section without the microtube collapsing. Complete filling of the microtube cross-section could be a requirement for microtube collapse and may be initiated by surface tension of the water pulling the separated SiO_2 layer closer to the underlying substrate.

Further evidence for the lack of a root is seen in Figure 5.1.10 which shows a cross section from an AFM image of a broken blister at the 1 nm film-SiO_2 interface. The edge of the blister is not elevated above the original glass surface as was the case with the Si-SiO_2 blisters [McDonald 2010]. An elevated rim at the edge of broken Si-SiO_2 blisters is a strong indicator of an SiO_2 layer which has undergone plastic deformation.

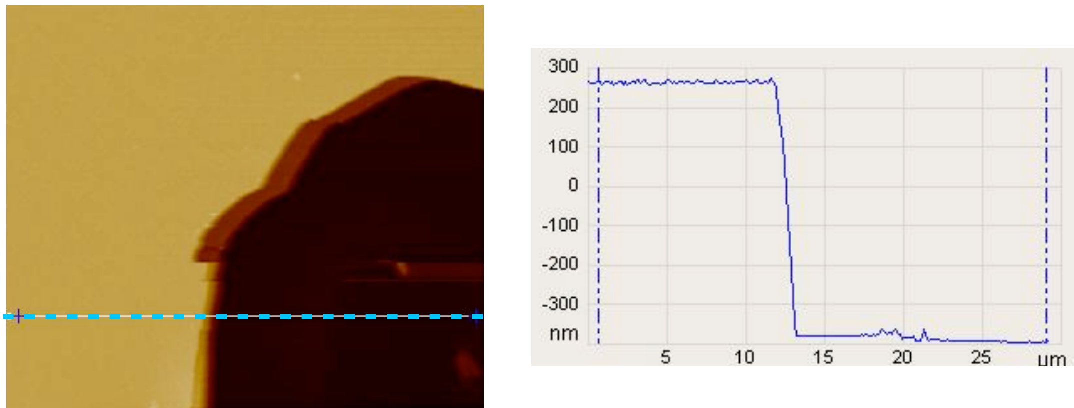

FIG. 5.1.10. AFM image and trace of the edge of a broken blister at the 1 nm film-SiO_2 interface. The rim of the broken blister is flat, indicating little to no plastic deformation of the SiO_2 has occurred.

With lower Ni film thicknesses, the lack of a root should mean that stress predictions derived from blister dimensions will match the measured stress in the film. This was not the case with blisters formed at the Si-SiO_2 interface [McDonald 2010]. Stress in the Si-SiO_2 wafers was calculated by measuring changes in wafer radius of curvature before and after SiO_2 growth with a Flexus laser interferometer at the UM LNF. Since the thin Ni film and SiO_2 were deposited onto microscope slides it was not possible to measure film curvature using the interferometer. Future studies will focus on using Multi-beam Optical Sensors (MOS) available at k-Space Associates, Inc. to obtain 2D stress profiles of the thin Ni and SiO_2 films on microscope slides. Thin Ni and SiO_2 films may also be deposited onto Si wafers to form flexible microfluidic tubes. Stress measurement could then be performed using the Flexus interferometer, which will also be a subject of future study.

Future studies will also focus on performing measurements of the absorptance of Ni film-SiO_2 multilayer structures to determine the absorbed fluence rather than only the

incident fluence. The composition and amount of oxidation present in Ni films with thicknesses ≤ 5 nm could possibly be determined using transmittance and reflectivity measurements.

Section 5.2 Revisiting Femtosecond Laser Interactions with Single Interfaces

Section 4.2 of this thesis focused on the fs laser interaction with single interfaces between a SiO_2 substrate and Ni thin films. Interfaces were further explored in Section 5.1 where the interaction of fs laser pulses with multiple interfaces was studied. The knowledge gained about root formation in Section 5.1 will now be applied to single glass substrate-SiO_2 interfaces and Si-SiO_2 interfaces where heat transfer and root formation plays a large part in blistering behavior at these interfaces.

If defects at an interface can induce material removal after irradiation, then it should be possible to separate the interface between two similar materials. To test this hypothesis, the thin Ni film was removed from the glass substrate SiO_2 interface by depositing SiO_2 directly onto a glass substrate. Figure 5.2.1(a) shows a blister formed at a glass substrate-SiO_2 interface with Newton's rings visible after irradiation with a single laser pulse.

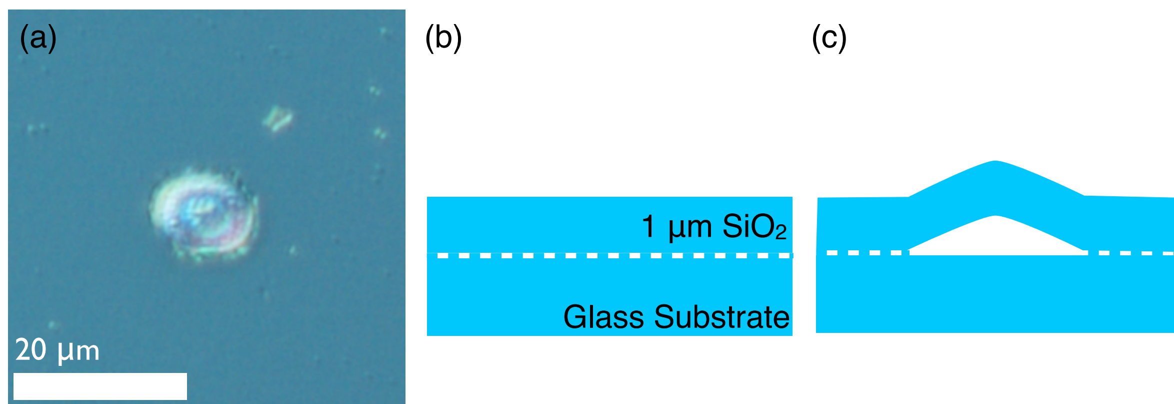

FIG. 5.2.1. (a) DIC image of blister formation at a glass substrate-SiO_2 interface at a fluence of 3.0 J/cm^2. (b) Illustration of defects at the glass substrate-SiO_2 interface. (c) Illustration of separation of the SiO_2 layer from the glass substrate at the interface and blister formation after irradiation by a single laser pulse.

Even without the thin Ni film present at the interface to absorb laser light, the SiO_2 layer is separated from the underlying substrate. The fluence used to form blisters at this interface, 3.0 J/cm^2, is above the single shot damage threshold of SiO_2 [Ashkenasi 1999]. Therefore, after irradiation the SiO_2 melts and defects at the substrate SiO_2 interface, Figure 5.2.1(b), provide heterogeneous nucleation sites for void formation and growth, allowing the SiO_2 to separate from the substrate and form a blister, Figure 5.2.1(c).

If successive laser shots are overlapped at this fluence, microtube formation is sporadic and the microtubes break in many areas along their length. The SiO_2 is brittle since the incident 3.0 J/cm^2 raises the SiO_2 above its T_g, inducing plastic deformation after the first laser shot. The blister then breaks after irradiation by the second shot. The thin Ni film discussed in Section 5.1 allows for blister and microtube formation at fluences which are an order of magnitude lower than that used in Figure 5.2.1, the SiO_2 is not raised above its T_g, and a root isn't formed.

If root formation through heat transfer from the hot substrate to the SiO_2 layer is playing a role in microtube formation then it should be possible to form microtubes at fluences below the single pass microfluidic tube formation threshold at a Si-SiO_2 interface. The single pass threshold for microfluidic tube formation was found to be 0.30 J/cm^2, using 25% overlap of laser pulses at a Si-SiO_2 interface with a 1 µm SiO_2 layer and 150 MPa compressive stress. Irradiation after a single pass at 0.20 J/cm^2 doesn't form a microtube and Figure 5.2.2(a) shows an ~ 3 nm increase in height, which likely corresponds to a decrease in density of amorphous Si compared with crystalline Si [Custer 1994], in the irradiated regions. After a second laser pass irradiating the same region, the SiO_2 layer is raised to a height which is > 150 nm above the original surface, Figure 5.2.2(b) and mirofluidic flow was demonstrated.

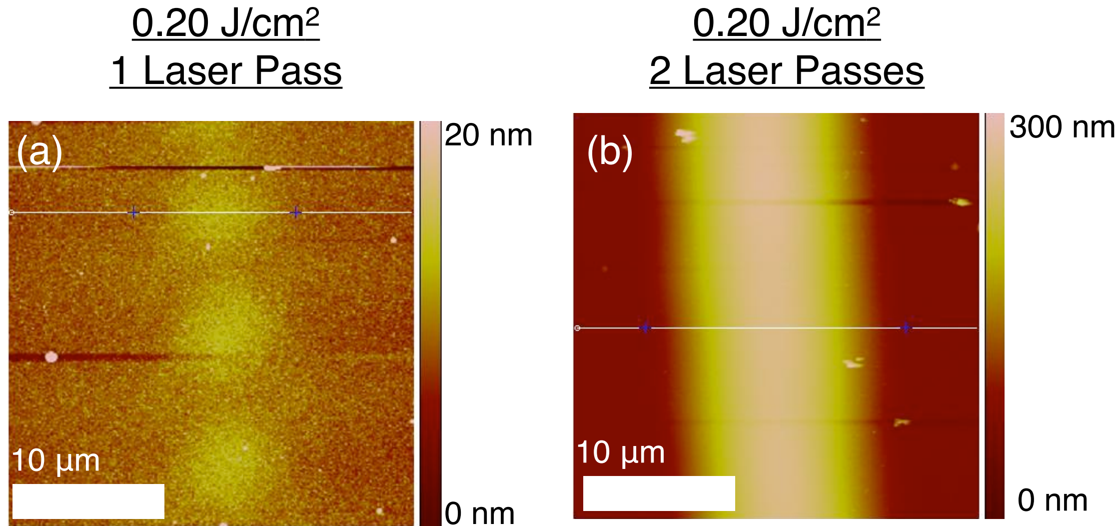

FIG. 5.2.2. (a) AFM image of irradiation of 1 µm SiO_2 on a Si substrate with 1 laser pass. No microfluidic flow was observed. (b) AFM image of the Si-SiO_2 interface with 3 laser passes. The height increased and microfluidic flow was observed.

After 2 passes with laser pulses, the height of the SiO_2 layer increased by 2 orders of magnitude and microfluidic flow was observed. The first laser pass forms amorphous Si (indicated by a slight height change in the AFM and a change in optical contrast), and amorphous Si has a thermal conductivity which is 2 orders of magnitude lower than crystalline Si [Wada 1996]. The amorphous Si layer formed from the first laser pass likely keeps the molten "pool" of Si formed after the second pass hot longer, forming a larger molten pool. A larger extent of molten Si will break a larger area of bonds at the Si-SiO_2 interface, initiating a combination of buckling and root formation which forms a microtube after subsequent laser passes.

The rigidity of microfluidic tubes formed from the overlap of laser pulses above the single pass microtube formation threshold at the Si-SiO_2 interface strongly indicates the presence of a root in those microtubes. Microfluidic tubes formed using multiple passes using fluence below the single pass threshold for tube formation were also rigid after microfluidic flow. Microtube rigidity, amorphous Si formation, and tube formation after multiple laser passes below the single pass threshold all suggest root formation is playing a strong role in microtube formation using varying fluences at the Si-SiO_2 interface.

In summary, it was found that the response of the underlying bulk substrate and thin films affects the blistering dynamics of thin SiO_2 films. Heat transfer from the underlying material to the SiO_2 film induces plastic deformation of the SiO_2, which changes both blister and microtube properties. Decreasing the film thickness sandwiched between a glass substrate and SiO_2 film allowed for blister formation at lower temperatures and the formation of blisters which aren't brittle. Overlap of the these blisters formed microtubes and microtube flexibility was demonstrated, confirming that blisters formed at the thin film-SiO_2 interface are not brittle. Future studies are needed to separate the roles material ablation and breaking bonds at the thin film-SiO_2 interface play in blister formation.

References

D. Ashkenasi, M. Lorenz, R. Stoian, and A. Rosenfeld, *Surface damage threshold and structuring of dielectrics using femtosecond laser pulses: the role of incubation*, Applied Surface Science **150**, 101 (1999).

C. Coupeau, P. Goudeau, L. Belliard, M. George, N. Tamura, F. Cleymand, J. Colin, B. Perrin, J. Grilhé, *Evidence of plastic damage in thin films around buckling structures*, Thin Solid Films **469-470**, 221 (2004).

J. S. Custer, M. O. Thompson, D. C. Jacobson, J. M. Poate, and S. Roorda, *Density of amorphous Si*, Applied Physics Letters **64**, 437 (1994).

M. C. Downer, R. L. Fork, and C. V. Shank, *Femtosecond imaging of melting and evaporation at a photoexcited silicon surface*, Journal of the Optical Society of America B **2**, 595 (1985).

J. P. McDonald, V. R. Mistry, K. E. Ray, and S. M. Yalisove, *Femtosecond pulsed laser direct write production of nano- and microfluidic channels*, Applied Physics Letters **88**, 183113 (2006).

J. P. McDonald, M. D. Thouless, and S. M. Yalisove, *Mechanics analysis of femtosecond laser-induced blisters produced in thermally grown oxide on Si(100)*, Journal of Materials Research **25**, 1087 (2010).

S. K. Mitra, M. Amini, D. Fincham, and R. W. Hockney, *Molecular dynamics simulation of silicon dioxide glass*, Philosophical Magazine B **43**, 365 (1980).

P. H. L. Notten, F. Roozeboom, R. A. H. Niessen, and L. Baggetto, *3-D integrated all-solid-state rechargeable batteries*, Advanced Materials **19**, 4564 (2007).

J. R. Serrano, and D. G. Cahill, *Micron-scale buckling of SiO_2 on Si*, Journal of Applied Physics **92**, 7606 (2002).

S. Song and F. Placido, *An in-situ investigation of the surface oxidation of ultra-thin films of Ni and Hf*, Proceedings of SPIE **7101**, 710120 (2008).

H. Wada and T. Kamijoh, *Thermal conductivity of amorphous Si*, Japanese Journal of Applied Physics **35**, L648 (1996).

Chapter 6

Ultrafast Laser Formation of Laser Induced Periodic Structures

The following chapter explores LIPS formation on surfaces after irradiation of *features* at interfaces. The features were either created by the laser after irradiation with a single pulse or were deposited before irradiation using lithography. This chapter extends the idea that the laser-solid interaction is unique at interfaces and will show that not only is material removal unique at interfaces but the behavior of light is also altered by the interface.

The presence of an interface introduces surface roughness, and rough surfaces change the interaction of light in the near field of the surface. The importance of the behavior of light in the near field is exemplified by diffraction gratings [Cook 1960, Strickland 1985, Guosheng 1982], plasmonics [Ozbay 2006], surface enhanced raman spectroscopy [Kneipp 2008], and even the source of color for stained glass [Zayats 2005].

The nature of near field light coupling to a material surface has been shown to control LIPS formation, which was discussed in detail in Chapter 2 of this thesis. Briefly, early reports of LIPS formation varied the angle of incidence of the laser pulse with the surface and found a $\Lambda = \frac{\lambda}{1 \pm \sin\theta}$ dependence on LIPS periodicity Λ, where θ is the angle of incidence with the surface. This behavior was attributed to the interference of light scattered from the scratches and rough surfaces with the incident laser light. Further theories emerged which showed that Λ is usually slightly less than λ and surface plasmon polaritons (SPPs) can be excited by p-polarized light within the near surface and shift the value of Λ from λ. SPP excitation is usually only discussed for

surfaces which are randomly rough; after SPP excitation, the energy is coupled with the surface at a period Λ.

However, in this chapter, evidence will be presented which shows that a randomly rough surface is not required for LIPS formation. Multiple mechanisms are responsible for LIPS formation on a surface, and these mechanisms are dependent on the polarization direction of the light with surface features which are already present on the surface. Multiple sources will also be shown to be responsible for LIPS formation after irradiation with both single and multiple laser pulses.

It will be shown that LIPS formation can be controlled by placing features on the surface and irradiating these features with single laser pulses. By using these features, the study of LIPS formation was simplified and it was possible to deconvolve the different mechanisms of light interaction with the material surface. What was learned by irradiating these features is applied to irradiation of bulk material using multiple pulses. The random nature of LIPS formation, even in the presence of pre-existing features on the surface, means they have a multitude of applications where non-tamperable marking is desirable. Highly variable properties of the LIPS are orientation, amplitude, and periodicity. This chapter will explore the multiple factors which change these properties.

Section 6.1 Ultrafast Laser Formation of LIPS on Bulk Si

As in the other sections of this thesis, femtosecond irradiation of bulk materials with a single laser shot forms a crater, shown in Figure 6.1.1(a) and no LIPS are formed. If a defect is present on the surface before irradiation, however, LIPS form near the defect with an orientation mostly perpendicular to the laser polarization, within a small angle.

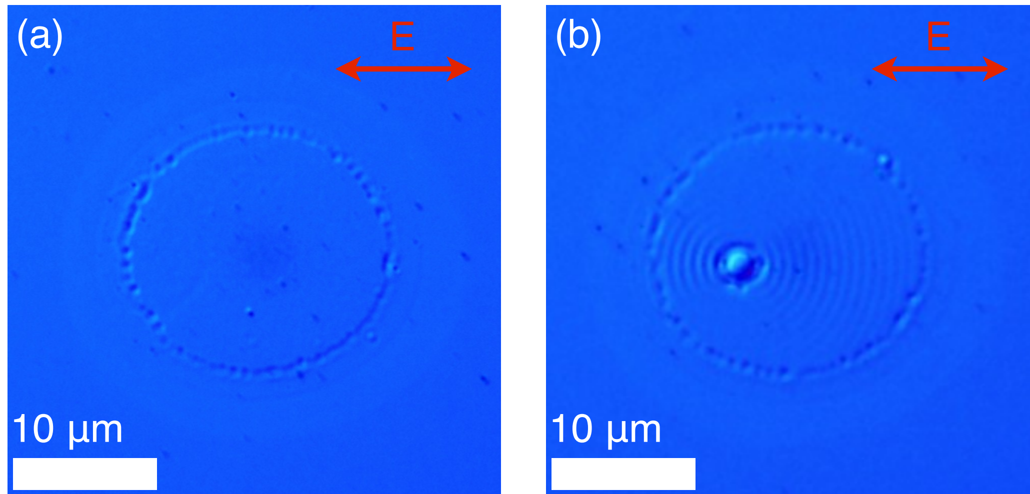

FIG. 6.1.1. (a) DIC image of a crater in Si after a single laser shot at 0.64 J/cm^2. (b) DIC of image of a crater in Si with LIPS forming near a defect.

Irradiation of the crater in the Si substrate with a second laser shot at the same fluence forms LIPS throughout the entire crater, Figure 6.1.2. Rotation of the polarization vector causes the orientation of the LIPS to change.

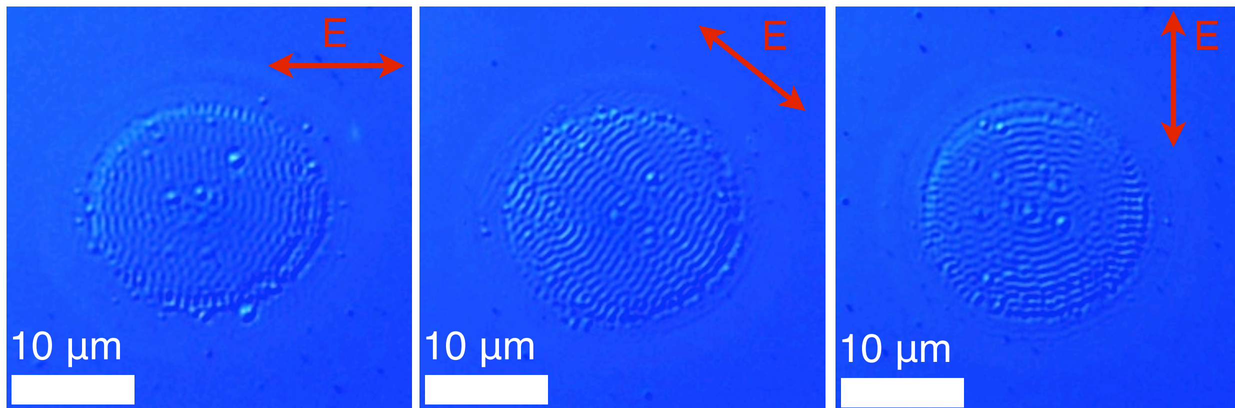

FIG. 6.1.2. DIC image of a crater in Si with ripples after 2 shots at 0.64 J/cm^2. (a) Horizontal polarization. (b) Polarization at a 45° angle. (c) Vertical polarization.

The LIPS are mostly oriented perpendicular to the laser polarization; however it can be seen in some areas that the LIPS follow the rim of the crater. These results lead us to 3 conclusions concerning LIPS formation: 1) A random surface roughness is not required for LIPS formation. 2) LIPS can form after a single laser shot if a feature is already present on the surface. 3) The shape of features already present on the surface can influence the orientation of the resulting LIPS.

SPP excitation is likely the dominant mechanism for LIPS formation in both 1 shot and 2 shot cases of bulk Si irradiation. After irradiation, the Si possesses a free carrier electron density which can support SPP excitation [Bonse 2009]. Also the LIPS are perpendicular to the laser polarization as predicted by theory [Guosheng 1982, Sipe 1983]; a result of the fact that SPPs can only be excited with p-polarized light [Zayats 2005]. In the next section further evidence will be shown which further supports the conclusions made above and a second mechanism for LIPS formation will be introduced.

Section 6.2 Ultrafast Laser Formation of Ripples at a Si-SiO_2 Interface

Microtube formation at a Si-SiO_2 interface studied in Chapter 5 involves the overlap of multiple laser shots, so it is expected that LIPS formation will occur in the microtube formation process. During microtube formation at a Si-SiO_2 interface, LIPS were observed in the Si substrate underneath the ~ 1 µm SiO_2 layer with OM, shown in Figure 6.2.1(a). By removing the SiO_2 layer by scraping the layer off with a knife, it was possible to perform AFM on the LIPS, Figure 6.2.1(b) and confirm the LIPS formed in the Si substrate.

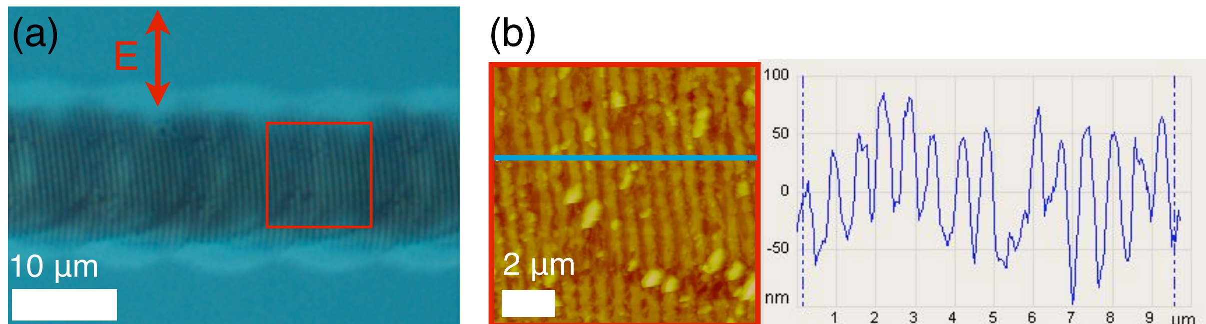

FIG. 6.2.1. (a) DIC image of LIPS formation at a Si-SiO_2 interface. (b) AFM image of LIPS formation at a Si-SiO_2 interface.

The periodicity of the LIPS was calculated by taking Fourier transforms of each LIPS period using the MATLAB code in Appendix 6. The average LIPS periodicity was 683 nm (standard deviation = 67nm), but the orientation of the LIPS was parallel to the laser polarization. LIPS which form after a low number of laser pulses on a Si substrate

are always oriented perpendicular to the laser polarization, while parallel to the polarization LIPS form after a higher number of pulses [Dufft 2009, Crawford 2007, Honda 2010, Costache 2004]. Even in these cases, LIPS with *both* perpendicular and parallel orientations are observed.

These results suggests a mechanism different than SPP excitation within a randomly rough surface is occurring since the presence of features from the previous laser shot has a strong affect on LIPS orientation. Figure 6.2.1(b) indicates a diffraction mechanism similar to the Huygens-Fresnel principle is occurring. The LIPS are following the outline of the features created from the previous laser shot, parallel to the laser polarization direction. The fact that the laser polarization still has an effect on the LIPS orientation if the polarization is rotated, however, suggests that SPP excitation is still playing a role in LIPS formation in these cases. The idea that features already present on the surface can affect LIPS formation and orientation is outlined below in Figure 6.2.2 with crater formation and subsequent LIPS formation near crater edges.

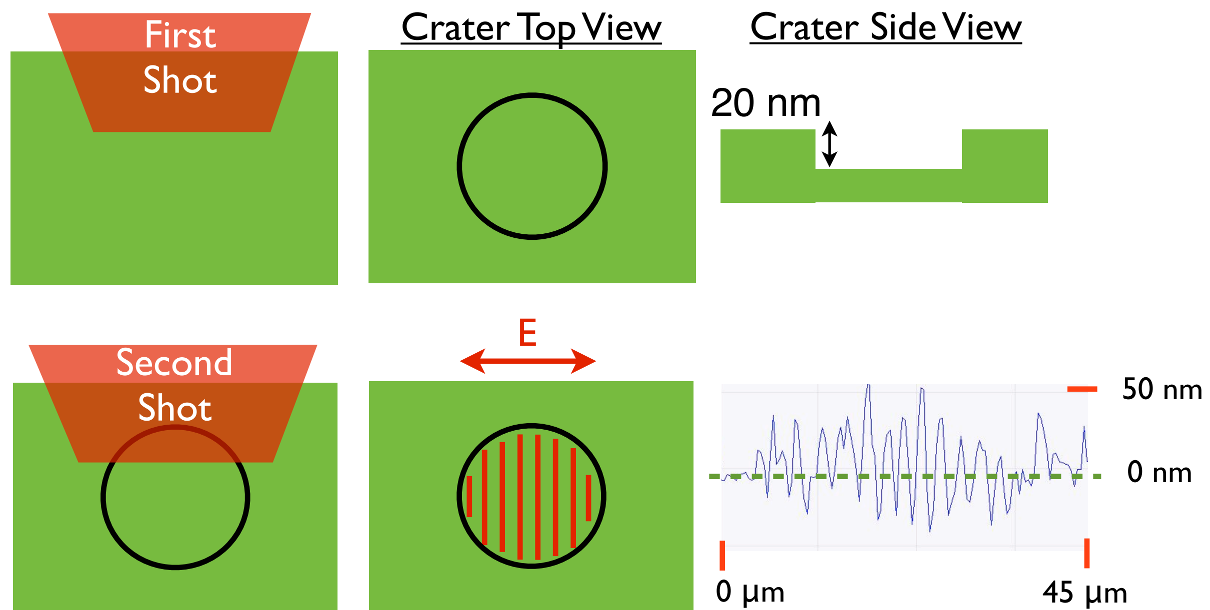

FIG. 6.2.2. Illustration of crater formation after a single laser shot and LIPS formation after the second laser shot. The crater edges formed after the first shot are hypothesized to act as sources for LIPS formation within the crater after the second shot.

The first shot forms a crater and the crater edges act as sources for LIPS formation during the second shot, forming LIPS along the crater edges and in the middle of the crater.

To test this hypothesis and determine if LIPS could form after irradiation of features with a single shot, Au microstructures are studied in the following section. Neither a crater or the overlying SiO_2 are present on the surface before irradiation. The role of SPP excitation and diffraction will also be explored in this section.

Section 6.3 Ultrafast Laser Formation of LIPS Near Au Microstructures

Au microstructures, “mesas” were deposited onto Si substrates with lithography at Sandia National Laboratories, Appendix 5. The Au layer was 100 nm thick and a 10 nm layer of Ti rests between the Au and Si for better adhesion of the Au to the substrate. The total height of the Au mesa above the Si surface was 110 nm. The RMS roughness of the original Au surface is < 1.5 nm.

A pristine square mesa is shown in Figure 6.3.1 with an ~ 40 µm $\frac{1}{e^2}$ diameter of the focused laser beam illustrated. The mesas were typically irradiated with the focused laser spot centered on a mesa edge.

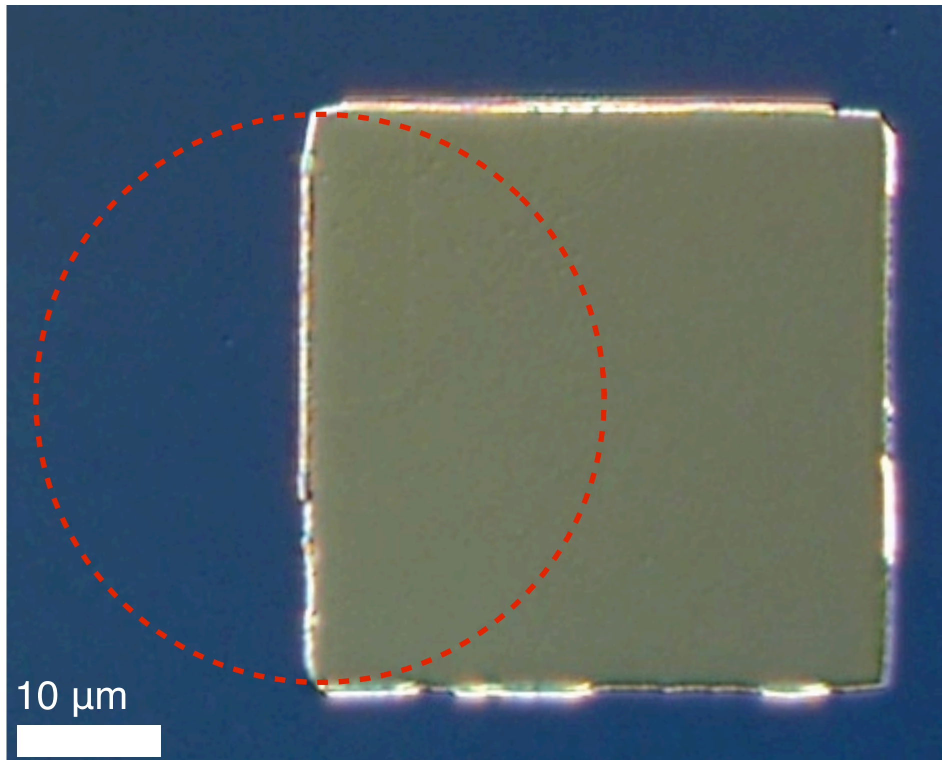

FIG. 6.3.1. A pristine Au square mesa and illustrated $\frac{1}{e^2}$ diameter of the focused laser beam.

Irradiation of a square mesa at the Si material removal threshold of 0.30 J/cm^2 is shown in Figure 6.3.2. The laser polarization is perpendicular to the mesa edge in Figure 6.3.2(a) and parallel to the edge in Figure 6.3.2(b). LIPS are seen on the Si substrate and parallel to the mesa edge in both cases.

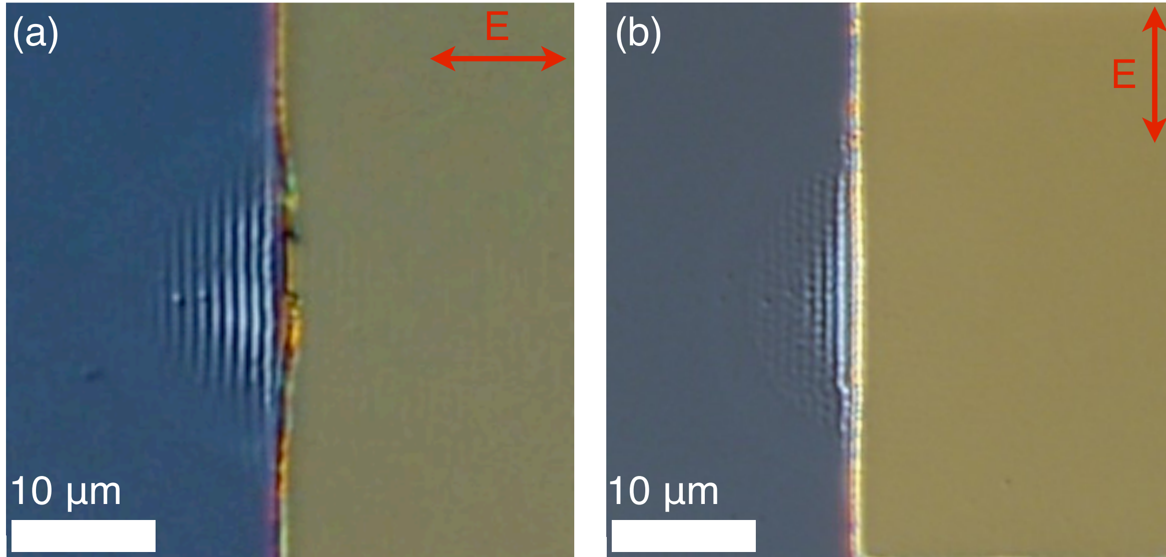

FIG. 6.3.2. Irradiation of square mesa at 0.30 J/cm². (a) Polarization vector perpendicular to mesa edge. (b) Polarization vector parallel to mesa edge.

The distributions of Λ formed near the mesa edges in Figure 6.3.2 are shown in Figure 6.3.3.

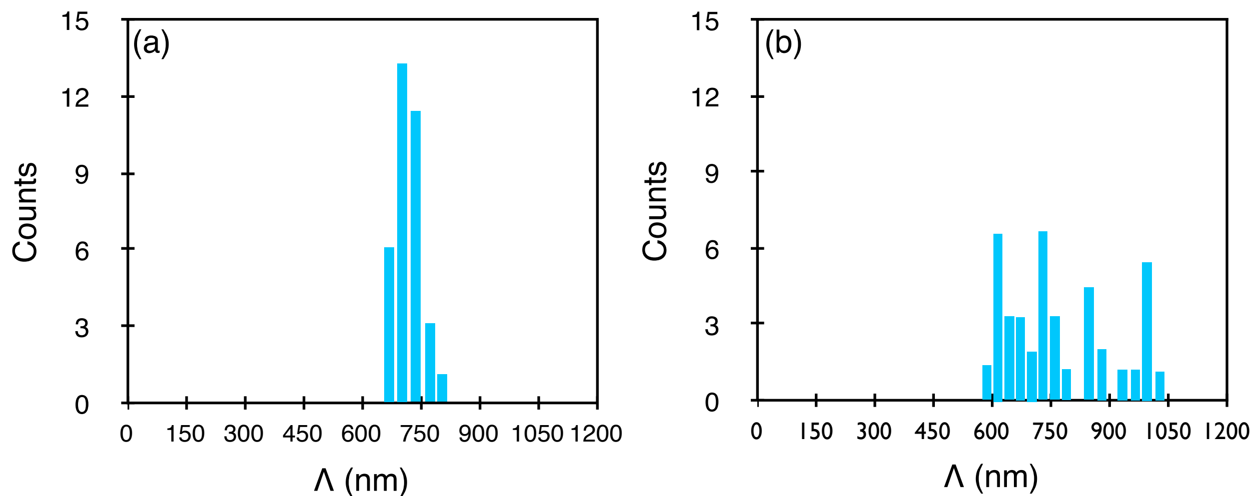

FIG. 6.3.3. Distributions of Λ after irradiation of the mesa in Figure 6.3.3. (a) Distributions for polarization perpendicular to a mesa edge. (b) Distributions for polarization parallel to a mesa edge.

The distribution of Λ for irradiation with perpendicular polarization has a large peak centered at a Λ of 705 nm ± 10 nm, while the distribution of Λ for irradiation with parallel polarization has a much larger spread of values.

If the fluence is increased to 0.64 J/cm^2, Figure 6.3.4 clearly shows that LIPS are forming on both the Au and Si surfaces.

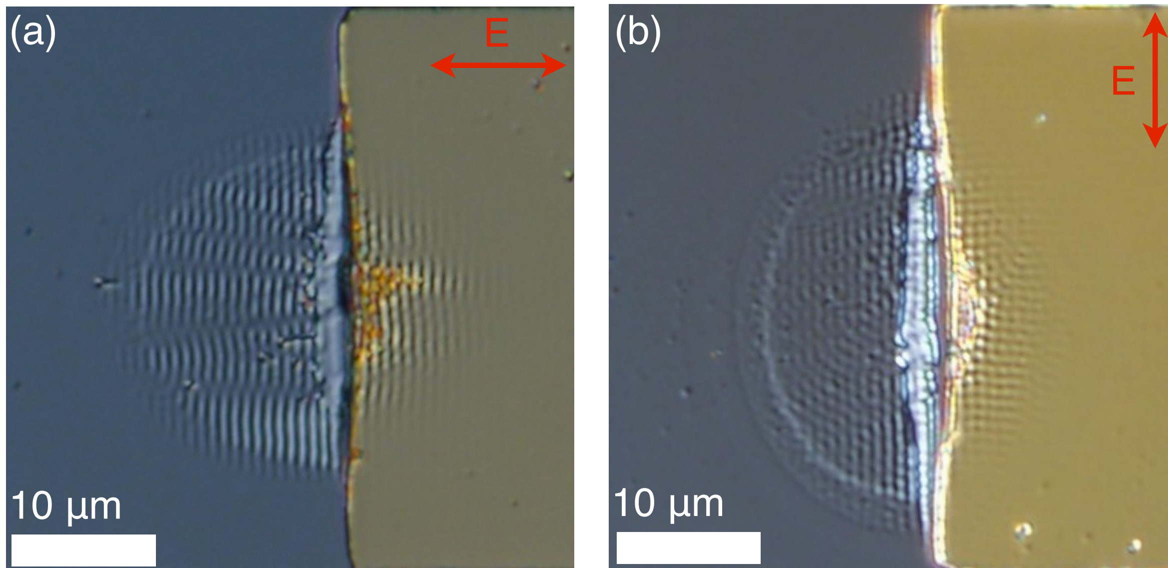

FIG. 6.3.4. Irradiation of square mesa at 0.64 J/cm^2. (a) Polarization vector perpendicular to mesa edge. (b) Polarization vector parallel to mesa edge.

It was not possible to determine the LIPS periodicity above a local fluence of 0.60 J/cm^2 since for increasing fluence, the Si surface near the mesa edge develops a large trench in the irradiated region which masks the LIPS formation in this region. The distribution of Λ for a local fluence of 0.60 J/cm^2 has a wide spread of values similar to the distribution in Figure 6.3.3(b), and is likely due to the initial LIPS pattern being distorted by the subsequent formation of the trench.

If the fluence was decreased to 0.20 J/cm^2, periodic variation in DIC contrast is visible on both the Au and Si surfaces for perpendicular polarization in Figure 6.3.5(a). If the polarization is parallel to the mesa edge at this fluence, no LIPS are visible on either the Si or Au surface, Figure 6.3.5(b).

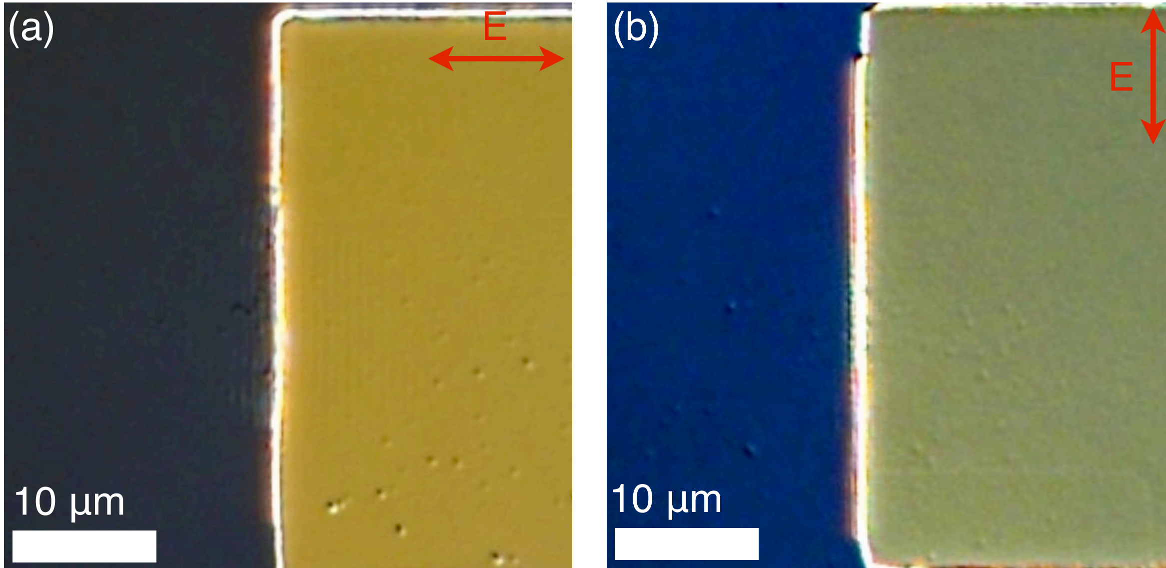

FIG. 6.3.5. Irradiation of square mesa at 0.20 J/cm^2. (a) Polarization vector perpendicular to mesa edge. (b) Polarization vector parallel to mesa edge.

An enlarged image of the LIPS from Figure 6.3.5(a) is shown in Figure 6.3.6.

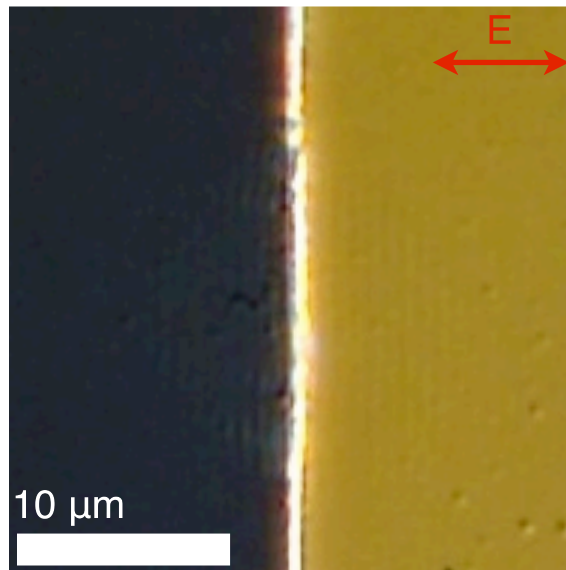

FIG. 6.3.6. Irradiation of square mesa at 0.20 J/cm^2 with the polarization vector perpendicular to the mesa edge.

At 0.20 J/cm^2 and perpendicular polarization, using AFM, height variations are seen on the Au surface, Figure 6.3.7. No height variations on the Si surface were

evident at this fluence. The height variations are typically ~ 3 nm below the original Au surface. Below 0.20 J/cm^2, no variations were observed on either the Au or Si surfaces.

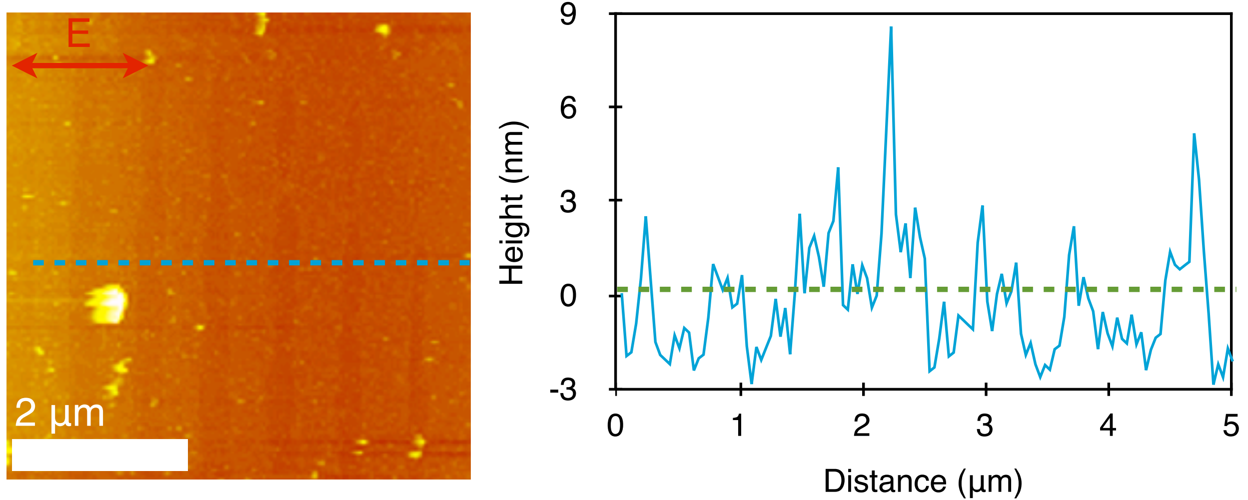

FIG. 6.3.7. AFM image of LIPS on a Au surface after irradiation of a mesa edge at 0.20 J/cm^2 and perpendicular polarization.

The dependence of LIPS orientation on the orientation of the polarization vector with mesa edges was also studied by irradiating triangular mesas. Triangles irradiated at 0.50 J/cm^2 with different polarization vector orientations are shown in Figure 6.3.8. It can be seen that the orientation of the LIPS is strongly influenced by the orientation of the polarization vector with the mesa edges.

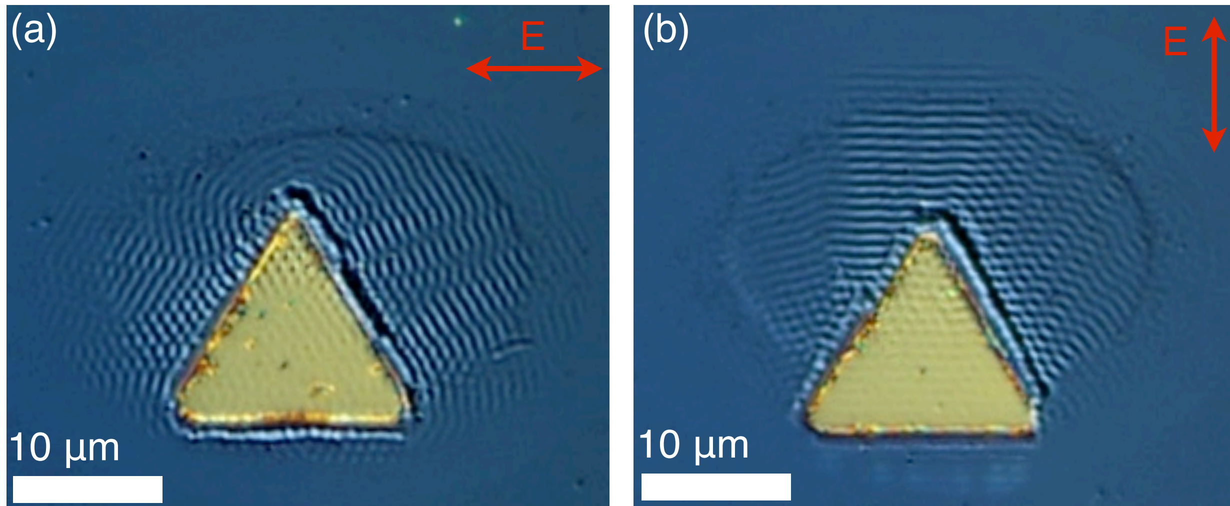

FIG. 6.3.8. Irradiation of triangular mesas at 0.50 J/cm^2. (a) Horizontal polarization. (b) Vertical polarization.

These results suggest that the edges are acting as sources for LIPS formation. It is evident in every optical image that not only is the LIPS orientation dependent on the polarization vector orientation with mesa edges, but the contrast of the LIPS is also dependent on mesa edge orientation. This fact is especially apparent as the polarization vector is rotated around the apex of the triangle in Figure 6.3.9(a) for a horizontal polarization vector. The mesa edges acting as sources are illustrated in Figure 6.3.9(b), with the horizontal polarization vector irradiation of the triangle in Figure 6.3.9(a). The sources from each edge are color coded with the LIPS which are parallel to that source.

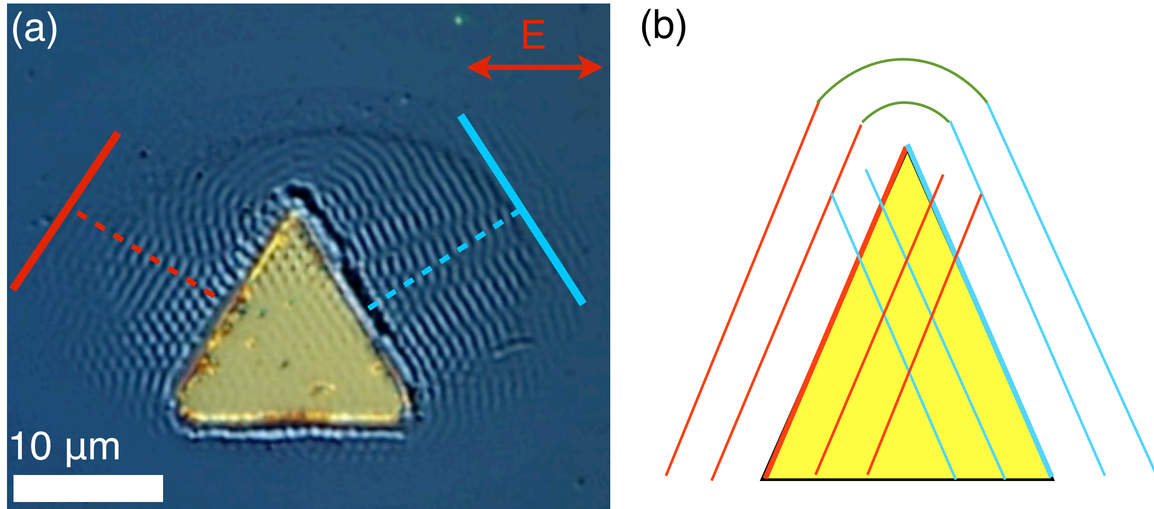

FIG. 6.3.9. (a) Irradiation of a triangle at 0.50 J/cm². (b) Illustration of sources for LIPS formation in (a).

If we assume the mesa edges are acting as sources for LIPS then it can be seen in Figure 6.3.9(b) that LIPS orientation in the Si substrate is influenced by each mesa edge, even around the apex of a triangle. The presence of multiple sources also explains the "crosshatch" pattern seen at the apex of the triangle on the Au surface formed by LIPS formation from multiple mesa edge sources. LIPS are clearly seen forming around the entire range of angles of the polarization vector with mesa edges.

Contrast in the DIC images strongly suggests that the LIPS amplitude is changing with polarization. To quantify the polarization dependence of LIPS amplitude, a square mesa was irradiated and the LIPS amplitudes were compared for polarizations perpendicular and parallel to the mesa edges, Figure 6.3.10. The dashed green line indicates the original surface.

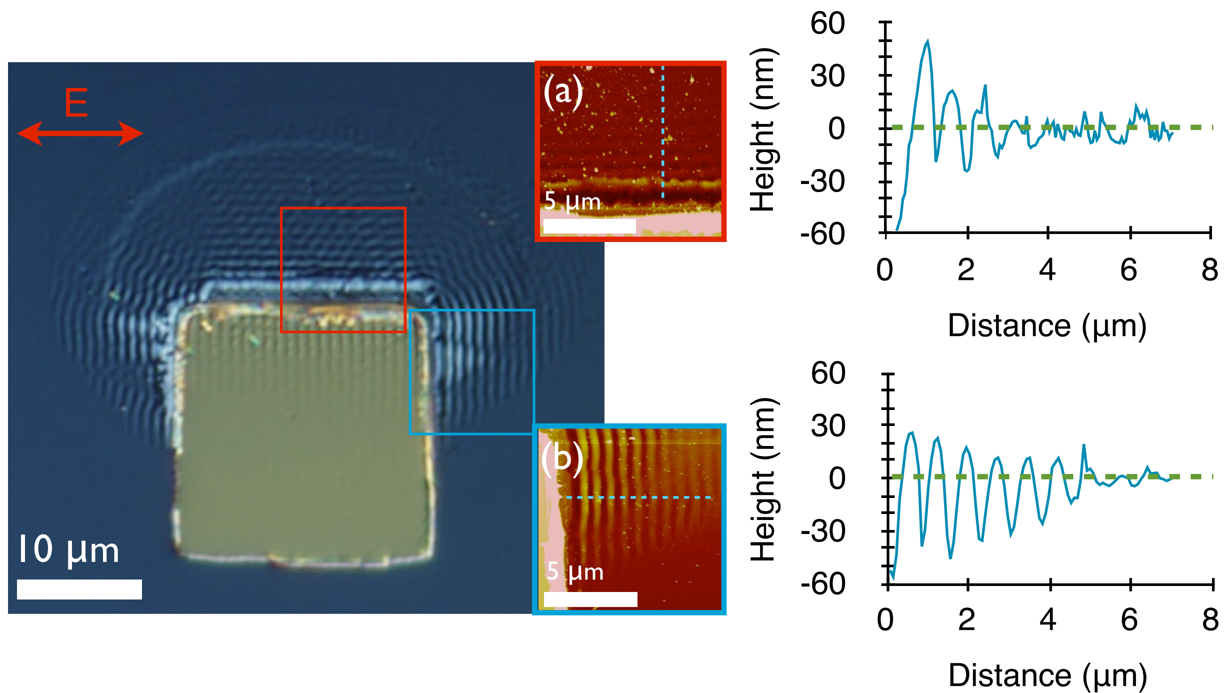

FIG. 6.3.10. DIC image of the irradiation of a square Au mesa at a peak fluence of 0.50 J/cm². a) AFM image and trace of LIPS formed in the Si at the upper edge of the square with wavevectors perpendicular to the laser polarization. b) AFM image and trace of LIPS formed with wavevectors parallel to the laser polarization. The peak-peak magnitudes of the LIPS with wavevectors parallel to the laser polarization are larger than those with wavevectors perpendicular to the polarization. Height = 0 corresponds to the original surface height.

It is clear from the AFM traces that LIPS amplitudes are smaller when the laser polarization is parallel to mesa edges. The deep valley on the left hand side of both traces, which is closest to the mesa edge, is due to trench formation at the mesa edge. Even when the local fluence in the blue box (0.34 J/cm²) is lower than the peak fluence of 0.34 J/cm² in the red box, the LIPS which form when the polarization is perpendicular to the mesa edge are deeper than LIPS for parallel irradiation. A more direct comparison of the LIPS amplitude dependence on the polarization orientation perpendicular and parallel to mesa edges is shown in Figure 6.3.11 where AFM traces are shown for the same fluence.

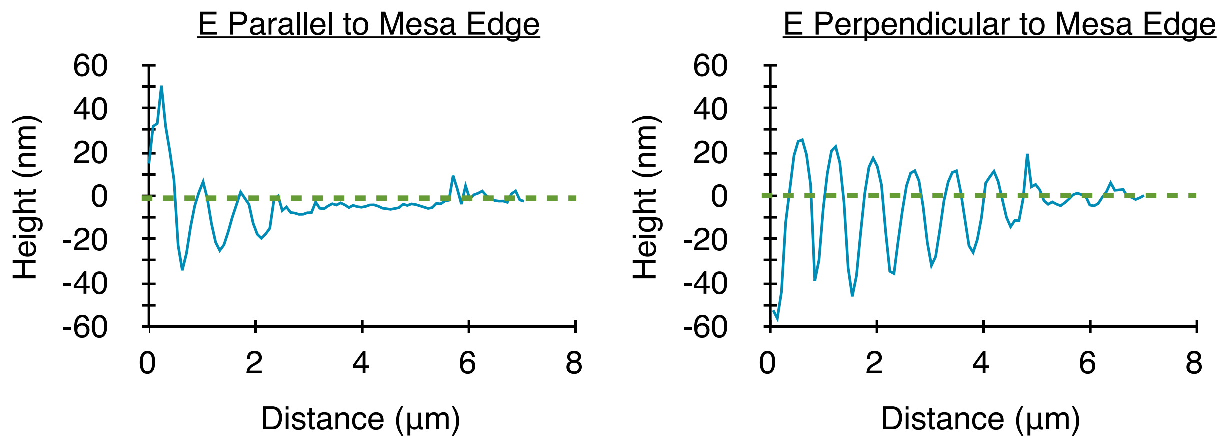

FIG. 6.3.11. Comparison of LIPS amplitudes in Si after irradiation of a Au mesa edge at 0.34 J/cm^2.

If mesa edges are not directly irradiated and the laser pulse is displaced to one side, it can be seen in Figure 6.3.12 that a crater forms in the Si substrate, while LIPS form parallel to the closest mesa edge.

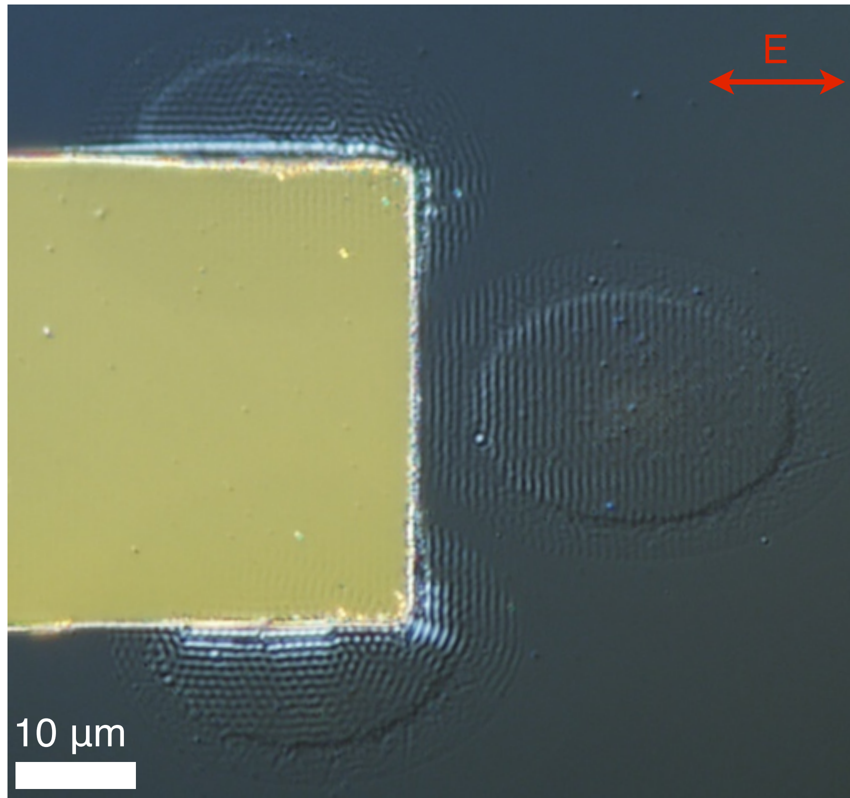

FIG. 6.3.12. Single pulse crater formation in Si at 0.75 J/cm^2 near a mesa edge.

This figure clearly shows even when a crater is formed away from mesa edges, the mesa edge is still acting as a source for LIPS formation and an initially random surface is not required for LIPS formation.

Section 6.4 Pump-Probe Microscopy of LIPS Formation

In order to determine the time scales for LIPS formation for the first time, pump-probe microscopy was used to image the formation of LIPS with a probe beam after LIPS formation was initiated with a pump beam. First, pump-probe microscopy after irradiation of a pristine Si substrate with a single pump pulse at 0.60 J/cm^2 was studied using the blue light pump-probe reflection geometry introduced in Section 3.6. The images formed by the blue light at various time steps are shown in Figure 6.4.1.

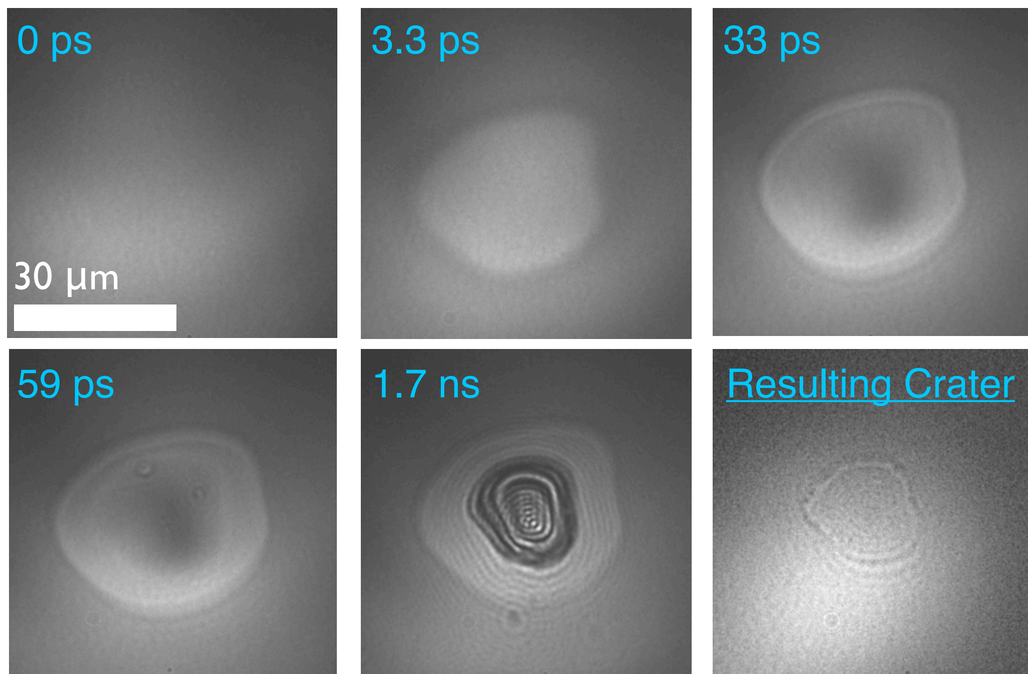

FIG. 6.4.1. Pump-probe microscopy of Si removal after irradiation with a single pulse at 0.60 J/cm^2.

At 0 ps, no features are observed in the probe image since this is before the pump pulse has irradiated the Si surface. The time at which the pump pulse irradiates the Si surface was determined to within 3.3 ps, after which the reflectivity of the Si

surface increases, due to the presence of molten Si. After 33 ps, the center of the irradiated region has darkened; this is the first evidence for the existence of an expanding dome of Si rising from the underlying Si surface [Downer 1985]. Rings are observed in the center of the irradiated region resulting from the interference of reflected light from the surface of the expanding molten dome of Si and light reflected from the remaining Si beneath the dome. After 8.3 ns, the presence of molten Si is no longer evident and the resulting crater edges after irradiation are shown in the last frame.

The pump-probe setup using blue probe light did not have the proper resolution to image LIPS with the probe light. In order to image LIPS formation, a new pump-probe microscopy setup using white probe light at normal incidence for image collection was developed. Shown in Figure 6.4.2(a), Fresnel fringes are projected onto the Si surface and LIPS are only visible with the white probe light when they are within the region illuminated with Fresnel fringes, Figure 6.4.2(b).

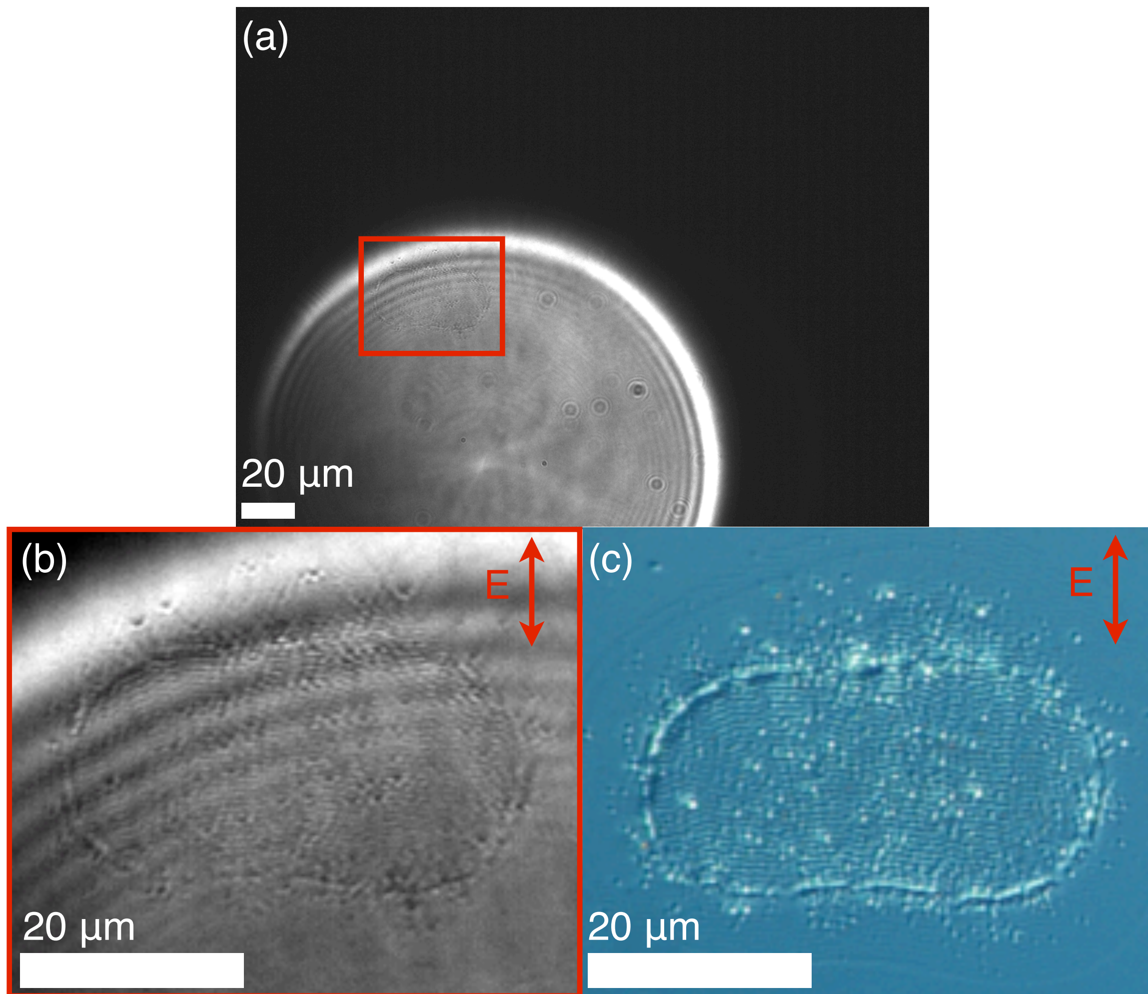

FIG. 6.4.2. Image from white probe light using the white light pump-probe setup. (a) Fresnel fringes projected onto the Si surface. (b) Imaging LIPS within the Fresnel fringes. (c) Nomarski contrast image from a commercial microscope of the same LIPS.

Initially two laser shots at 0.45 J/cm^2 were used to irradiate bulk Si, but material removal after the second laser shot masked the LIPS formation. Therefore, it was necessary to form a crater with the first shot using 0.45 J/cm^2 and then turn the laser fluence down to 0.34 J/cm^2 for the second shot. In this manner, the velocity of Si removed from the surface was slowed and LIPS formation could be observed before material removal masked the Si surface.

Figure 6.4.3 at 0 ps shows the crater formed after the first shot before the arrival of the second laser shot. The crater is elongated in the horizontal direction since the pump beam is now striking the sample at a 45° angle.

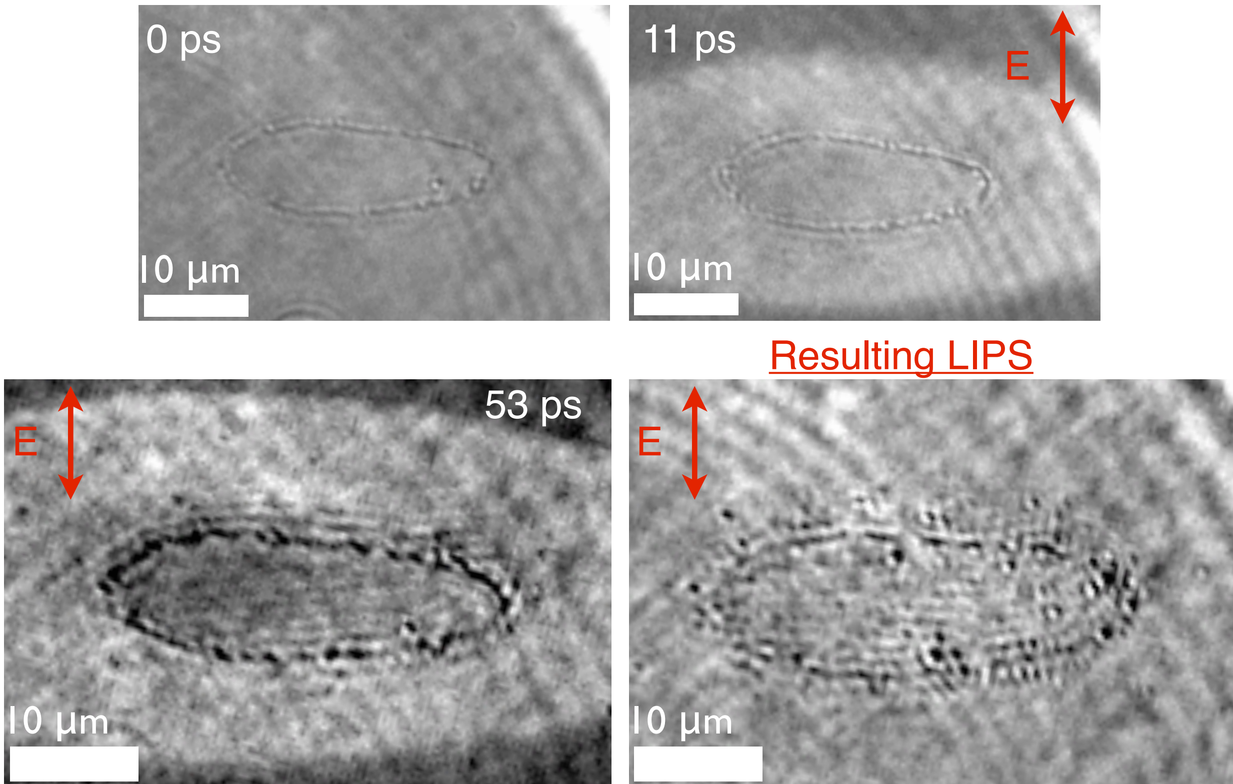

FIG. 6.4.3. Pump-probe microscopy of LIPS formation after irradiation of a crater in bulk Si with a single 0.34 J/cm^2 pulse.

Seen in Figure 6.4.3, molten Si formation is shown for 11 ps and 53 ps after irradiation, and LIPS are visible within the Si crater 53 ps ± 5 ps after arrival of the pump pulse. The crater began to darken 77 ps after arrival of the pump pulse. Since the surface is already molten before 53 ps, the LIPS contrast at 53 ps is most likely due to height contrast. The height resolution limits of the white light pump-probe microscopy setup were not determined, but they are at least on the same order as the depth of the crater in Si, ~ 20 nm. This indicates that the initiation of LIPS formation occurs on time scales which are on the order of time scales of the initiation of material removal near threshold [Downer 1985].

Section 6.5 Proposed LIPS Formation Mechanisms

LIPS formation in Si craters after two shots and also after a single shot near defects were observed in this thesis and have been observed in the literature [Bonse

2009, Bonse 2010]. However, there are several new features of LIPS formation which should be noted in the images from the previous sections in this chapter.

By irradiating Au mesa microstructures, LIPS formation was observed in Section 6.3 after irradiation of mesas after a single laser shot. This is not surprising since the mesa is essentially a surface defect, but the most interesting feature is the formation of LIPS both perpendicular and parallel to the laser polarization. In the literature, LIPS with a Λ slightly less than λ are only discussed for LIPS which form perpendicular to the laser polarization. While LIPS forming in directions parallel to the laser polarization are seen with Λ much less than λ and only after irradiation with many laser pulses [Honda 2010, Qi 2009]. It should be noted that the intensity of light diffracted by features parallel to the polarization has been calculated [Guosheng 1982], but no LIPS were observed for this polarization angle.

After irradiation of mesas, the step-edges act as sources for LIPS formation on both the Au and Si surfaces for any polarization angle w.r.t. mesa edges. Light scattered by mesa edges fills 3D space in the far-field of the edge, interferes with the incident laser light, and projects a Fresnel diffraction pattern onto the Au and Si surfaces. The formation of LIPS when the laser pulse is not centered on mesa edges, Figure 6.3.12, further shows that mesa edges act as sources for LIPS formation and a randomly rough surface is not required for LIPS formation. If no mesa edge is present, such as during the irradiation of polished Si targets far away from Au features, no diffraction from an edge occurs. The first few cycles of scattered fundamental laser light from a mesa step-edge are illustrated in Figure 6.5.1. In Figure 6.5.1(a), the presence of a step edge with a height much less than the laser wavelength (not shown to scale) scatters light in 3D space.

LIPS formation occurs around all edges, according to the Huygens-Fresnel principle, illustrated as concentric curves in Figure 6.5.1(b). With multiple edges acting as sources of LIPS, LIPS form at multiple angles, experimentally seen in Figure 6.3.9(a) by the diamond-shaped crosshatch pattern in the Au apex of the triangle and in the crosshatch pattern in the Si along the edges of the triangle, suggested by [Obara 2011]. In Figure 6.5.1(b), LIPS formation from multiple edge sources at the apex of a triangular mesa is illustrated along with the formation of the crater edge.

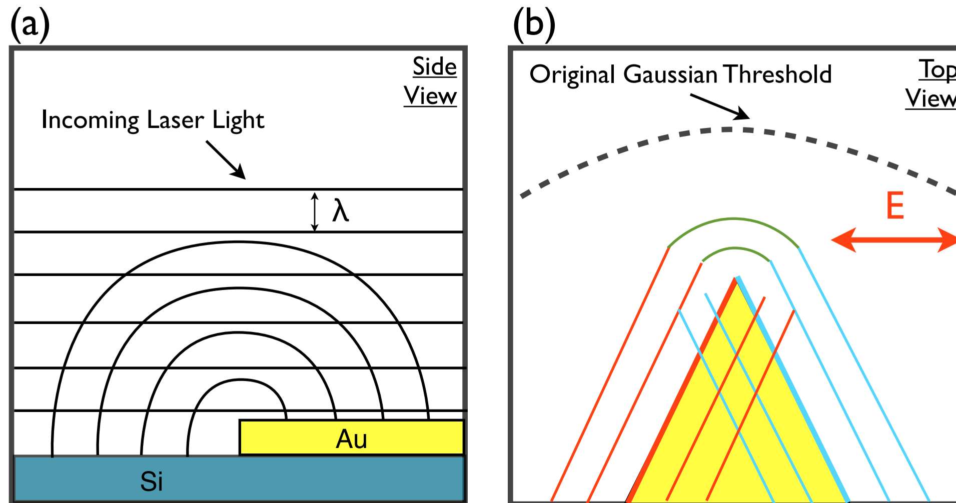

FIG. 6.5.1. The orientations of the first few fringes from diffraction of the fundamental beam from the microstructure edges are illustrated. a) Side-view of light diffraction from a step-edge. Scattering fills 3D space and interferes with the incoming laser light to form a diffraction pattern in the near-surface of the Au mesa and Si substrate. b) Top-view of diffraction from the apex of an equilateral triangle. Diffraction intensity is equal for both triangle edges (red and blue). Since the angle of the triangle edges is ~ 60°, LIPS formation from multiple edges occurs in both the Si near the edges of the triangle and on the Au mesa. Both crater and LIPS formation are seen in the Si substrate. Corners fabricated by lithography and deposition have finite size and shape and LIPS form around the corner, according to the Huygens-Fresnel principle, indicated by concentric curves in green.

The diffraction patterns projected onto Au and Si surfaces by mesa edges lead to an inhomogeneous deposition of energy onto the surface. The incident laser fluences used in these studies were above the melt threshold of Si (~ 0.20 J/cm^2) and close to the melt threshold of Au (~ 0.55 J/cm^2). The energy is absorbed by the Au and Si surfaces, and the surfaces melt within a few picoseconds (ps) [Kandyla 2007, Reis 2006]. Subsequent dynamics of the molten material and heat transfer occur after melting [Sokolowski-Tinten 1998, Kandyla 2007, Reis 2006]. The exact mechanisms of material movement and subsequent LIPS formation are unclear at this point, however it should be noted that the depths of the LIPS valleys are larger than the amplitudes of the hills above the original Si surface, Figure 6.3.10. Showing that material has been removed and LIPS formation in our experiments is likely the result of material removal. It is hypothesized that periodic energy variations in the Gaussian intensity distribution, due to superposition, over the material surface lead to variations in the temperature of the molten Si and a corrugation of the irradiated surface results from either localized material removal, vaporization, surface flow, or a contribution from each mechanism.

The flow of molten material before thermal quenching will further tailor the shape of the LIPS.

For incident laser polarizations perpendicular to mesa edges the distribution of periods in our studies is peaked at a wavelength slightly less than the fundamental laser wavelength agreeing with the results from other groups [Bonse 2009]. For incident laser polarizations parallel to mesa edges, the distributions of periods for polarizations parallel to mesa edges is not peaked at a particular wavelength and may be due to LIPS formation at multiple orientations, which introduces larger variations in the AFM measurements and FT calculations. Seen in Figure 6.3.10, for incident laser polarizations parallel to mesa edges, LIPS are mostly seen parallel to mesa edges, but LIPS are also seen at orientations which are not parallel to *any* mesa edge. This may be due to activation of mechanisms other than Huygens-Fresnel diffraction, such as SPP excitation by defects on mesa edges.

In other works, the irradiation of Au nanospheres, tuned to the Au plasmon resonance, with multiple circularly polarized laser shots below the Si single shot removal threshold resulted in circular LIPS formation surrounding the nanospheres in the neighboring Si substrate [Obara 2011]. These effects were attributed to plasmonic diffraction in the far-field of the nanospheres; however, we have shown that LIPS may form after a single laser shot and optimizing mesa dimensions for plasmon resonance is not necessary to form LIPS.

In this chapter, as the polarization vector is rotated w.r.t. mesa edges, the LIPS amplitude changes with orientation but LIPS never completely disappear. The fact that we observe LIPS even when the laser polarization is parallel to mesa edges, and LIPS are present for any angle with the mesa edge, especially apparent in Figure 6.3.9, suggests that *two* separate mechanisms are responsible for LIPS formation. The SPP excitation mechanism suggested by other groups is strongest for laser polarizations perpendicular to surface defects (p-polarization) but is prohibited for s-polarized irradiation w.r.t. surface features [Zayats 2005]. Therefore SPP excitation should not be playing a role in LIPS formation when the laser polarization is parallel to mesa edges and the Huygens-Fresnel diffraction mechanism will dominate when SPP excitation is forbidden.

Figures 6.3.10 and 6.3.11 show that the SPP excitation has a stronger intensity than the diffraction mechanism since LIPS amplitudes are larger where SPP excitation is allowed and are smaller where SPP excitation is forbidden. Calculations have shown that in the presence of randomly rough surfaces, the SPP mechanism for LIPS formation will dominate [Guosheng 1982, Sipe 1983] and LIPS will only be seen perpendicular to the laser polarization. SPP excitation is also responsible for the narrow LIPS Λ distributions for polarization vectors perpendicular to mesa edges, Figure 6.3.3(a).

The amorphous Si results from Figure 6.3.6 show that a periodic variation of laser light intensity is projected onto the Si surface. In this figure, the light intensity was too low to form LIPS but was high enough to melt the Si and form amorphous Si. The degree of Si amorphization in the periodically varying regions could not be determined, but alternating thicknesses of amorphous Si could be responsible for the contrast change. Local regions of Si which were exposed to higher laser light intensities will form thicker layers of amorphous Si than those regions exposed to lower light intensities. The thicker amorphous Si regions will be more reflective and brighter, and the thinner regions will be darker [Liu 1979].

For 0.20 J/cm^2, no LIPS were observed in AFM on the Si surface but periodic trenches were observed on the Au surface. We are forming trenches in the Au surface at incident laser intensities which are likely far below the estimated Au melt threshold (~ 0.55 J/cm^2). The incident laser intensity is below the Au melt threshold but SPP excitation can increase the local intensity above the Au melt threshold and form trenches. Periodic variations on the Si surface were only visible if the *incident* laser fluence was above the Si melt threshold. This is because SPPs cannot be excited in Si until the critical density of carriers (~ 10^{21}/cm^3) is reached after the first optical cycle of laser light. When the fluence is increased in order to reach this critical density, the Si melt threshold is exceeded. Therefore, LIPS can't form in Si below the incident fluence melt threshold of Si. At 0.30 J/cm^2 and laser polarization perpendicular to the edge, the damage region in Si is larger than expected for these fluences in bulk Si. At this fluence and polarization orientation, SPPs are excited on the Si surface [Bonse 2009] which will

periodically increase the local laser light intensities above the Si damage threshold on the Si surface and shift the periods of the LIPS below the incident laser λ.

Au is a metal with a carrier density of ~ $10^{22}/cm^3$ so when SPP excitation is allowed, depending on the polarization angle with surface features, SPP excitation is supported for laser fluences below the Au melt threshold. The excitation of SPPs then periodically increases the field intensity on the Au surface above Au's melt threshold and forms periodic trenches in the Au surface for incident laser fluences which are below the Au melt threshold. The formation of trenches in the Au surface is the first stage of LIPS formation in Au.

These results show that LIPS formation is affected by the shapes of features present on surface before irradiation by laser pulses and LIPS formation for all orientations of linearly polarized laser light with surface features is allowed. LIPS amplitudes are largest when the laser polarization is perpendicular to features, also seen by other groups [Bonse 2009, Huang 2009], but the Huygens-Fresnel diffraction mechanism allows for LIPS formation for any polarization orientation w.r.t. mesa edges. From these results it is evident that the intensity of diffracted light, and subsequently the local intensity of laser energy coupled into the surface will control the LIPS amplitude and orientation in any system.

The studies presented here have important implications for irradiation of polished surfaces with multiple laser shots and subsequent LIPS formation. Depending on the fluence, the first laser shot will form defects and/or crater edges on the surface and these features will diffract laser light after subsequent laser shots.

Factors such as the orientation of the polarization with a mesa edge and the distance from the diffracting edge have been observed to change the diffraction intensity and consequently the energy variation over a ripple period. From these results, *any* surface feature will diffract light at all angles and the strongest intensity of diffracted light exists when the laser polarization is perpendicular to the feature, if SPP excitation is allowed. For instance, above the Si crater threshold, LIPS formation when the laser polarization is perpendicular to the crater edges dominates. However, the results in this chapter show that edges will act as a source for LIPS and the shape of the crater edge will have the strongest effects on the initial orientation of the LIPS, Figure 6.2.2,

according to the Huygens-Fresnel principle. Subsequent laser shots then irradiate a corrugated surface, and grating coupling [Garrelie 2011, Bonse 2011] will have stronger effects in one direction compared to orthogonal directions, increasing the LIPS amplitude with each shot. If the peak fluence is decreased below the single shot crater threshold in bulk Si, LIPS formation is still observed [Tan 2006, Costache 2004]. Defects accumulated on a material surface after multiple shots will diffract light, and the polarization dependence of the excitation and grating coupling of the laser energy will dictate the orientation of the resulting LIPS.

For a low number of laser shots irradiating a Si surface, the reason that LIPS parallel to the Si crater edges are not present when the laser polarization is parallel to the crater edges could be due to two factors: the dominance of the SPP mechanism and a decreased Fresnel diffraction intensity for the smaller 20 nm step height compared to the 110 nm tall Au mesas. A single defect which forms LIPS, such as the defect in Figure 6.2.1(b), will form LIPS mostly perpendicular to the feature and around a certain angle, and LIPS completely disappear for parallel polarization (verified with AFM). The dimensions of the defects present on the Si surface could not be quantified but likely have height dimensions smaller than those of the mesa microstructures. Subsequently, the Fresnel diffracted light intensity is lower for crater edges and surface defects compared to the Au mesas; therefore, LIPS are only seen mostly perpendicular to the laser polarization. The reason LIPS parallel to the laser polarization dominate during microtube formation may be due to multiple reflections at the Si-SiO_2 interface enhancing the diffraction mechanism, while the presence of the SiO_2 above the Si could suppress SPP excitation [Zayats 2005].

The intensity of Huygens-Fresnel diffraction and SPP excitation are dependent on both the dimensions of irradiated features and their composition. The deep trench which forms along mesa edges after irradiation shows that field enhancement is increasing the light intensity near Au mesa edges. This field enhancement could increase the diffracted light intensity in the Si surface near Au mesas compared to light diffracted by Si crater edges, allowing for LIPS formation parallel to the laser polarization where it is not expected. After many laser shots on *any* polished surface, each laser shot will deepen the crater on the surface and increase the number of

defects. The diffracted light intensity and SPP excitation change with each subsequent laser shot. The strength of the two activated mechanisms will then control the orientation and amplitude of LIPS in *any* material system after irradiation. Varying feature dimensions and composition in order to further decouple the SPP excitation and diffraction mechanisms in order to understand their relative intensities will be a subject of future study.

It is apparent that LIPS valleys are always deeper than the hills, so for the fluence regimes explored here, material removal always accompanied LIPS formation. Pump-probe microscopy has shown the the time scales for LIPS formation, Figure 6.4.3, are comparable to the time scales for material removal after a single laser pulse in Si, Figure 6.4.1. These images reveal for the first time that LIPS with $\Lambda \sim \lambda$ form on the same time scales as expansion of the molten material during Si removal, establishing that LIPS form as material is removed from the Si substrate. Light diffraction and SPP excitation by mesa edges lead to an inhomogeneous deposition of energy onto the Au and Si surfaces. The energy is absorbed by the near-surface of the Au and Si, and the surface melts within a few picoseconds (ps) [Reis 2006]. Above, it was hypothesized above that periodic energy variations over the material surface lead to variations in the temperature of the molten Si and a corrugation of the irradiated surface results after the initiation of material removal. If the light intensity is not high enough, the surface periodically melts, as in Figure 6.3.6, but the expansion rate of the molten material is not high enough to remove material and form a corrugated surface.

In conclusion, the irradiation of Au mesa microstructures with a single ultrafast laser pulse resulted in the formation of LIPS on isolated Au microstructures of various shapes and the surrounding Si surfaces. LIPS formation on Si and Au surfaces was found to be polarization dependent, where LIPS with the largest amplitudes formed when the laser polarization was perpendicular to a mesa edge. These results agree with previous works which have found a preference of LIPS formation perpendicular to the laser polarization direction; however, the results in this chapter suggest a second mechanism, Huygens-Fresnel diffraction, is playing a role in LIPS formation. Fresnel

diffraction from surface features leads to LIPS formation for all laser polarization orientations with feature edges after a single laser shot.

This model for LIPS formation after a single shot can be extended to LIPS formation after multiple shots in bulk substrates, where the crater edges from the first shot may act as edge sources for LIPS formation within the crater after subsequent laser shots. Defects formed after irradiation by multiple pulses at fluences below the crater threshold may also be responsible for LIPS formation. Further studies will focus on exploring the polarization dependence of the Huygens-Fresnel diffraction mechanism and SPP excitation and their dependence on the material type, height of the mesa step-edge, and number of laser shots.

Finally pump-probe microscopy has for the first time established a time scale for LIPS formation. LIPS formation occurs on the same time scales as material removal, strongly suggesting that expansion of the molten material after absorption of laser light is responsible for the initial formation of LIPS.

References

J. Bonse and J. Krüger, *Pulse number dependence of laser-induced periodic surface structures for femtosecond laser irradiation of silicon*, Journal of Applied Physics **108**, 034903 (2010).

J. Bonse, A. Rosenfeld, J. Krüger, *On the role of surface plasmon polaritons in the formation of laser-induced periodic surface structures upon irradiation of silicon by femtosecond laser pulses*, Journal of Applied Physics **106**, 104910 (2009).

G. E. Cook, *Pulse compression - Key to more efficient radar transmission*, Ieee Proceedings of the Institute of Radio Engineers **48**, 310 (1960).

F. Costache, S. Kouteva-Arguirova, and J. Reif, *Sub-damage-threshold femtosecond laser ablation from crystalline Si: surface nanostructures and phase transformation*, Applied Physics A **79**, 1429 (2004).

T. H. R. Crawford and H. K. Haugen, *Sub-wavelength surface structures on silicon irradiated by femtosecond laser pulses at 1300 and 2100 nm wavelengths,* Applied Surface Science **253**, 4970 (2007).

M. C. Downer, R. L. Fork, and C. V. Shank, *Femtosecond imaging of melting and evaporation at a photoexcited silicon surface*, Journal of the Optical Society of America B **2**, 595 (1985).

D. Dufft, A. Rosenfeld, S. K. Das, R. Grunwald, and J. Bonse, *Femtosecond laser-induced periodic surface structures revisited: A comparative study on ZnO*, Journal of Applied Physics **105**, 034908 (2009).

Z. Guosheng, P. M. Fauchet, and A. E. Siegman, *Growth of spontaneous periodic surface structures on solids during laser illumination*, Physical Review B **26**, 5366 (1982).

H. Honda, M. Tsukamoto, N. Abe, T. Shinonaga, & M. Fujita (2010). *Microstructres formed on stainless steel by femtosecond laser irradiation*. Online: Wiley Online Library.

J. Kneipp, H. Kneipp, and K. Kneipp, *SERS - a single-molecule and nanoscale tool for bioanalytics*, Chemical Society Reviews **37**, 1052 (2008).

P. L. Liu, R. Yen, N. Bloembergen, R.T. Hodson, *Picosecond laser-induced melting and resolidification morphology on Si*, Applied Physics Letters **34**, 864 (1979).

G. Obara, N. Maeda, T. Miyanishi, M. Terakawa, N. N. Nedyalkov, and M. Obara, *Plasmonic and Mie scattering control of far-field interference for regular ripple formation on various material substrates*, Optics Express **19**, 20 (2011).

E. Ozbay, *Plasmonics: Merging photonics and electronics at nanoscale dimensions*, Science **311**, 189 (2006).

L. Qi, K. Nishii, and Y. Namba, *Regular subwavelength surface structures induced by femtosecond laser pulses on stainless steel*, Optics Letters **34**, 1846 (2009).

D. A. Reis, K. J. Gaffney, G. H. Gilmer, and B. Torralva, *Ultrafast dynamics of laser excited solids*, Materials Research Society Bulletin **31**, 601 (2006).

J. E. Sipe, J. F. Young, H. M. van Driel, *Laser-induced periodic surface structure. I. Theory*, Physical Review B **27**, 2 (1983).

D. Strickland and G. Mourou, *Compression of amplified chirped optical pulses*, Optics Communications **56**, 219 (1985).

A. V. Zayats, I. I. Smolyaninov, A. A. Maradudin, *Nano-optics of surface plasmon polaritons*, Physics Reports **408**, 131 (2005).

Chapter 7
Ultrafast Laser Interactions with Carbon

The ultrafast irradiation of polymers, CNTs, and CNT-polymer composites is studied in this chapter. First, the fs laser interaction with a bulk sample of the polymer Nafion^{TM} are presented. Nafion is used in fuel cells as a proton conduction membrane and the proton conductivity may be enhanced with Pt catalyst nanoparticles, but the NPs are only useful to facilitate charge transfer at the Nafion *surface*. Therefore, rough surfaces of Nafion are desired for enhanced catalyst utilization. Several techniques to roughen the Nafion surface have included mechanical roughening [Lehmani 1998], ion bombardment [Cho 2006], and plasma etching [Bae 2006]. But these techniques either provide little control over the Nafion surface roughness or they change the chemical properties of the polymer, rendering it useless for proton conduction. It will be shown in this chapter that the Nafion surface may be roughened using void nucleation and growth after irradiation without detrimentally affecting the conductivity of the polymer. Irradiation of CNT forests are then presented and it will be shown that alignment of the top layer of the forest may be accomplished using irradiation with a single laser pulse.

Finally the results of a combined CNT-polymer composite system are discussed. CNT-polymer composites have unique mechanical and electrical properties which make them ideal for use in several applications such as organic photovoltaics and microelectromechanical systems (MEMS) [Barnes 2010, Rowell 2006, Shim 2007, Bai 2012]. SWNTs aligned in the Z-direction are desirable [Bai 2012], exemplified by photovoltaic elements, flexible electronics, sensors, as well as neural prosthetic devices [Jan 2011, Gheith 2005, Kotov 2009]. However, alignment only in the Z-direction reduces the tensile mechanical properties of the composites. Therefore, it is desirable to achieve two alignment modes of SWNTs; orthogonal dual alignments of the same SWNTs in both the XY- and Z-directions. Such dual mode alignment of CNTs on a

substrate has not been achieved by any current growth techniques, where alignment is limited to CNTs standing up or lying down on the substrate. The most common alignment method involves chemical vapor deposition growth from catalyst particles, with CNTs preferentially aligned perpendicular to a substrate [Sinnott 2001]. While alignment of CNTs parallel to a substrate can be achieved using growth along the surface [Orofeo 2009], electromagnetic fields [Zhang 2001], gas flow [Shim 2005], laser ablation [Kocabas 2004], and a variety of other methods including LBL assembly [Mamedov 2002] and spin casting [Ago 1999]. This chapter demonstrates that by using ultrafast irradiation, CNT bundling and alignment both horizontal and perpendicular to the substrate was achieved using ultrafast laser irradiation under ambient conditions. It will be shown that thermal expansion of the polymer pulls CNTs out of the XY plane. Ultrafast irradiation can alter the morphology of these networks through rapid melting and subsequent quenching with no decrease in film performance. Laser processing of CNT-polymer composite films under ambient conditions opens the door for roll-to-roll processing of films after growth and deposition, obviating the need to alter current growth technologies [Kocabas 2004, Guo 2008, Kramberger 2005, Romero 2005, Mahjouri-Samani 2009]. Importantly, laser treatment in this fashion allows for the fast patterning of these films.

Section 7.1 Ultrafast Laser Irradiation of Bulk Polymer

Nafion samples were prepared at Carnegie Mellon University and were kept in water until irradiation to prevent changes in the polymer structure over time. Prior to laser irradiation, the samples were dried by placing them in low vacuum for two hours to avoid interactions of the fs irradiation with water, which may complicate interpretation of the results. Results of irradiation of the Nafion with a single laser pulse at 2.2 J/cm^2 are shown in Figure 7.1.1.

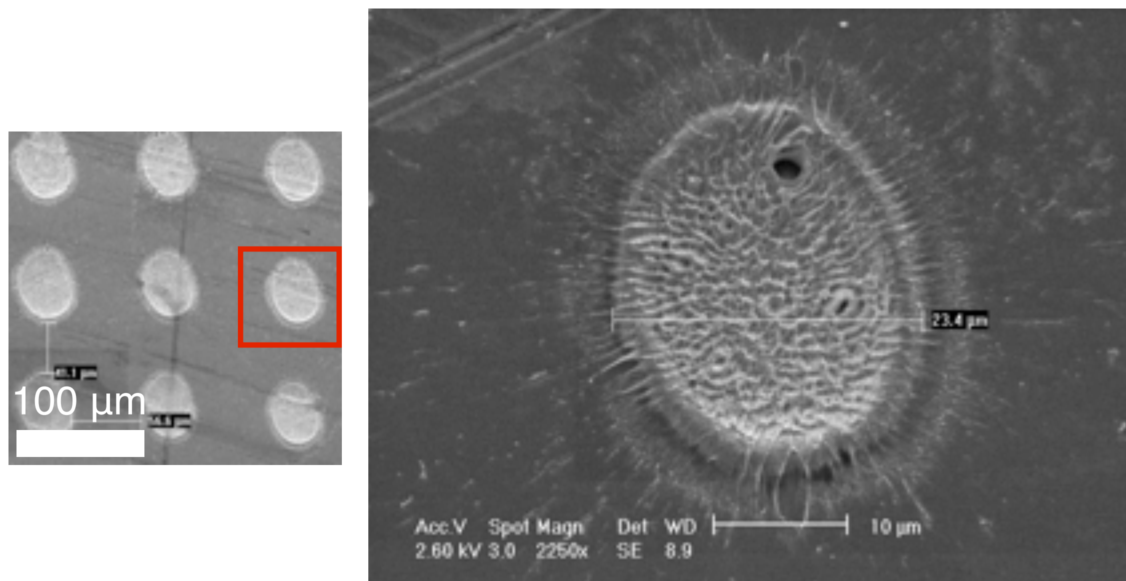

FIG 7.1.1. Irradiation of Nafion with a single laser shot.

It can be seen that the Nafion surface was drastically changed within the laser irradiated region and is very rough. The increased surface roughness, compared to irradiation near the removal threshold of metals and semiconductors, is likely the result of bond breaking, thermal expansion, and removal of the some of the polymer. While the remaining polymer also thermally expanded, was pulled out of the plane during expansion, and thermal quenching occurred before the polymer was removed from the system.

If two laser shots at the same fluence are overlapped, then the polymer surface within the overlap region is very different than the surface where only a single shot irradiated the sample, Figure 7.1.2.

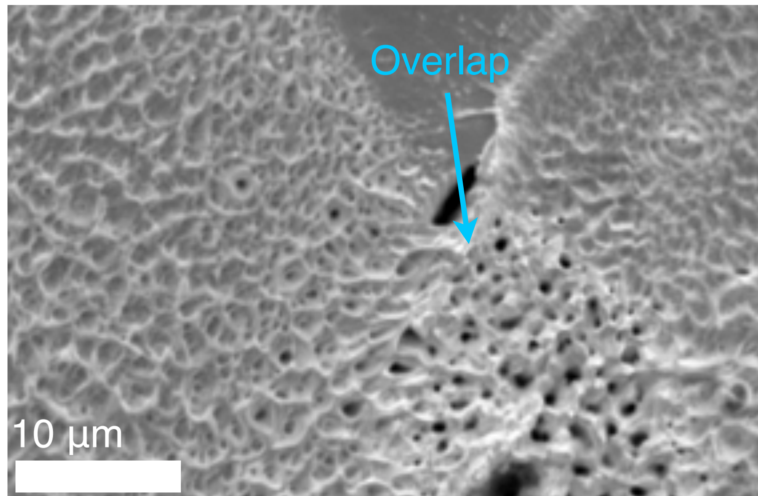

FIG 7.1.2. Irradiation of Nafion with two slightly overlapping laser shots.

Evidence of pitting within the overlap region is seen in Figure 7.1.2. If laser shots are overlapped by 50% over larger areas of the Nafion surface, then dramatic increases in surface roughness are apparent in Figure 7.1.3.

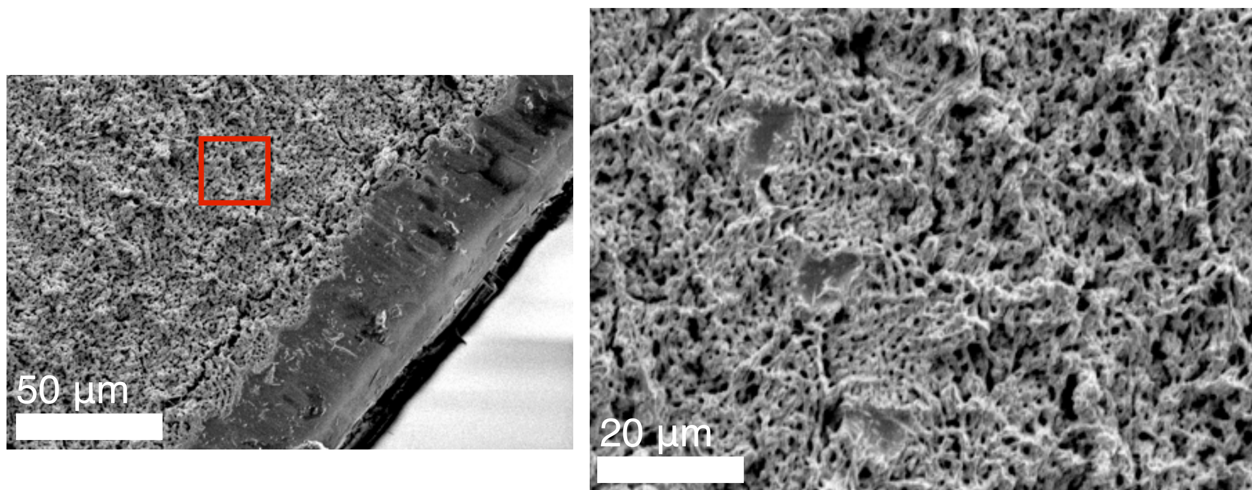

FIG 7.1.3. Large area irradiation of Nafion with 50% overlapping laser shots.

The Nafion surface now resembles an open-cell foam and, by using the sample in Figure 7.1.3, fuel cell efficiency was increased by up to 300% [Whitacre 2009]. This indicates that the Nafion chemistry was unaffected by fs laser irradiation and Pt utilization was enhanced by the increased polymer surface area. The mechanisms proposed for foam formation are the result of void nucleation within the expanding,

heated Nafion surface. After irradiation, once secondary bonds are broken, thermal expansion pulls the Nafion out of the original plane of the surface. Thermal quenching “freezes” the polymer surface and produces rough surfaces. This process likely forms a large amount of voids beneath the rough surface. The second laser shot sees a rough surface, which may redistribute the laser light, but once the bonds are broken again by the second laser shot, areas which contained voids will grow faster than regions without voids. This inhomogeneous expansion rate is ultimately responsible for the very rough surfaces seen in Figure 7.1.3, and this process is illustrated in Figure 7.1.4.

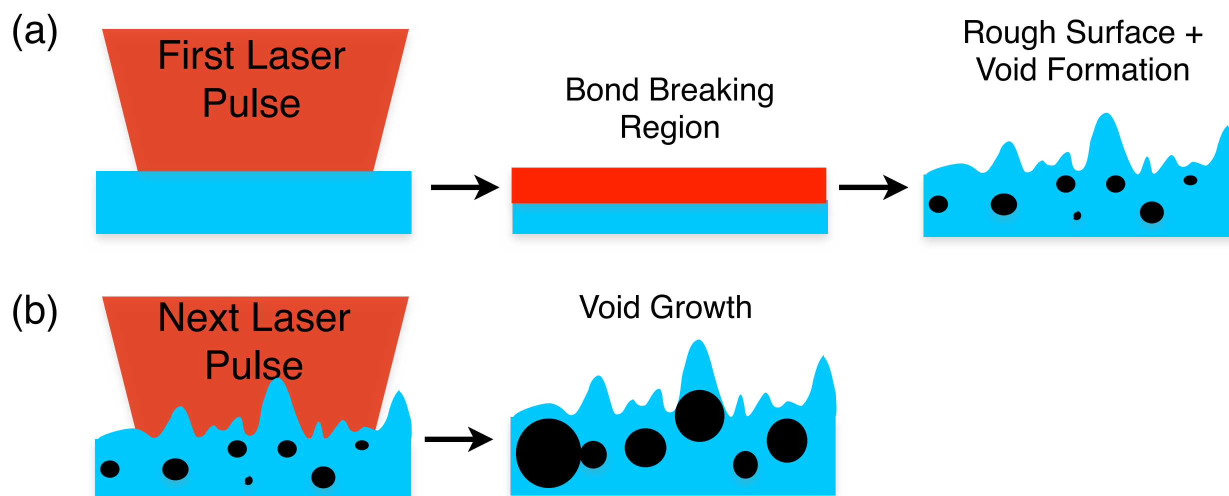

FIG 7.1.4. (a) Void formation in Nafion after a single laser shot. (b) Void growth and foam formation after subsequent laser shots.

Section 7.2 Ultrafast Laser Irradiation of CNT Forests

CNT forests were grown in the Hart lab at the University of Michigan using a CVD growth chamber, and the final forest height was measured with SEM to be ~ 500 μm. The CNTs are vertically aligned on a Si substrate and are connected together with van der Waal’s bonding in a network termed a “forest” [Bedewy 2009]. As the forest grows during CVD, a tangled network of CNTs develops at the top of the forest, the “crust”, while the CNTs underneath are vertically aligned.

A top-down view of the forest after irradiation with single laser pulses with varying fluences is shown in Figure 7.2.1.

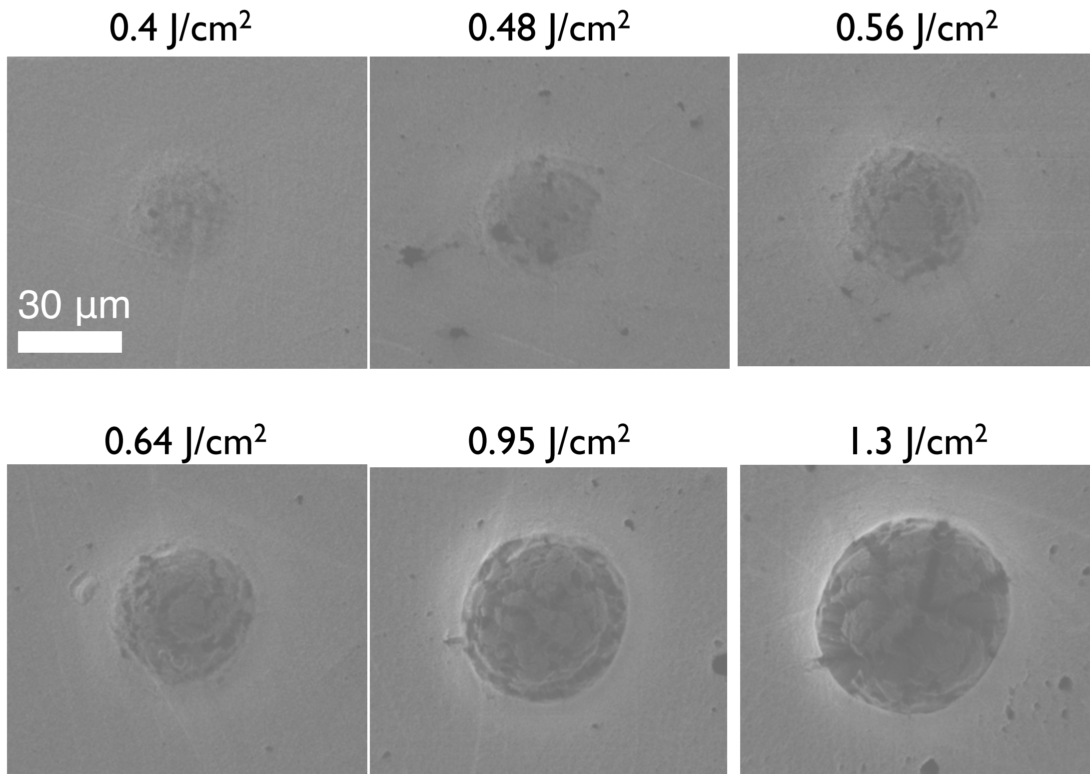

FIG 7.2.1. Top-down view of irradiation of a CNT forest with single laser pulses.

The damage threshold of the CNT forest was found to be 0.11 J/cm^2. The morphology visible in the SEM images may be the result of CNT removal from the system, but the amount of CNT removal could not be determined. At fluences below the 0.48 J/cm^2 fragmentation threshold [Guo 2008, Dumitrica 2006], the local density of the forest changed in the irradiated regions and could have occurred without CNT removal through absorption of the laser light by the CNTs, breaking of van der Waal's bonds, and thermal expansion of the collective CNT network. Further evidence for this process is shown in Figure 7.2.2 where slightly above the damage threshold of the CNT network, vertically aligned CNTs are visible within the damage region where a tangled crust is normally visible before irradiation.

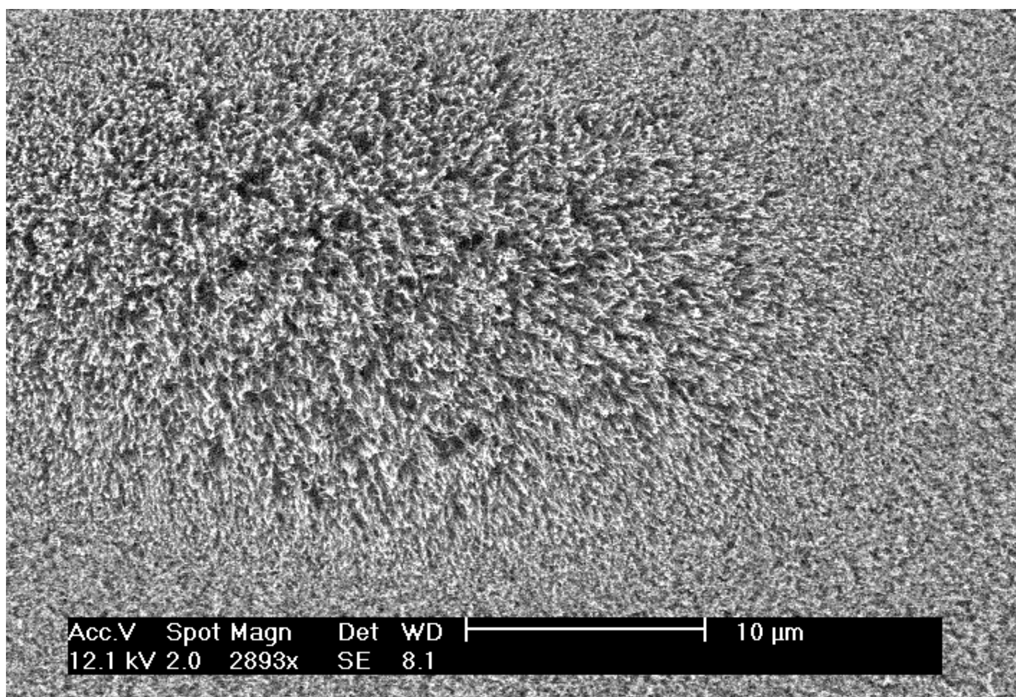

FIG 7.2.2. Top-down view of crust removal from a CNT forest. Vertically aligned CNTs are visible within the irradiated region.

This indicates that a single laser pulse removed the tangled crust from the top of the CNT forest, likely through separation of the tangled CNTs from the forest at the crust-forest interface. Alignment of CNTs with fs laser pulses will be explored further in the following section through irradiation of CNT-polymer composites.

Section 7.3 Ultrafast Laser Irradiation of CNT-Polymer Composites

CNT-polymer composites were formed by dipping microscope glass slides in a 0.05 wt % SWNT (~ 2 µm long) and 0.2 wt % poly(sodium 4-styrene-sulfonate) (PSS) dispersion with alternating dips in poly(vinyl alcohol) (PVA). This process was repeated 30 times to form a composite film ~ 120 nm thick.

Direct-write large scale patterning of the composite film was performed by rastering the laser over the film using laser fluences above the film's damage threshold, shown in Fig. 7.3.1. Each circular damage region is formed using a single pulse.

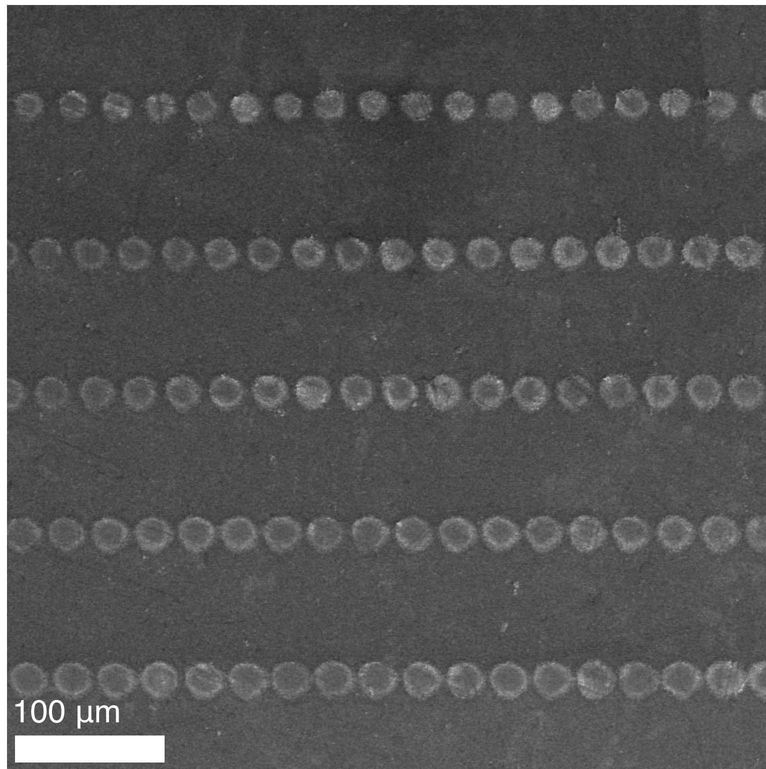

FIG 7.3.1. SEM image of the direct-write large scale patterning of a 30 layer CNT-polymer composite film on a glass substrate irradiated with varying laser fluences above the damage threshold of the film. Each row is patterned using a different fluence (increasing fluence from top to bottom), and each circular damage region is formed using a single pulse.

Increasing the laser fluence increases the size of the damage region, and individual damage spots were investigated optically to determine the damage radius of the film after single laser shots. The visible damage threshold of the CNT-polymer composite film was found to be 0.10 J/cm^2. If the fluence is increased to approximately twice the damage threshold, optical contrast shows evidence of complete removal of the film from the center of the crater.

SEM images of regions irradiated near the damage threshold in Fig. 7.3.2 show changes to the original film; a CNT-polymer foam was created. Damage is produced in the composite film when the CNTs are separated from the substrate but are not removed from the system. Structures formed by the laser irradiation are seen on multiple scales and are revealed to be bundles of CNTs in Fig. 7.3.2(b). These bundles are formed from long, parallel strands of CNTs and are pulled out of the plane of the film towards the Z-direction. The patterned CNT bundles separated from the substrate are

oriented out of the plane with angles ranging from 0° to 90° w.r.t. the XY plane, and their roots are anchored and oriented within the XY plane of the film.

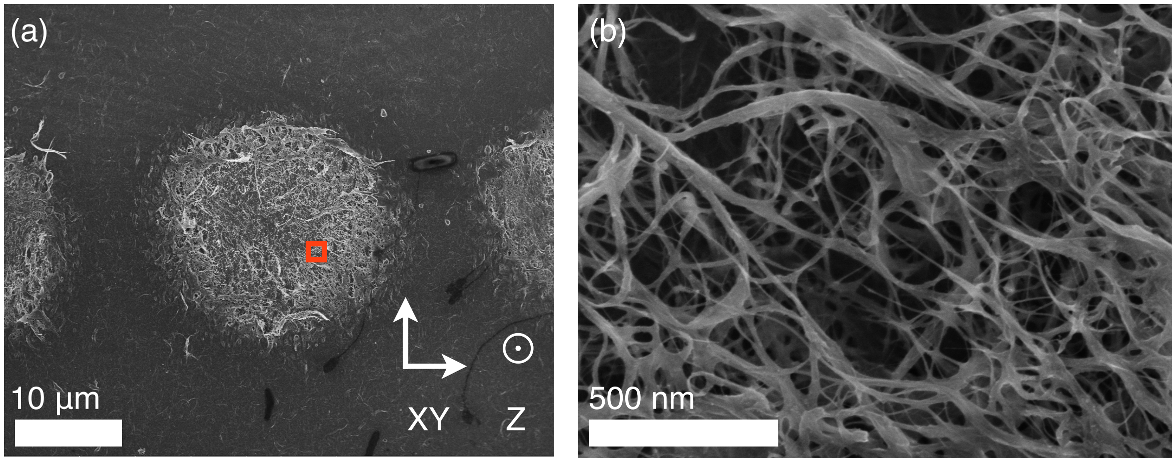

FIG 7.3.2. (a) SEM image of a single laser pulse damage area of a 30 layer CNT-polymer composite film on a glass substrate irradiated at a fluence of 0.12 J/cm^2. (b) Inset from Figure 2(a). Bundles of CNTs can be seen on multiples scales within the damage region. The XY- and Z-directions are indicated in Fig. 7.1.2(a).

Further investigation of the bundled structures was carried out using HRTEM, shown in Fig. 7.3.3. A monolayer of the CNT composite film was deposited onto a holey carbon TEM grid and irradiated at the damage threshold. The low fluence region in the top portion of Fig. 7.3.3(a) shows bundles of SWNTs crossing the holey carbon grid and each other at high-contact angles. The high fluence region in Fig. 7.3.3(a) is in the lower portion of the image and shows bundled CNT structures pointing towards this region. Two bundles of CNTs in the damage region are shown in Fig. 7.3.3(b) and are crossing each other at low-contact angle with little difference between the as-received and irradiated bundles.

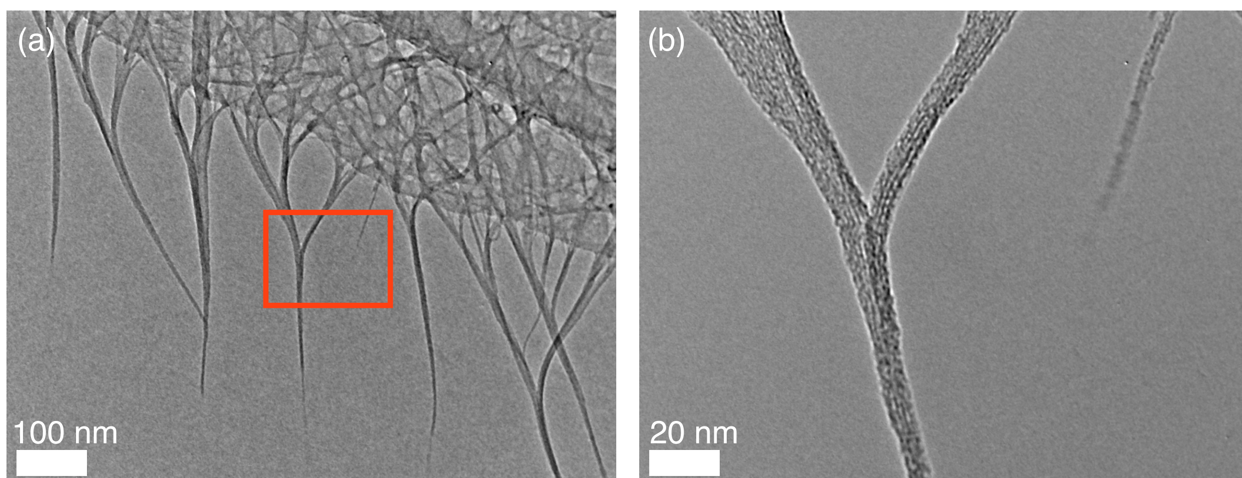

FIG 7.3.3. (a) Irradiation of a composite film at the damage threshold. CNT structures are pointing towards higher flunce regions in the lower portion of the image. (b) Inset from Fig. 3(a). Two CNT bundles within the irradiated region crossing at low-contact angle.

In order to directly determine the effects of laser irradiation on the electronic properties of the composite film, a 5 x 5 mm area of the as-received 30 bilayer film on glass was irradiated by patterning the entire film using laser pulses at a fluences of 0.12 J/cm^2. At this fluence, a CNT foam was created and CNTs were bundled while removing little material. The resistance of these films was measured before and after irradiation using copper contact pads and, most interestingly, an average resistance decrease of 20% was seen after irradiation. This decrease is less than that seen after thermal annealing [Shim 2007], but is still remarkable considering a significant number of CNTs are now standing up instead of lying down and were not expected to contribute greatly to charge transfer in the XY plane. However, considering the interconnectivity of CNTs in bundles and their tight contact, some charge transport through laser patterned areas is possible. Therefore, the net conductivity due to out-of-plane alignment is not decreasing, but rather increasing after laser patterning.

The transmittance of light in the wavelength range from 390 nm to 1100 nm was also seen to increase by an average of 18% after irradiation, shown in Fig 7.3.4. If the fluence was increased to 0.20 J/cm^2, the transmittance increased by an average of 52% but the resistance also increased by 12%.

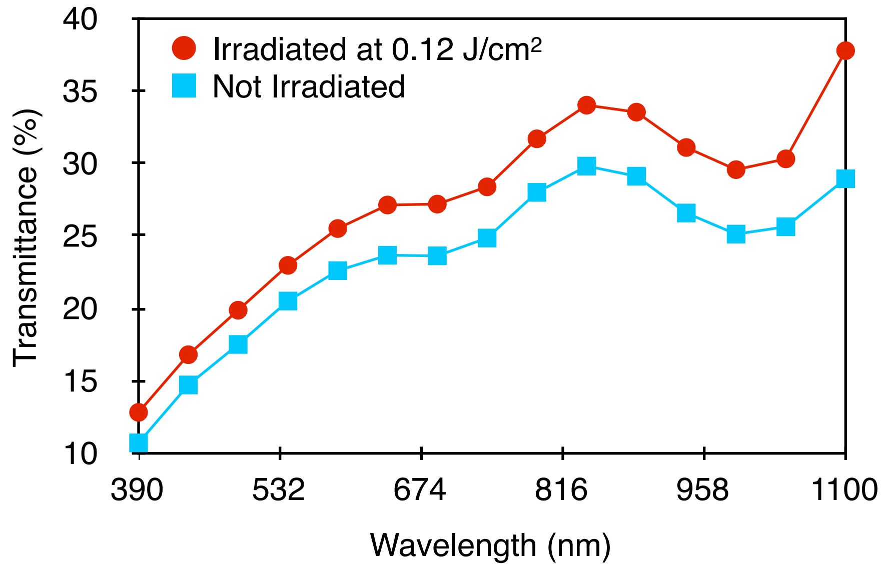

FIG 7.3.4. UV-Vis transmittance measurements of a composite film before and after laser irradiation at a fluence of 0.12 J/cm^2. The transmittance of 390 nm to 1100 nm wavelength light increased by an average of 18% after irradiation.

If a 10 bi-layer sample is irradiated with fs laser pulses at 0.11 J/cm^2, the resistance is the same as before irradiation or increased, indicating that a significantly lower amount of CNT bundles have formed. The SEM image in Figure 7.3.5 shows single pulse irradiation of a 10 bi-layer CNT-composite film at 0.11 J/cm^2 and the formation of a lower density of bundles compared to Figure 7.3.2.

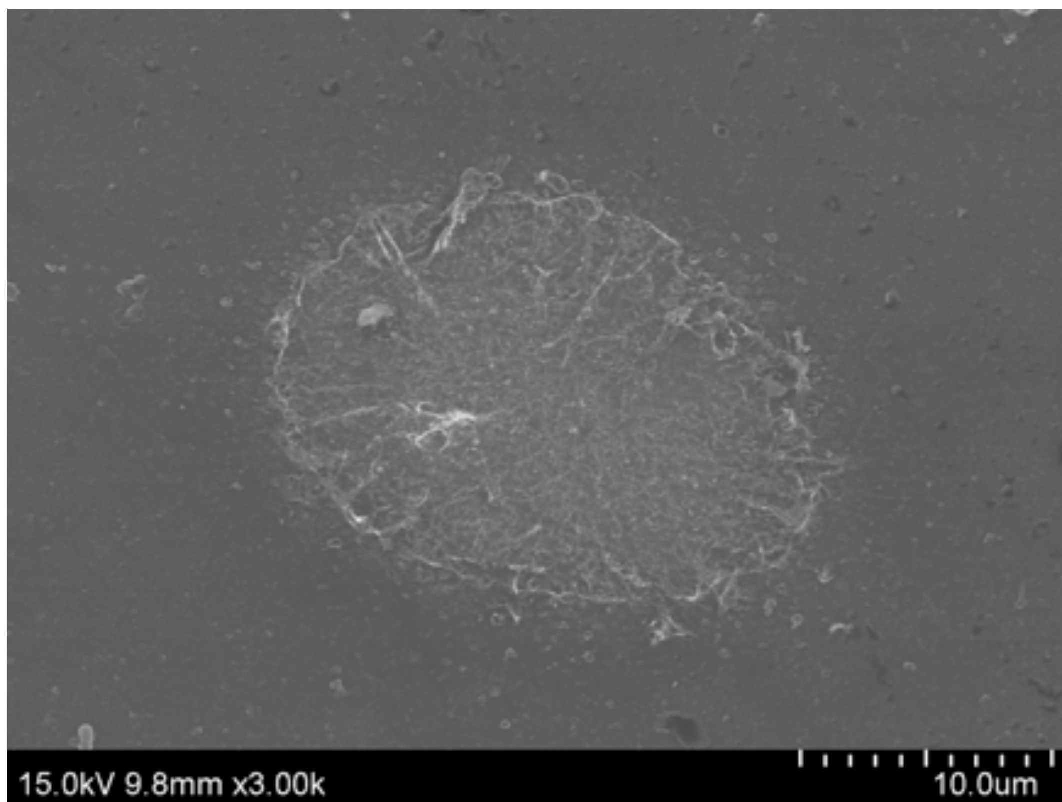

FIG 7.3.5. Single pulse irradiation of a 10 bi-layer sample at 0.11 J/cm^2.

Femtosecond laser irradiation of solids near the damage threshold is a deterministic process, involving the rapid heating and melting of material within a few picoseconds accompanied by high expansion rates of hot material in the liquid state [Sokolowski-Tinten 1998, Reis 2006, Kandyla 2007, Leveugle 2004]. The damage threshold of the CNT-polymer film was found to be an order of magnitude lower than the damage threshold of SiO_2 [McDonald 2006] and lower than the 0.48 J/cm^2 threshold to break CNT covalent bonds [Guo 2008, Dumitrica 2006]. In our studies using fluences of 0.12 J/cm^2, alignment of the CNTs within the CNT-polymer film after irradiation at the film damage threshold was seen, rather than a significant amount of CNT removal. This alignment can be seen on multiple scales between varying numbers of CNT bundles in Fig. 7.3.2 and Fig. 7.3.3 and involves the decrease of contact angles between bundles within close proximity of each other and the formation of bonds between CNTs, likely van der Waals bonds. A model was developed to explain this alignment and the formation of bonds between bundles after laser irradiation.

When a single laser pulse is incident on the CNT-polymer film, the laser light is absorbed by the CNTs and polymer. The laser turns off after 150 fs, the excited electrons relax and heat the film within a few picoseconds. Since the laser fluence is too low to break covalent bonds in the CNTs, subsequent thermal vibrations likely break secondary bonds such as van der Waals bonds between the polymer matrix and CNTs, van der Waals bonds between bundled CNTs, charge-transfer complexes between PSS and PVA, and possible chemical bonds at the polymer/CNT interface [Shim 2007].

Once the secondary bonds are broken, viscous flow in the composite film can occur at high strain rates. At high temperatures the thermal expansion coefficients for polymers can be greater than those of CNTs by as much as an order of magnitude [Jiang 2004, Li 2005], therefore the rapid thermal expansion of the polymer likely drives the film away from the glass substrate. For lower fluences, as in Fig. 7.3.2, the film expands away from the substrate and contact angles decrease as the film strains and CNTs slide past each other. When the film thermally quenches, van der Waals bonds form between the parallel CNTs, and thicker bundles of CNTs are created. Evidence of this process was experimentally observed in Fig. 7.3.2 and Fig. 7.3.3 and is illustrated in Fig. 7.3.6(b). The CNTs are in green, the glass substrate is gray, and the direction of strain is indicated by the arrows. If the fluence is increased higher, further straining causes necking, and van der Waals bonds between CNTs break within the necking region, Fig. 7.3.6(c). The film is then released from the substrate before bonds can form again. For the 10 bi-layer film, the lower density of bundles present after irradiation may indicate that lower amounts of polymer in the system lead to lower strain rates of the expanding film after irradiation. The lower strain rates mean that fewer CNTs will be pulled into bundled alignment.

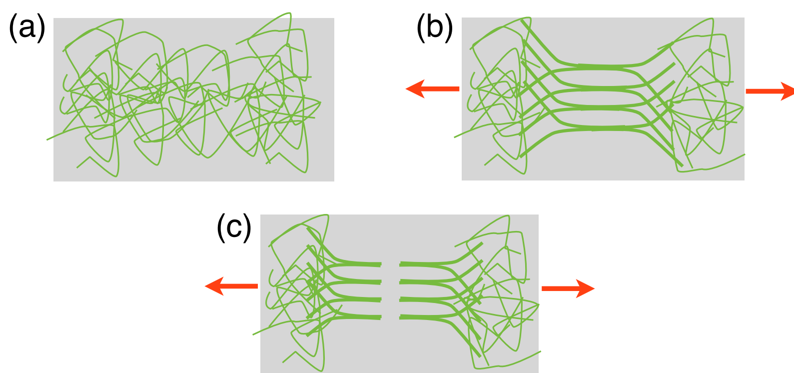

FIG 7.3.6. (a) A CNT network organized within the 2-D XY plane is shown, with CNTs in green resting on the gray substrate. (b) Straining of the network in the direction of the red arrows causes contact angles between the CNTs to decrease and the network begins to neck. Due to thermal expansion of the polymer, CNTs are aligned in both the XY- and Z-direction. (c) At higher fluences, further straining of the network within the necking region causes the film to fracture.

As was mentioned above, the resistance decreases of the film in the low fluence regime may be attributed to the formation of thicker bundles of CNTs; larger CNT-CNT contact areas are formed providing more pathways for electron flow. If the fluence is increased to 0.20 J/cm^2, CNTs are removed from the substrate at the center of the irradiated region and there are fewer pathways available. Therefore, the resistance begins to increase.

The increases in optical transmittance of the film after irradiation with low laser fluences in Fig. 7.3.4 may be due to several different factors. Removal of the polymer film from the substrate may contribute to transmittance increases, but it was found that the polymer film alone did not have an appreciable effect on transmittance. Therefore transmittance increases associated with the amount of polymer present in the film are expected to be minimal. Changes in the CNT film are expected to play the largest role in transmittance, due to the nature of light absorption by CNTs. UV-Vis spectroscopy employs light preferentially polarized in the XY plane and the absorption of light by CNTs is a polarization dependent process [Murakami 2005]. Alignment of CNTs in the Z-direction after laser irradiation reduces the amount of CNTs lying in the XY plane, which reduces light absorption in this plane and allows for the passage of more light through the film. At low laser fluence, ~ 50% of the CNTs over a 5 x 5 mm area were patterned using laser pulses and pulled out of the XY plane, resulting in an average 18% transmittance increase. At high laser fluence, ~ 37% of the CNTs were pulled out

of the XY plane and ~ 22% of the CNTs were completely removed from the substrate; both effects lead to an increase in transmittance. The transmittance increases due to pulling CNTs out of the plane are on the same orders as those seen by other groups [Murakami 2005], and these results show by controlling the percentage of CNTs pulled out of the plane (by changing the laser fluence) the film transmittance may be tuned.

In summary, it was shown in this chapter that the intense electric fields of ultrafast laser pulses may change the surface morphology of polymers and CNT-polymer composites without detrimentally changing their properties. Thermal expansion of polymers in CNT-polymer composites was shown to pull CNTs out of the XY plane on a glass substrate. The CNTs roots were still connected to CNTs lying in the XY plane demonstrating alignment of CNTS both within the XY plane and Z direction. SEM images show bundled structures after irradiation and high resolution TEM analysis shows these structures are composed of bundles of SWNTs, indicating that the laser had little effect on CNT structure. Bundles within the damage region are crossing each other at low contact angle, indicating the CNTs have experienced strain due to laser heating and rapid expansion. It is shown after patterning a large area of the composite film, transmittance of light increases and the conductivity of the network slightly increased.

References

H. Ago, K. Petritsch, M. S. P. Shaffer, A. H. Windle, and R. H. Friend, *Composites of carbon nanotubes and conjugated polymers for photovoltaic devices*, Advanced Materials **11**, 1281 (1999).

B. Bae, D. Kim, H. J. Kim, T. H. Lim, I. H. Oh, and H. Y. Ha, *Surface characterization of argon-plasma-modified perfluorosulfonic acid membranes*, Journal of Physical Chemistry **110**, 4240 (2006).

Y. Bai, S. Ho, and N. A. Kotov, *Direct-write maskless lithography of LBL nanocomposite films and its prospects for MEMS technologies*, Nanoscale **4**, 4393 (2012).

T. M. Barnes, J. D. Bergeson, R. C. Tenent, B. A. Larsen, G. Teeter, K. M. Jones, J. L. Blackburn, and J. Lagemaat, *Carbon nanotube network electrodes enabling efficient organic solar cells without a hole transport layer*, Applied Physics Letters **96**, 243309 (2010).

M. Bedewy, E. R. Meshot, H. Guo, E. A. Verploegen, W. Lu, and A. J. Hart, *Collective Mechanism for the Evolution and Self-Termination of Vertically Aligned Carbon Nanotube Growth*, Journal of Physical Chemistry C **113**, 20576 (2009).

S. A. Cho, E. A. Cho, I. H. Oh, H. J. Kim, H. Y. Ha, S. A. Hong, and J. B. Ju, *Surface modified Nafion® membrane by ion beam bombardment for fuel cell applications*, Journal of Power Sources **155**, 286 (2006).

T. Dumitrica, M.E. Garcia, H. O. Jeschke, and B. I. Yakobson, *Breathing coherent phonons and caps fragmentation in carbon nanotubes following ultrafast laser pulses,* Physical Review B **74**, 193406 (2006).

M. K. Gheith, V. A. Sinani, J. P. Wicksted, R. L. Matts, and N. A. Kotov, *Single-Walled Carbon nanotube polyelectrolyte multilayers and freestanding films as a biocompatible platform for neuroprosthetic implants*, Advanced Materials **17**, 2663 (2005).

S. X. Guo and A. Ben-Yakar, *Femtosecond laser nanoablation of glass in the near-field of single wall carbon nanotube bundles*, Journal of Physics D: Applied Physics **41**, 185306 (2008).

E. Jan, F. N. Pereira, D. L. Turner, and N. A. Kotov, *In situ gene transfection and neuronal programming on electroconductive nanocomposite to reduce inflammatory response*, Journal of Materials Chemistry **21**, 1109 (2011).

H. Jiang, B. Liu, Y. Huang, and K. C. Hwang, *Thermal expansion of single wall carbon nanotubes*, Journal of Engineering Materials and Technology **126**, 265 (2004).

M. Kandyla, T. Shih, and E. Mazur, *Femtosecond dynamics of the laser-induced solid-to-liquid phase transition in aluminum*, Physical Review B **75**, 214107 (2007).

C. Kocabas, M. A. Meitl, A. Gaur, M. Shim, and J.A. Rogers, *Aligned arrays of single-walled carbon nanotubes generated from random networks by orientationally selective laser ablation*, Nano Letters **4**, 2421 (2004).

N. A. Kotov, J. O. Winter, I. P. Clements, E. Jan, B. P. Timko, S. Campidelli, S. Pathak, A. Mazzatenta, C. M. Lieber, M. Prato, R. V. Bellamkonda, G. A. Silva, N. W. S. Kam, F. Patolsky, and L. Ballerini, *Nanomaterials for neural interfaces*, Advanced Materials **21**, 3970 (2009).

C. Kramberger, A. Waske, K. Biedermann, T. Pichler, T. Gemming, B. Büchner, and H. Kataura, *Tailoring carbon nanostructures via temperature and laser irradiation*, Chemical Physics Letters **407**, 254 (2005).

A. Lehmani, S. Durand-Vidal, and P. Turq, *Surface morphology of Nafion 117 membrane by tapping mode atomic force microscope*, Journal of Applied Polymer Science **68**, 503 (1998).

E. Leveugle, D. S. Ivanov, and L. V. Zhigilei, *Photomechanical spallation of molecular and metal targets: molecular dynamics study*, Applied Physics A. **79**, 1643 (2004).

C. Li and T. Chou, *Axial and radial thermal expansions of single-walled carbon nanotubes*, Physical Review B **71**, 235414 (2005).

M. Mahjouri-Samani, Y. S. Zhou, W. Xiong, Y. Gao, M. Mitchell, and Y. F. Lu, *Laser induced selective removal of metallic carbon nanotubes*, Nanotechnology **20**, 495202 (2009).

A. A. Mamedov, N. A. Kotov, M. Prato, D.M. Guldi, J. P. Wicksted, and A. Hirsch, *Molecular design of strong single-wall carbon nanotube/polyelectrolyte multilayer composites*, Nature Materials **1**, 190 (2002).

J. P. McDonald, V. R. Mistry, K. E. Ray, S. M. Yalisove, J. A. Nees, and N. R. Moody, *Femtosecond-laser-induced delamination and blister formation in thermal oxide films on silicon (100),* Applied Physics Letters **88**, 153121 (2006).

Y. Murakami, E. Einarsson, T. Edamura, and S. Maruyama, *Polarization dependent optical absorption properties of single-walled carbon nanotubes and methodology for the evaluation of their morphology*, Carbon **43**, 2664 (2005).

C. Orofeo, H. Ago, N. Yoshihara, and M. Tsuji, *Top-down approach to align single-walled carbon nanotubes on silicon substrate*, Applied Physics Letters **94**, 053113 (2009).

D. A. Reis, K. J. Gaffney, G. H. Gilmer, and B. Torralva, *Ultrafast dynamics of laser-excited solids*, MRS Bulletin **31**, 601 (2006).

A. H. Romero, M. E. Garcia, F. Valencia, H. Terrones, M. Terrones, and H. O. Jeschke, *Femtosecond laser nanosurgery of defects in carbon nanotubes*, Nano Letters **5**, 1361 (2005).

M. W. Rowell, M. A. Topinka, M. D. McGehee, H. Prall, G. Dennler, N. S. Sariciftci, L. Hu, and G. Gruner, *Organic solar cells with carbon nanotube network electrodes*, Applied Physics Letters **88**, 233506 (2006).

B. S. Shim and N. A. Kotov, *Single-walled carbon nanotube combing during layer-by-layer assembly: from random adsorption to aligned composites*, Langmuir **21**, 9381 (2005).

B. S. Shim, Z. Tang, M. P. Morabito, A. Agarwal, H. Hong, and N. A. Kotov, *Integration of conductivity, transparency, and mechanical strength into highly homogeneous layer-by-layer composites of single-walled carbon nanotubes for ptoelectronics*, Chemistry of Materials **19**, 5467 (2007).

S. B. Sinnott and R. Andrews, *Carbon nanotubes: synthesis, properties, and applications*, Critical Reviews in Solid State and Materials Science **26**, 145 (2001).

K. Sokolowski-Tinten, J. Bialkowski, A. Cavalleri, D. von der Linde, A. Oparin, J. Meyer-ter-Vehn, and S. I. Anisimov, *Transient states of matter during short pulse laser ablation*, Physical Review Letters **81**, 224 (1998).

J. F. Whitacre, R. D. Murphy, A. Marrie, and S. M. Yalisove, *Enhanced catalyst utilization in PEM fuel cells via ultrafast laser modification of the polymer exchange membrane surface*, Electrochemistry Communications **11**, 655 (2009).

Y. Zhang, A. Chang, J. Cao, Q. Wang, W. Kim, Y. Li, N. Morris, E. Yenilmez, J. Kong, and H. Dai, *Electric-field-directed growth of aligned single-walled carbon nanotubes*, Applied Physics Letters **79**, 3155 (2001).

Chapter 8
Conclusions and Future Work

This dissertation explores the interaction of ultrafast laser pulses with interfaces by determining damage thresholds and studying the formation of micro- and nanoscale surface features on various material surfaces. The response of thin metallic films, SiO_2 films, and CNT composite films to ultrafast irradiation was explored. Two mechanisms were found to play roles in LIPS formation after irradiation of Au features and pump-probe microscopy revealed the time scale of LIPS formation for the first time. Physical mechanisms were proposed for each observed phenomena, which reveal new insights into the interaction of fs laser pulses with materials.

The laser-solid interaction and material removal mechanisms outlined in Chapter 2 were applied to material systems involving interfaces. It was shown that both the presence of interfaces and the shape of the laser light at the material surface were important for *each* system studied in this thesis.

For bulk substrates and thin films, the temperature distribution established by the Gaussian pulse shape of the incident laser pulse is responsible for the formation of an elevated rim of material along the crater edge after material removal. Heat transfer through thin films induced material removal from the substrate if the melt front reached the interface, which also depends on the temperature distribution established by the Gaussian pulse shape. Material removal from bulk substrates near the removal threshold results from homogeneous void nucleation within the melt, and it was shown that a similar mechanism can be applied to material removal from thin films, heterogeneous void nucleation at the interface. Heterogeneous void nucleation at interfaces results in rougher surfaces after irradiation when compared to homogeneous nucleation within the film, since there are more regions where Ni isn't removed from the interface. Material removal at the interface after fs irradiation was shown to form

nanoparticles. NP formation after ns laser irradiation is only possible after irradiation of bulk substrates or after material removal from *within* films, due to the absence of the heterogeneous void nucleation mechanism at the interface. The control of material removal from interfaces after fs irradiation of thin films may lead to control over NP size in future studies. Void nucleation, thermal expansion, and the interaction of laser light with interfaces were also used to control the morphology of polymers and CNTs after fs irradiation.

Heat transfer is shown to be important for buckling of SiO_2 films on Si substrates (blister formation). Blister formation after irradiation with fs laser pulses was previously thought to be independent of heat transfer to the SiO_2 film, since the laser pulse exists for a much shorter time compared to ns laser pulses. However, two cases for blister formation at a SiO_2 thin film and a Ni thin film interface showed that heat transfer is important during blister formation at SiO_2-thin film interfaces and even at SiO_2-bulk substrate interfaces. Interface separation of 70 nm thick Ni films and heat transfer from the molten Ni elevated the SiO_2 above its glass transition temperature and induced collapse of the overlying SiO_2 film after blister formation. For much thinner Ni films, little heat transfer occurs to the SiO_2 film, and by connecting individual blisters it was found that flexible microtubes could be formed. The microtube flexibility is attributed to the lack of plastic deformation of the SiO_2, due to the low heat capacity of very thin Ni films and the lower laser fluence required to form blisters at these interfaces. Plastic deformation at blister edges (root formation) occurs after blister formation at SiO_2 film-bulk substrate interfaces and explains the rigidity of microtubes at these interfaces. The blister edge stays in contact with molten Si after blister formation, forming a root. Analysis of the blister dimensions predicts the blisters are under larger stresses than those present in the film. However, root formation at the blister edge leads to permanent delamination of the SiO_2 film and the formation of blisters with radii smaller than those expected when the magnitude of the compressive stress of the film before irradiation is accounted for. After multiple laser shots, the radius of the molten pool of Si increases, forming wider and taller blisters and allowing for blister and microtube formation at fluences which are lower than single shot blister and microtube thresholds.

The shape of laser light at the air-solid interface was shown to be responsible for LIPS formation in Chapter 6. Previous studies have suggested that randomly rough surfaces are required for LIPS formation, but it is shown in this thesis that single surface defects alone are sufficient to alter the shape of the incident laser light and form LIPS on material surfaces after single shot irradiation of polished surfaces. In the literature, LIPS are typically observed perpendicular to the laser polarization direction. SPP excitation by laser light which is TM polarized w.r.t. random surface features is generally accepted as being responsible for LIPS formation. But several examples in this thesis are presented which show that the shape of features initially present on the surface affect the LIPS morphology and LIPS aren't always perpendicular to the laser polarization. Irradiation of Au mesa microstructures with single laser shots forms LIPS in the near vicinity of mesas for all angles of laser polarization w.r.t. mesa edges, showing that Huygens-Fresnel diffraction from surface features is responsible for LIPS formation at any angle. SPP excitation enhances light absorption at the surface and shifts the periods of the LIPS for certain polarization angles w.r.t. to mesa edges. This demonstrates that factors which are important for irradiation of bulk materials with ultrafast laser pulses, such as changes in carrier densities and the dielectric function with fluence, are also important for LIPS formation. These properties and near-field diffraction are dependent on the material type, surface features and interface. Therefore, the nature of the laser-solid interaction will change after each laser shot. Finally, after absorption of the laser light, pump-probe microscopy has shown that material removal mechanisms discussed for irradiation of bulk substrates can be applied to LIPS formation.

These studies have important implications for irradiation of material surfaces with multiple laser shots. Diffraction of laser light from surface features such as crater edges, thin films, and isolated defects forms LIPS at many angles w.r.t. the laser polarization, which explains why some studies observe LIPS at different angles depending on the number of laser shots irradiating the material surface.

The landscape of a surface changes after irradiation with just a single laser pulse above the damage threshold; therefore, both the shape of the incident laser light and the material response change after each subsequent laser shot. Future studies and

processes will depend on the ability to control the laser-solid interaction after irradiation with both single and multiple laser shots. Control thus far has led to interesting changes in surface morphology (especially LIPS formation), but further control such as pulse shaping may lead to the ability to irradiate any surface with multiple laser pulses and not form any surface features at all. This control can only be gained by being able to predict how laser pulses interact with surfaces and how the surface changes and responds to the laser light.

The following sections provide a summary of the results, conclusions, and future work for each of the goals presented in Chapter 1.

Section 8.1 Single Interfaces

For Ni films on glass substrates in Chapter 4, a material removal threshold dependence on film thickness was found by varying the Ni film thickness. Thresholds generally decreased with decreasing film thickness, which was partially due to an increase and peak of film absorptance for thin films. For film thicknesses ≤ 20 nm, a transition from material removal within the film to removal at the interface occurred. Material removal within the film produced smoother surfaces than removal at the interface, indicating a transition from homogeneous void nucleation within the film to heterogeneous void nucleation at the interface. When the Ni film thickness was < 20 nm, the calculated film absorptance rapidly decreased with film thickness, but the threshold only slightly increased. This behavior was attributed to the lower energy requirements for heterogeneous void nucleation at interfaces.

For Ni film thicknesses ≥ 20 nm, material removal always occurred within the film at the damage threshold. If the fluence was increased, heat transfer propagated through the Ni film to the interface and thermal expansion of the molten film nucleated voids at the interface, allowing for separation of material from the interface. Comparisons of the laser fluences required for the melt front to reach the interface for varying Ni film thicknesses should be made to modeling results to determine the validity of this physical model. Pump-probe microscopy could also be employed to observe

material removal from both within the film and at the interface to gain an understanding of the dynamics of material removal from within films and at the interface.

NP formation was observed after the irradiation of Ni films with fs laser pulses but the dependence of NP size on Ni film thickness was not explored. The horizontal printing geometry discussed in Chapter 4 did not allow for efficient NP collection for films < 20 nm thick. A top-down printing geometry could allow for more efficient NP collection and the study of the NP size dependence on Ni film thickness. Future studies will also focus on further control of the atmosphere the NPs are created in with different background gases and pressures for control of NP size and faceting.

It was found that it is not necessary to deposit a film onto a Si substrate and heat the film to form NPs. A method of printing NPs directly onto the Si substrate was developed and CNT growth from the catalytic NPs was demonstrated.

To refine the dependence of the Ni film threshold on absorbed laser light intensity, the transmitted and reflected intensities of light during irradiation of the Ni films should be measured. It will then be possible to determine the precise dependence of the Ni film absorptance on film thickness. The surface roughness in this thesis was only compared at one fluence for intra-film separation and interface separation. Surface roughness should be compared for a range of fluences and film thicknesses to determine the dependence of surface roughness on fluence and void nucleation. Material properties such as surface hydrophobicity are highly dependent on surface roughness so these studies will likely have many applications. Modeling should also be performed to determine the exact mechanisms for how film thickness corresponds to where the material breaks within the film, the relation of material removal to the melt front and interface. The precise dependence of material removal on film thickness and film adhesion to the substrate will require further studies and computational modeling of the phenomena.

A detailed study of CNT properties after growth using printed Ni catalyst NPs such as the number of walls formed and chirality should be performed using TEM and Raman spectroscopy. CNT properties may be dependent on NP properties such as size, NP faceting, and NP composition.

Section 8.2 Multiple Interfaces

Blistering behavior at a metal-SiO_2 interface was observed for the first time in Chapter 5. For a 70 nm Ni film-SiO_2 interface, the blister dimensions linearly increased with laser fluence until a threshold fluence was reached and the blister heights began decreasing. Blister collapse occurred at the same fluences as pit formation in the 70 nm Ni film without the overlying SiO_2 film. This behavior was attributed to molten Ni striking the buckled SiO_2 film, raising the SiO_2 temperature above its glass transition temperature and causing the SiO_2 film to sag. Future studies should use a FIB cutting technique to expose the inside of the collapsed blister for SEM imaging. This will allow examination of the underside of the collapsed blister to determine the approximate amount of Ni which was deposited onto the SiO_2 film above the pits. Further analysis will involve estimating the amount of heat transferred from this Ni to the SiO_2 film and the subsequent temperature rise of the SiO_2 film.

When the Ni film thickness was decreased further, the blister formation threshold decreased with decreasing film thickness. The blister threshold follows a similar trend as the Ni damage threshold for varying film thickness, indicating that the response of thin Ni films to fs irradiation affects blistering behaviors. It was shown for very thin films that microtubes formed at these interfaces are flexible and the lack of a plastically deformed SiO_2 root was proposed to explain this behavior. The lack of a root for thinner Ni films proves that for bulk substrates, heat transfer from the substrate to the SiO_2 film during blister formation plays a role in blister formation. Material removal is playing a minimal role in SiO_2 buckling at thin film interfaces and buckling mechanisms should mostly be dependent on what is predicted by the clamped circular plate theory. However, SiO_2 buckling as a function of spot size was not explored. Larger melt regions of the film at the interface should induce buckling of the SiO_2 layer at lower laser fluences and without any mechanism which is assisted by material removal. In order to compare blister formation to the buckling theory, stress at the thin Ni film-SiO_2 interface must be determined before blister formation. Stress in the Si-SiO_2 wafers was calculated by measuring changes in wafer radius of curvature before and after SiO_2 growth with a Flexus laser interferometer at the UM LNF. Since the thin Ni film and SiO_2

were deposited onto microscope slides it was not possible to measure film curvature using the interferometer. Future studies will focus on using Multi-beam Optical Sensors (MOS) available at k-Space Associates, Inc. to obtain 2D stress profiles of the thin Ni and SiO_2 films on microscope slides. These stress profiles will then be compared to the stress predictions based on the clamped plate buckling theory.

The presence of a root for buckled SiO_2 may be further explored by performing mechanics analysis of the buckled SiO_2 using AFM techniques. It is likely that varying degrees of microtube flexibility exist which could not be studied using optical techniques or height measurements. These buckling regimes may be studied by measuring blister and microtube strain for a given force applied by an AFM tip.

Flexibility and the lack of a root for the buckled SiO_2 film for very thin Ni films was demonstrated by inducing collapse of the microtubes with water flow. Flexible microfluidic tubes have applications such as in-plane microvalves and micropumps by externally straining the buckled SiO_2 film, but this is only possible if movement of the SiO_2 film can be driven externally. Initial studies of externally driving the SiO_2 film may use piezoelectrics attached to the microfluidic tube surface. For energy applications microtube stacking will be important to obtain higher energy densities. This may be possible by forming microtubes at the Ni film-SiO_2 interface, depositing additional Ni film and SiO_2 layers onto the buckled SiO_2, and irradiating the structure to form one microtube on top of the other. In principle this process could be repeated a number of times to continue stacking microtubes, although there are likely limits due to stress building up within the film structure with repetitive stacking of thin films.

As with the results of thin Ni films on glass substrates in Chapter 4, it is important to know the exact composition of films < 10 nm thick and the nature of laser energy coupling to these thin films and interfaces. Future studies will focus on using reflectance and transmittance studies to determine the composition of Ni films and relating composition to absorbed laser fluence.

Section 8.3 Laser Induced Periodic Structures

The polarization dependence of LIPS formation was determined in a controlled manner by irradiating features on Si surfaces after a single shot in Chapter 6. Some features were created by a laser pulse which forms edges in Si or blisters at a Si-SiO_2 interface. Other Au features were deposited with lithography. Irradiating Si crater edges with a single laser shot showed that LIPS formed mostly perpendicular to the polarization vector, while LIPS formation at a Si-SiO_2 interface showed LIPS formation mostly parallel to the polarization vector. Two mechanisms are thought to be playing a role in LIPS formation and are polarization dependent. By irradiating Au mesas, a strong polarization dependence of LIPS amplitude was found and LIPS amplitudes were larger when the polarization vector was perpendicular to mesa edges, compared to irradiation with the polarization vector parallel to mesa edges. LIPS were also observed to form on multiple surfaces from different sources, showing that diffraction mechanisms in the near field are responsible for LIPS formation. SPP excitation is allowed when the polarization vector is perpendicular to mesa edges and is responsible for the larger amount of energy coupled to the material surface. For polarization vectors parallel to mesa edges, SPP excitation is forbidden and the diffracted light intensity is lower when SPPs are not excited. A diffraction mechanism without SPP excitation therefore produces LIPS with lower amplitudes when the polarization vector is parallel to mesa edges.

The formation of local, periodic amorphous Si below both the Si ablation threshold and LIPS formation threshold for a polarization direction perpendicular to a mesa edge proves that the laser intensity is periodically varied by mesa edges before LIPS formation occurs. There is a transition from periodic amorphous Si formation to LIPS formation to material removal which was not explored in this thesis. The peak laser fluence should be varied at finer steps from the Si amorphization threshold up to the LIPS formation and material removal thresholds to observe this transition. By stepping through these lower laser fluences the transition from light absorption on the Si surface, to expansion of molten material, and finally to material removal may be observed.

It is clear that mesa edges are diffracting energy into regions of the focused beam which don't cause material removal when the Si substrate is irradiated far away

from mesa edges. To experimentally test this model, the Si crater size formed at varying distances from the mesa edges should be systematically compared with crater sizes formed far away from edges. The laser polarization should also be varied for the same experiment to determine how much energy is diffracted with parallel polarization and how much energy is taken from the laser pulse to excite SPPs for perpendicular polarization. Modeling should also be performed for the same conditions and compared to experiment.

The first known determination of time scales for LIPS formation after multiple laser shots in a Si substrate was performed using pump-probe microscopy. To achieve this, a new pump-probe microscopy technique employing white light and Fresnel fringes was developed in order to image LIPS on a Si surface. The time scales for LIPS formation are on the same time scales as material removal due to expansion of molten material, suggesting that a combination of the rapid expansion of molten material and material removal is responsible for the initiation of LIPS formation. This pump-probe technique should be used to study the dynamics of LIPS formation after mesa irradiation to determine if the two different mechanisms for LIPS formation cause LIPS to form on different time scales. It may also be possible to observe near field effects using the white light setup by varying the polarization state of the pump laser light with mesa edges and measuring the reflected light intensity. This could help elucidate the two proposed LIPS formation mechanisms by measuring surface reflectivity changes due to incident light intensity, plasmon excitation, and reflected light intensity.

Varying the mesa heights will help to decouple SPP excitation and Fresnel diffraction by bringing the mesa edge out of the near field of the Si substrate. Measurements of LIPS periodicity will then be more reliable since one mechanism will be decoupled from the other. The mesa and substrate materials should also be varied to explore the dependence of SPP excitation and diffraction intensity on material type (i.e. semiconductors vs. metals) and compared to the current LIPS literature of LIPS formation on bulk substrates.

It will be important to determine the diffracted light and SPP excitation intensities at the Si-SiO_2 interface. It is expected that the SiO_2 thickness will change the diffracted light intensity at the Si interface and change the orientation of the LIPS. A combination

of both LIPS formed parallel and perpendicular to the laser polarization direction should be observed for varying the thickness of SiO_2. Systematic studies which explore the orientation dependence of LIPS on both fluence and SiO_2 thickness should be performed.

Section 8.4 Composites

It was shown in Chapter 7 that the morphology of CNT-polymer composite films may be changed using fs laser pulses without changing the nanostructure of the CNTs. A new CNT alignment mechanism was demonstrated which pulls CNTs out of the XY plane and into the Z direction. Such CNT alignment is not currently possible with any other current CNT growth technique.

Thermal expansion of polymers in CNT-polymer composites was shown to pull CNTs out of the XY plane on a glass substrate. The CNT roots were still connected to CNTs lying in the XY plane demonstrating alignment of CNTS both within the XY plane and Z direction. SEM images show bundled structures after irradiation and high resolution TEM analysis shows these structures are composed of bundles of SWNTs, indicating that the laser had little effect on CNT structure. Bundles within the damage region are crossing each other at low contact angle, indicating the CNTs have experienced strain due to laser heating and rapid expansion. It was shown after patterning a large area of the composite film, that the transmittance of light increased and the conductivity of the network also slightly increased. The transmittance increases were attributed to pulling the CNTs out of the XY plane, since the absorption of laser light by CNTs is polarization dependent and the laser polarization lies in the XY plane. Slight resistance decreases of the film after large-scale irradiation were attributed to the formation of CNT bundles which increases contact areas between CNTs and decreases the CNT contact resistance.

Future studies of CNT-polymer composite films should focus on further control of CNT alignment after irradiation. Varying the number of composite bi-layers was not studied in this thesis and will likely have a large affect on the response of the composite film to fs irradiation and bundling of the CNTs. The fs irradiation of different polymer and

composite films should also be explored since it was shown here that simple irradiation of just one kind of composite film changed the film's properties. Many composite films have issues with bonding within the polymer network and also bonding with the underlying substrate. Changing the surface roughness of the films with fs laser irradiation will change the surface area and regions of the polymer which are available for bonding. This could lead to improvements in the mechanical properties of polymers and composite films and also improvements in conductive properties.

Section 8.5 Improving Uniformity

Finally, the interpretation of all the results presented in this thesis would be greatly simplified if the experiments were performed with a flat-top beam. The Gaussian shape of the pulse used in this thesis means that the material response to ultrafast irradiation is the result of irradiation with a wide range of fluences, complicating the experimental results, especially those of blister and LIPS formation. Irradiation with a flat-top beam would mean that each experiment could be performed where a single laser fluence is dominating, and it would be easier to elucidate the precise mechanisms responsible for the resulting morphology after ultrafast laser irradiation.

Appendices

Appendix 1

To control the 3-axis translation stage, graphical user interfaces (GUI) were written in LabVIEW. The code and GUI for basic controls of stage movement such as changing the stage velocity, moving relative distances, and moving to specific locations, are shown in Figures A1.1. - A1.3.

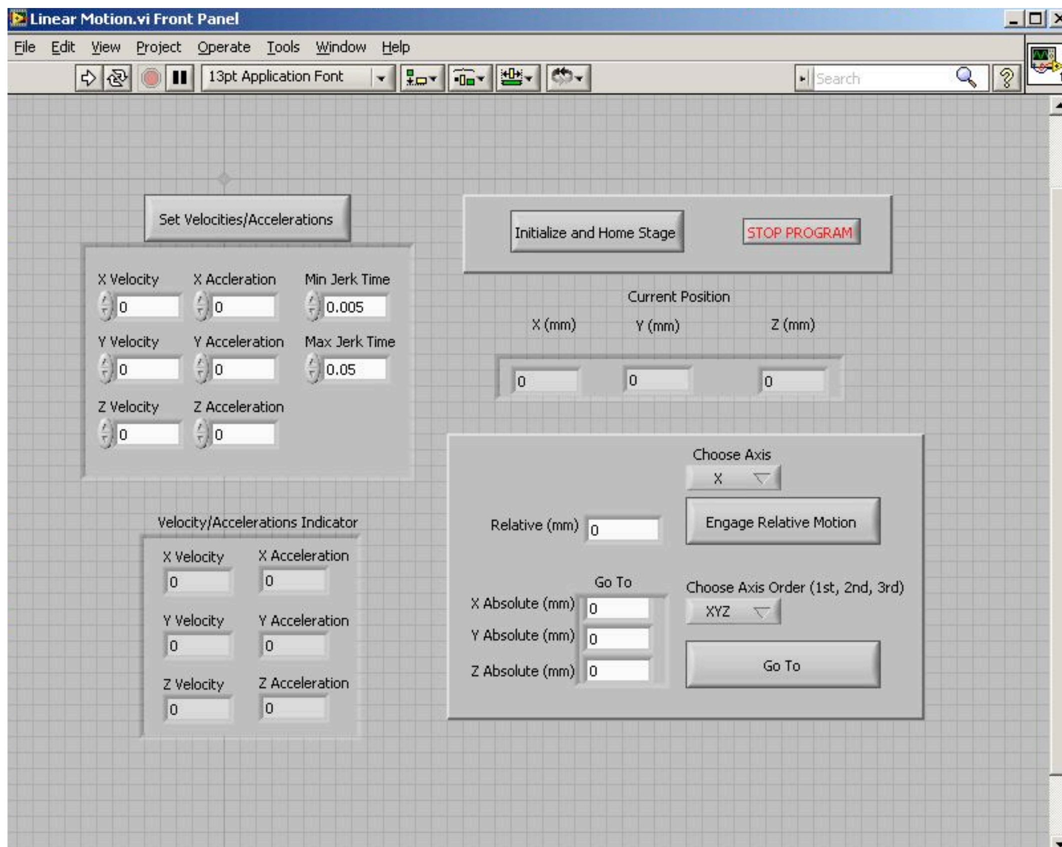

FIG. A1.1. LabVIEW GUI for basic 3-axis stage movement.

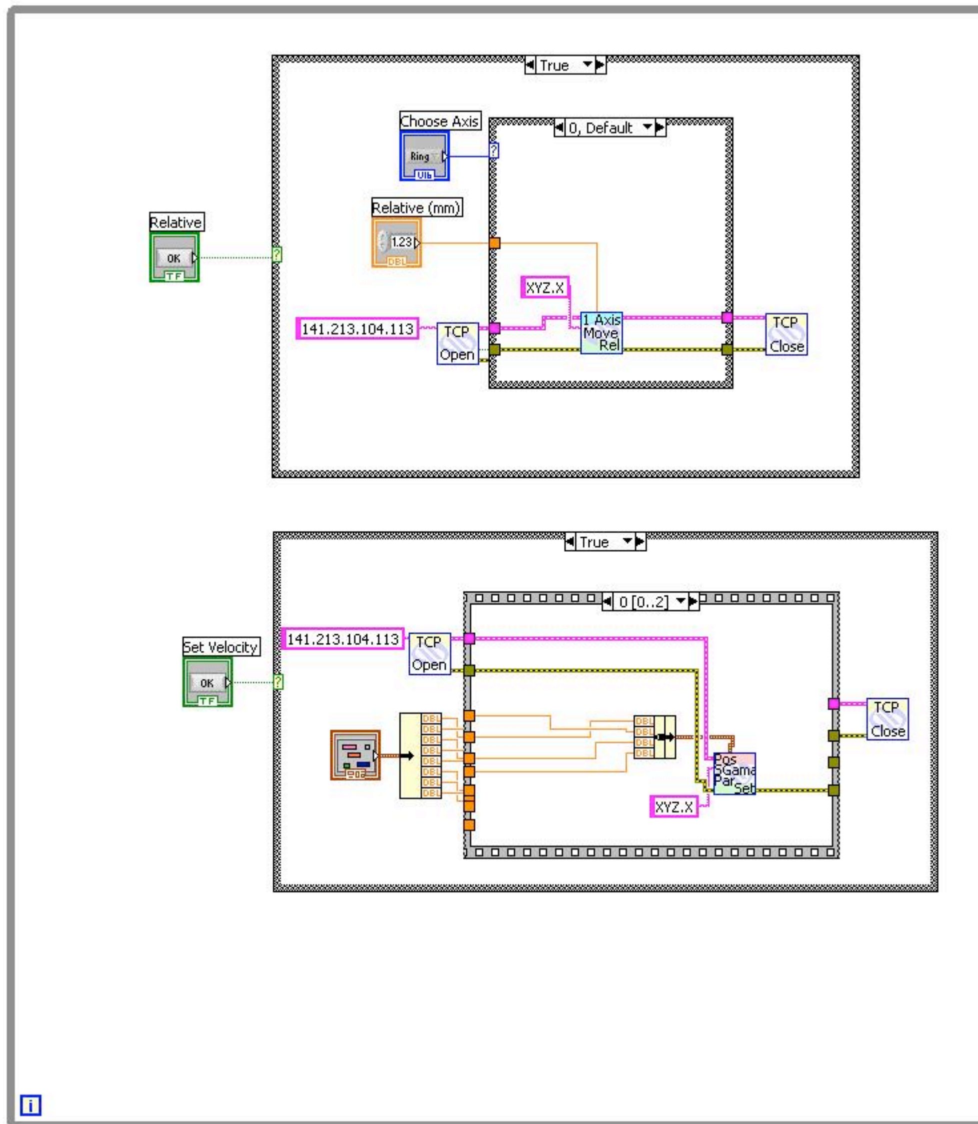

FIG. A1.2. Partial LabVIEW code for basic 3-axis stage movement. Continued in Fig. A1.3.

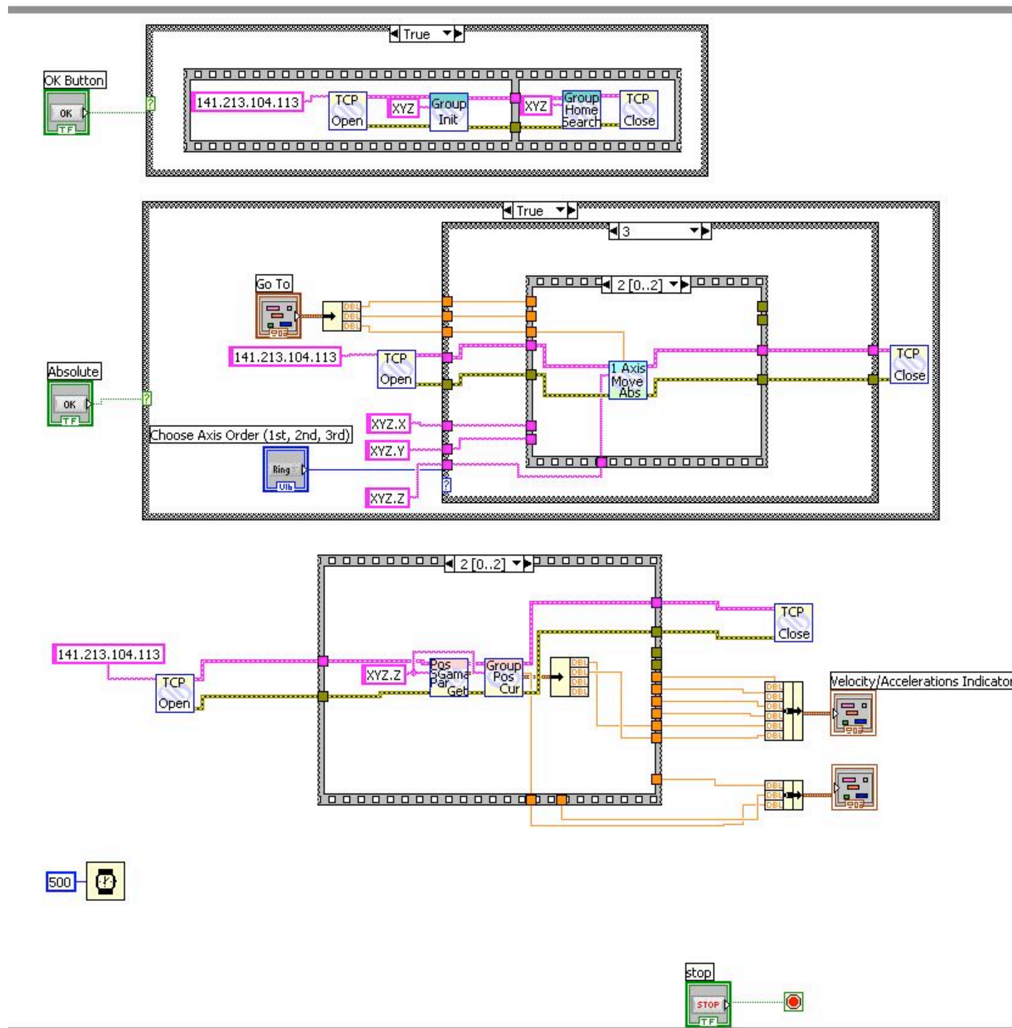

FIG. A1.3. Partial LabVIEW code for basic 3-axis stage movement. Continued from Fig. A1.2.

LabVIEW code used to repeat stage movements with the option for pauses between each step is shown in Figures A1.4 and A1.6. This code was used for large-scale patterning of samples or for finding the damage thresholds of samples. Pauses could be added to allow for changing the incident laser power or exchanging samples.

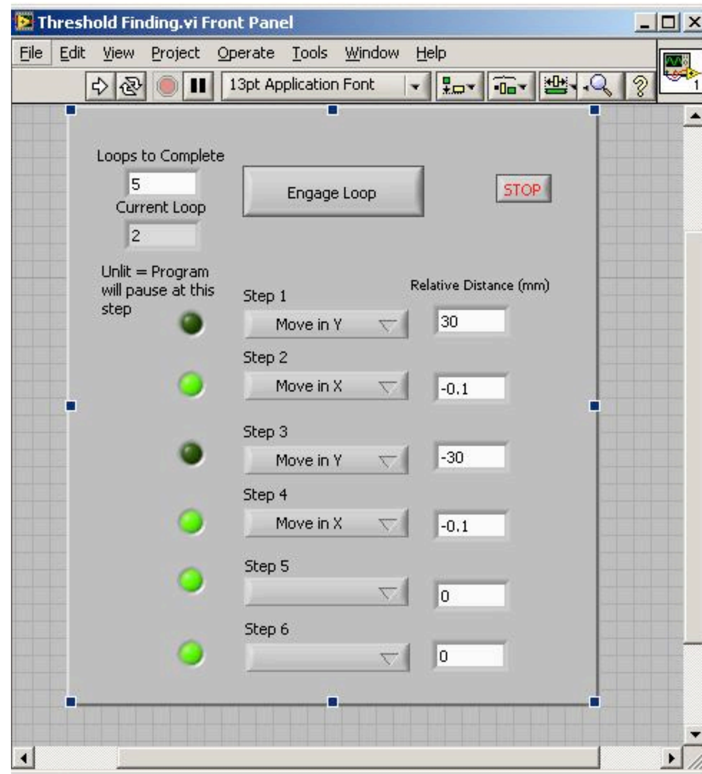

FIG. A1.4. LabVIEW GUI for repetitive control of the 3-axis stage.

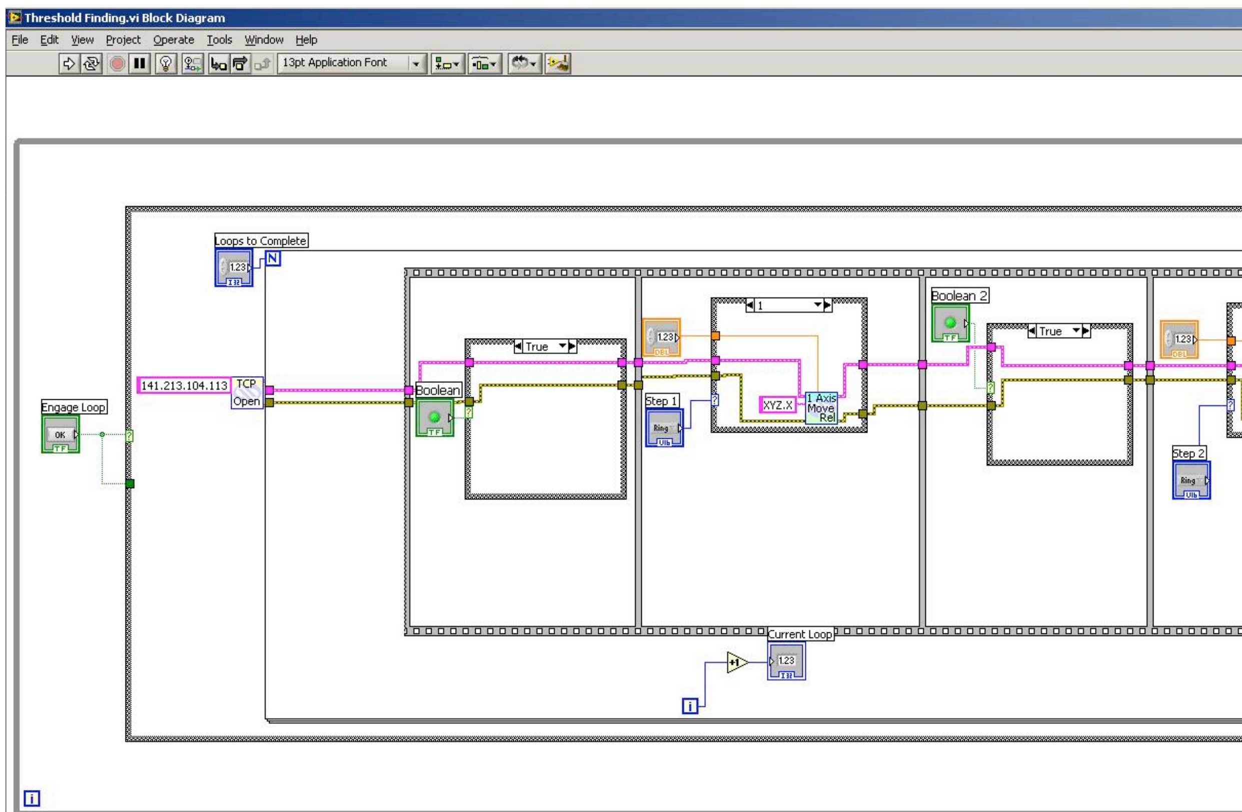

FIG. A1.5. Partial LabVIEW code showing the first few steps in the for loop for repetitive control of the 3-axis stage.

Appendix 2

Below is a proof that when the $\frac{1}{e^2}$ major and minor radii *a* and *b* of the focused elliptical Gaussian beam are used, then the formula $F = \frac{2E_{Total}}{\pi ab}$ will give the peak fluence of the Gaussian beam.

The intensity of an elliptical Gaussian beam when *a* and *b* are the $\frac{1}{e^2}$ radii of the beam is given by:

$$I(x,y) = I_0 e^{-2\left(\frac{x^2}{a^2}+\frac{y^2}{b^2}\right)}$$

If *F* is the peak fluence, then the local fluence at any point in the projection of the Gaussian is:

$$F(x,y) = Fe^{\frac{-2x^2}{a^2}} e^{\frac{-2y^2}{b^2}}$$

E_{Inside} is the energy under the Gaussian after integrating over an area of an ellipse is:

$$E_{Inside} = F\int e^{\frac{-2x^2}{a^2}}\,dx\int e^{\frac{-2y^2}{b^2}}\,dy$$

If we assume that $F = \frac{2E_{Total}}{\pi ab}$, then the total energy under the Gaussian is calculated by integrating over all space:

$$E_{Inside} = \frac{2E_{Total}}{\pi ab}\int_{-\infty}^{\infty} e^{\frac{-2x^2}{a^2}}\,dx\int_{-\infty}^{\infty} e^{\frac{-2y^2}{b^2}}\,dy$$

$$E_{Inside} = \frac{2E_{Total}}{\pi ab}\left[\frac{a\sqrt{\pi}}{\sqrt{2}}\right]\left[\frac{b\sqrt{\pi}}{\sqrt{2}}\right]$$

$$E_{Inside} = E_{Total}$$

Appendix 3

To perform experiments in a low vacuum of ~ 40 mTorr, a vacuum chamber was built to hold samples in vacuum and allow laser light to pass through a window on the chamber.

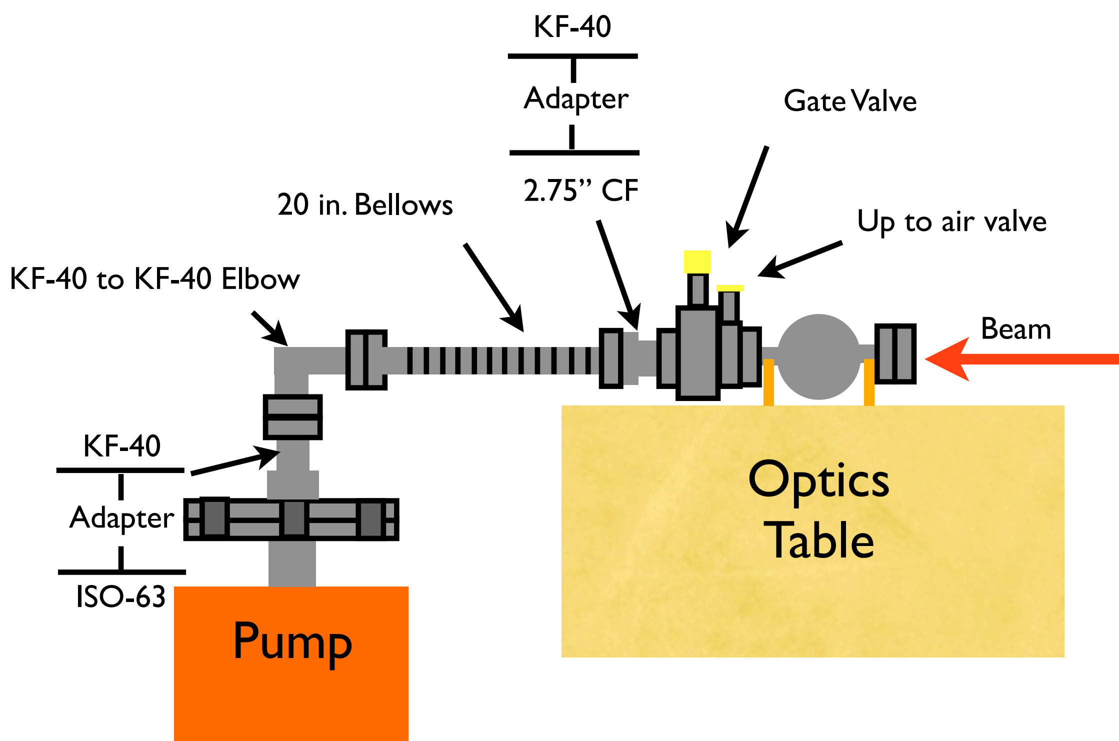

FIG. A3.1. Design of the vacuum chamber used for NP printing in vacuum.

The steps for pumping down and venting the vacuum chamber are outlined below.

1) Insert sample by disconnecting Kwik flange from the gate valve and sliding sample into the cross.

2) Reconnect Kwik flange and open gate valve.

3) Make sure the Up To Air valve is closed.

4) Start pump. Wait until operating pressure is reached.

5) Stop pump.

6) Close gate valve. Ensure operating pressure is maintained.

7) Perform experiment.

8) Turn the pump off and wait for it to spin down.

9) Open the gate valve.

10) Open the Up To Air valve.

11) Disconnect Kwik flange for sample exchange.

Appendix 4

In order to view the evolution of the same ablation event after a single pulse irradiates the sample, a possible design for a 2-D optical streak camera is outlined below. White probe light is produced from non-linear interactions with water and filtered, perhaps with notch filters, and each color is delayed at a different time delay, perhaps with a second prism. Each probe color irradiates the sample backwards through the objective and then travels back through the objective. The colors are spread across the CCD camera with a prism so that multiple colors and time delays from the same ablation event may be captured in the same image.

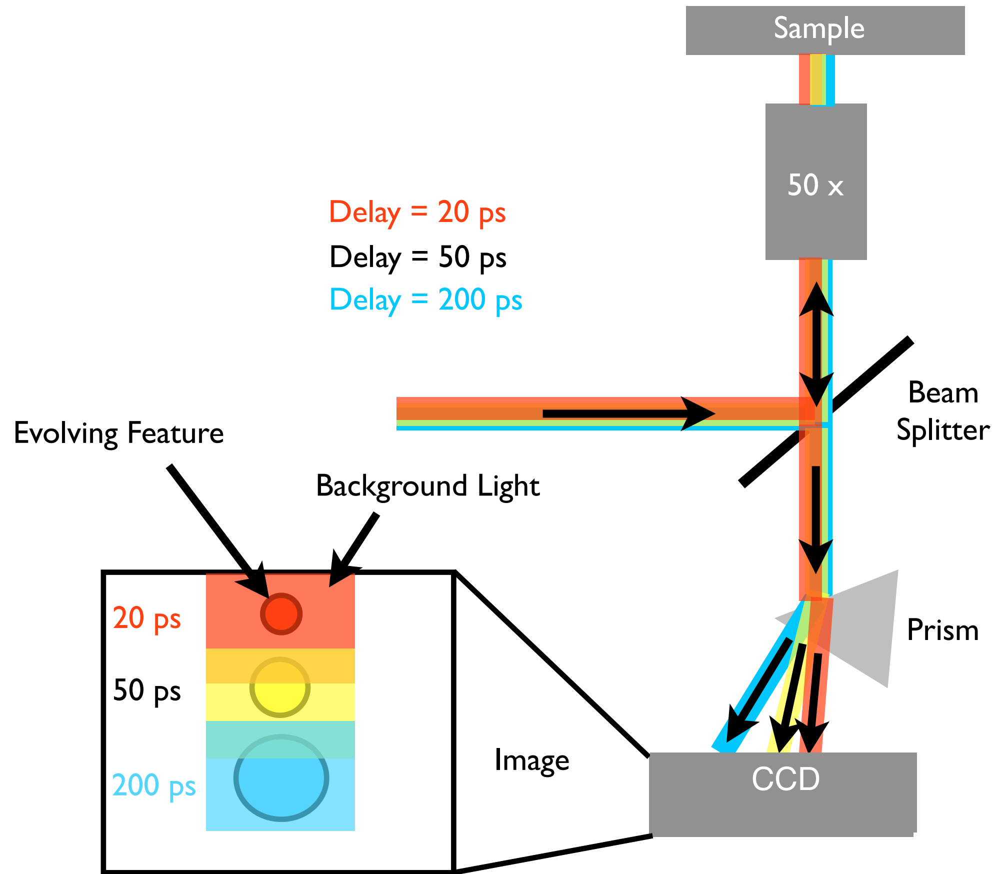

FIG. A4.1. Possible design of a 2-D optical streak camera for imaging the same ablation event at different time steps.

Appendix 5

The mesa deposition process performed at Sandia National Laboratories is outlined below.

The patterning process starts with dehydration and surface treatment of a substrate to be patterned. These surfaces can have excess moisture adsorbed on the surface that can affect the adhesion of photoresist. These wafers are processed through a vapor prime oven where they are dehydration baked, and if the surface is oxidized, are exposed to an adhesion promoter hexamethyldisilazane (HMDS). Adhesion promoters are used to enhance the bonding of photoresist to silicon nitride or silicon dioxide surfaces. This process is run under reduced pressure at a temperature of 150 ºC. The wafer is baked out for a period of time to remove excess moisture from the surface. After this dehydration bake the process chamber is exposed to the HMDS vapor, which coats the surface of the wafer. Shortly after the completion of the HMDS process, the wafer is coated with photoresist.

The photoresist is spun onto the surface of wafers using a spin coater. The first part or the spin program ramps up the speed slowly to spread the resist uniformly over the surface of the wafer. In the next step the spinner quickly accelerates to the final speed to remove the excess material. The increased speed and acceleration of this step improves the final thickness uniformity of the photoresist across the surface of the wafer.

After the spin coat process is complete, the photoresist coated wafer is immediately moved to a hot plate to bake out the solvent and solidify the layer. The baking parameters for photoresist vary depending on the product type and thickness. For 5214 resist used in this experiment, we bake to ~ 90 °C. The thickness of the photoresist can be tailored to the desired thickness of the patterned thin film. In general,

thinner layers of photoresist are used to pattern thinner metal layers. If a thick layer of photoresist is desired, then multiple coats can be applied and baked in a similar fashion.

There are two types of photoresist: positive and negative. UV light and baking alters the chemical structure of the photoresist and affects its solubility in the developer solution. When positive resist is exposed to UV light it becomes more soluble in developer. Negative resist becomes insoluble after exposure to UV light, and remains wherever it was exposed. An additional bake step after UV exposure is typical to complete the chemical altering of the negative photoresist.

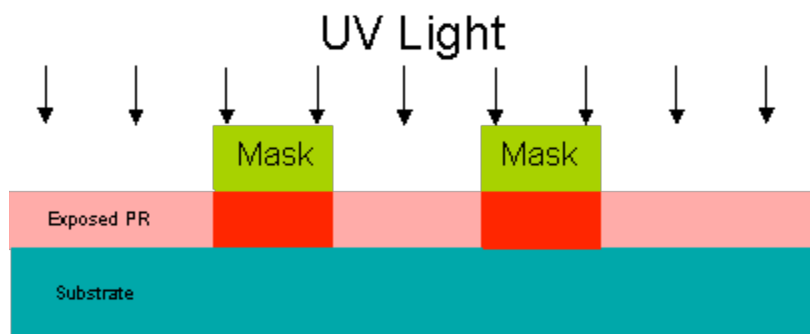

FIG. A5.1. Depiction of UV light exposure of photoresist using a mask.

The final process for patterning photoresist is development. Development of the photoresist is done using a solution of tetramethylammonium hydroxide. The liquid solution is poured into a container, and the wafer is immersed in the solution. The process time to complete the development is dependent on the thickness of the photoresist. At the end of the development process, the wafer is moved to a bath of deionized water to completely rinse the surface of residual chemical. The final step is to dry the wafer using dry nitrogen.

FIG. A5.2. Depiction of remaining photoresist pattern after exposure and development (and rinse).

The overhang or reentrant profile of the pattern is the key feature that enables the lift-off process to pattern thin films. This profile is created when the sample is placed in the basic developer solution. The lower region of the profile is etched away more than the upper region as a result of under exposure of the lower portion of resist at the edge of the pattern. In general, the thickness of the photoresist should be greater than the film thickness by a factor of 3 or more. However, this is limited by the width of the smallest patterned features.

After the photoresist is developed, the wafer is prepared for the thin film deposition process (for this experiment we use magnetron sputtering). Prior to loading the wafer into a deposition system, it is cleaned using a plasma. This process cleans the patterned areas on the wafer that are open to the surface of the substrate, and etches away any remaining photoresist residue. The plasma process is run at reduced pressure in a pure oxygen atmosphere.

The thin film layer is blanket sputter deposited, and coats the photoresist and the areas that are open to the substrate. The deposited layer not only coats the horizontal surfaces, but also a portion of the vertical surfaces. For these experiments, magnetron DC sputter deposition coated the entire wafer with Ti/Au to a thickness of 1100 Å (i.e., 100 Å Ti and a 1000 Å Au cap).

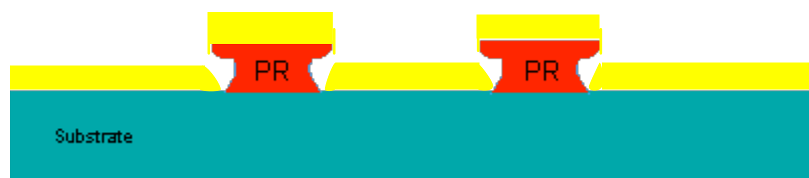

FIG. A5.3. Depiction of photoresist and substrate covered with Ti/Au.

The lift-off of the thin film-coated wafer is processed in a container of acetone. The acetone slowly penetrates the edges of the patterned features and dissolves the photoresist. Eventually, the entire layer of thin film that was deposited on the photoresist floats off. This process is slow and can take 3 hours or more to complete. The figure

below shows the resulting pattern of Ti/Au on the substrate at the end of the lift-off process.

FIG. A5.4. Depiction of Ti/Au after liftoff of PR.

Appendix 6

A MATLAB code was written to calculate Fourier transforms (FT) of LIPS using csv height data collected by performing AFM on the LIPS. The following code plots the height data, prompts the user to select a portion of the plot, and takes a FT of the plot only in the selected area.

```
function ryanfft = FTPlotSelection(data)
window = figure;
figure(window);
clf;
subplot(2,1,1);
plot(data(:,1),data(:,2));
axis([min(data(:,1)) max(data(:,1)) min(data(:,2)) max(data(:,2))]);
subplot(2,1,2);
plot(data(:,2));
%axis([min(data(:,1)) max(data(:,1)) min(data(:,2)) max(data(:,2))]);
axis([0 length(data(:,1)) min(data(:,2)) max(data(:,2))]);
myrect = getrect(window);
xmin = round(myrect(1));
xmax = xmin+round(myrect(3));
myfft = data(xmin:xmax,:);
myx = myfft(:,1);
myamp = myfft(:,2);
deltax = myx(2)-myx(1);
```

```
N=size(myfft(:,2),1)*100;
ryanfft(:,2) = abs(fftshift(fft(myamp,N)));
freq = (1/deltax)*[-N/2:N/2-1]/N;
ryanfft(:,1) = freq;
plot(freq, ryanfft)
```